UNIVERSITY OF SOUTHAMPTON

FACULTY OF ENGINEERING, SCIENCE AND MATHEMATICS

School of Chemistry

Fabrication, Characterisation, and Optical Applications of Electrochemically Deposited Nanostructured IrOx Films

By

Jin Hu

Thesis submitted for the degree of Doctor of Philosophy

October 2008

UNIVERSITY OF SOUTHAMPTON

ABSTRACT

FACULTY OF ENGINEERING, SCIENCE AND MATHEMATICS
SCHOOL OF CHEMISTRY

Doctor of Philosophy

Fabrication, Characterisation, and Optical Applications of Electrochemically Deposited Nanostructured IrOx Films

By Jin Hu

In this work, nanostructured iridium oxide films were fabricated by electrochemical deposition within a template made with polystyrene spheres on gold substrates. SEM pictures show that the nanostructured IrOx films have a very ordered hexagonal structure. To our knowledge, this is the first report of templated deposition of nanostructured IrOx films and only the 2nd of fabrication of templated deposition of nanostructured electrochromic metal oxides.

The deposition solution was carried out under voltammetric control with a solution made from iridium tetrachloride, hydrogen peroxide, oxalic acid and potassium carbonate based on a recipe reported by Yamanaka (Anodically Electrodeposited Iridium Oxide-Films (AEIROF) from Alkaline-Solutions for Electrochromic Display Devices, *Jpn. J. Appl. Phys. Part 1 - Regul. Pap. Short Notes Rev. Pap.* **1989**, *28*, 632). Both non structured and nanostructured IrOx films were grown with the deposition solution. During the voltammetry, the growth of the film was followed by monitoring the cathodic peaks and anodic peaks which reflect redox reactions Ir(III) / Ir(IV) and Ir(IV) / Ir(V) within the IrOx oxide film. During the deposition, the peak currents increase almost linearly with the number of voltammetric cycles thus allowing a fine control of the deposition process. Several attempts were made to estimate the film thickness and establish a relationship between film thickness and deposition cycles. The thickness of the nanostructured films is particularly difficult to measure accurately. Following deposition, the electrochemistry of the nanostructured IrOx films was characterised with cyclic voltammetry in both acid and base solutions.

Optical properties of the nanostructured IrOx films were investigated. The transmittance of a nanostructured IrOx films was measured with transparent ITO substrates. The novel idea of coating a thin layer of IrOx film on a nanostructured gold surface was investigated to test whether the electrochromism of the nanostructured IrOx film could be used to alter the surface plasmons of the nanostructured substrate. The nanostructured IrOx film worked as a surface plasmon modulator when its colours shifted between dark and transparent under potential control. The reflectance of thickness-graded nanostructured IrOx films was measured over a range of incident angles for different potentials. Following very recent publications on the theoretical modelling of light interaction with nanostructured gold films, an attempt was made to analyse the results obtained with the nanostructured IrOx films in terms of the interplay between the localised and delocalised surface plasmons.

ACKNOWLEDGEMENTS

First and foremost, I would like to deeply thank my supervisor Dr. Guy Denuault for his guidance and encouragement throughout this research.

I would like to acknowledge the assistance of other people who have contributed their time and expertise. I would especially like to thank Prof. Phil Bartlett and Prof. Jeremy Baumberg. Particular thanks also go to Mr Sumeet Mahajan, who has helped and supported me during the research.

I would like to thank my adviser Dr Peter Birkin for advising my progress as a PhD student.

I would also like to thank the Denuault group and the other members of electrochemistry group that have supported me during my study.

I would like to take this opportunity to thank my family in China.

Finally, I would like to thank Fei Xu for his understanding and support.

Contents

List of Symbols and Abbreviations

BNC cable	Bayonet Neill-Concelman cable
CV	Cyclic voltammogram
IrOx	Iridium oxide films
ITO	Indium tin oxide
SECM	Scanning electrochemical microscope
SEM	Scanning electron microscope
TEM	Transmission electron microscope
XRD	X-ray diffraction
EDX	Energy dispersive X-ray spectroscopy
LC	Liquid crystal
LLC	Lyotropic liquid crystal
IUPAC	International Union of Pure and Applied Chemistry
SP	Surface plasmon
SPP	Surface plasmon polariton
DMF	Dimethylformamide
3D	Three dimension
θ	Tilt angle
$Ø_{IrOx}$	Coverage of IrOx film
$Ø_{ITO}$	Coverage of the ITO surface
a	The real film thickness
x	SEM measured length
Q	Charge

d	Diameter
D	Diameter
n	Number of electrons transferred
F	Faraday constant
A	Surface area
h	Film thickness/height
V	Volume of deposited film
d_m	Density of the film
M_w	Molecular weight
r	Radius of the film cavity
r_s	Radius of the sphere
T	Transmittance

1 Introduction

1.1 The overview of the thesis

The initial goal of this work was to fabricate a novel pH nanostructured microelectrode of iridium oxide which combines the advantages of microelectrodes, nanostructured films and iridium oxide. Microelectrodes are powerful tools for microscale studies. Materials used for solid-state pH electrodes are various: metal oxide [1-6], carbon fibres [7, 8] and optical fibre types [9, 10]. Metal oxide microelectrodes are almost free from cation interference [11]. Among all the metal oxides, the use of iridium oxide as the pH sensing microelectrode has many advantages. IrOx is very stable and does not undergo dissolution [12, 13]. IrOx electrodes show potential stability over a wide range of temperature and pressure in aqueous solution, a wide range of pH response, fast response and the lowest sensitivity to redox interference and stirring [14, 15]. The novel design of the nanostructured IrOx microelectrode provides the possibility of achieving a microelectrode with a high surface area/volume ratio, thus increasing the reactive surface area without compromising the size.

At the start of this research project, liquid crystal templates were employed to fabricate nanostructured IrOx films. However, the chemistry was too complicated and nanostructured IrOx films were not successfully made by this approach. Colloidal template was proposed and the results turned out to be more successful. Thus, the work was focused on preparation of nanostructured IrOx films with the colloidal templates. Nanostructured iridium oxide films were fabricated by electrochemical deposition within a template made with colloidal polystyrene spheres on gold substrates. SEM pictures show that the nanostructured IrOx films have a very ordered hexagonal structure. Optical results of nanostructured IrOx films show that IrOx is a potential tunable photonic crystal material due to its unique electrochromism, and the optical properties of nanostructured IrOx films were studied thoroughly in this work. This work mainly concerns two parts: the fabrication and characterisation of the nanostructured IrOx films and the optical application of the nanostructured IrOx films.

Chapter one introduces the literature background of all the aspects of the project: the templated deposition of nanostructured materials, the optical application of macroporous materials and the fabrication and properties of IrOx films. Chapter two provides the details of the experimental conditions used to perform the investigations. Chapter three describes the fabrication and characterization of the non-structured IrOx films. Chapter four describes the fabrication and characterization of the structured IrOx films via templated deposition and the improvements made to control the structure of the film. The electrochromism of IrOx films lead to potential applications in photonic crystals. Chapter five reports the optical study of the nanostructured IrOx films, including transmittance and reflectance measurements. Chapter six presents the results of experiments where IrOx films are deposited on nanostructured Au surfaces to control their optical properties and produce tunable surface plasmonic device. Chapter seven concludes the thesis. References are presented in Chapter eight.

1.2 Brief background of liquid crystal template and colloidal template

Materials with engineered periodic structures raise wide research interests due to their novel properties in various application areas including: high surface/volume ratio electrocatalysts [16, 17], microsensors [18-20], surface enhanced Raman Spectroscopy [21, 22], photonic crystals [23, 24] and quantum dots [25].

One novel method to synthesise these structured materials is the templated deposition. Two templating approaches involving electrochemical deposition have been successfully developed in the electrochemistry group in the University of Southampton: the lyotropic liquid crystalline templates and the spherical colloidal templates. Liquid crystals are the substances that exhibit a phase of matter that has properties between those of a conventional liquid and those of a solid crystal [26]**.** Liquid crystals (from now on referred to as LCs) have two types: the lyotropic liquid crystals and thermotropic liquid crystals. The thermotropic liquid crystals are the liquid crystals, the phase behaviour of which is changed by temperature [27]. Comparing to the thermotropic LCs, lyotropic LCs (LLCs) only form when the anisotropic molecules are dissolved in a solvent and their

phase behaviour is determined by the concentration of the molecules in the solvent as well as the temperature [27]. In 1995 Attard et al. [28] reported the templating of silica mesoporous nanostructures (defined as 2 – 50 nm pore diameter by IUPAC[1]) with the lyotropic liquid crystal phases formed by the non-ionic surfactants octaethylene glycol monodecyl ether ($C_{12}EO_8$) and octaethylene glycol monohexadecyl ether ($C_{16}EO_8$) in water. Attard and co workers [29] then developed this method to prepare for the first time mesoporous Pt films (denoted by H_I-ePt) with the hexagonal phase [30] LLCs formed by the non-ionic surfactant $C_{16}EO_8$. This pioneering work brings up a new field of mesoporous metals or metal based materials including: Co [31], metal alloys [32], Ni [33, 34], Pd [35], semiconductors [36] ans so on. Figure 1-1 below shows the phase evolution of the liquid crystals in a polar solvent while the concentration of the surfactant changes.

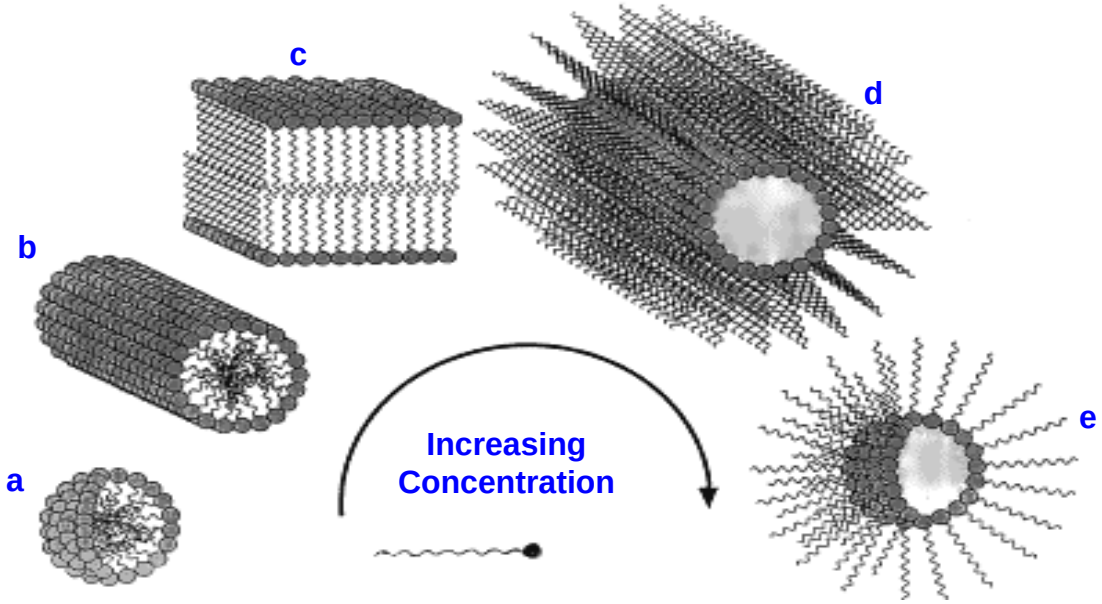

Figure 1-1: Schematic showing the aggregation of amphiphilic molecules into supramolecular structures when solvated in a polar solvent. Liquid crystal phases obtained: a) micellar, b) hexagonal, c) lamellar, d) inverse hexagonal and e) inverse micellar. Taken from reference [37].

[1] The International Union of Pure and Applied Chemistry (IUPAC) have proposed a specific nomenclature for porous materials according to the pore size as: macroporous materials (pore diameter >50 nm); mesoporous materials (pore diameter ~ 2 – 50 nm); and microporous materials (pore diameter ⩽ ~ 2 nm).

The demand for materials with larger pore sizes and the interest in the synthesis of three dimensional macroporous materials initiated the use of monodispersed colloidal spheres as the deposition template. The colloidal particles used in fabricating macroporous nanostructure materials have typical size ranging from 1 nm to 1 μm for silica and 20 nm to 100 μm for polymer spheres. Three dimensional ordered macroporous structures have been fabricated by employing close packed arrays of monodispersed spheres including polystyrene, polymethyl methacrylate or silica. Various materials such as metals [38, 39], metal oxides [40, 41], carbon [42], semiconductors [43], silica [44-46] and polymers [47-49] have been fabricated by this approach.

In contrast to the LLCs template, the colloidal template is easier to implement since it is a simple physical procedure and it is a convenient and versatile method for generating porous materials. The pore size produced by the colloidal template has a wide range of applications in optical devices and microsensors due to its sub-micrometer features. The pore size of the material made from these colloidal templates corresponds to UV-visible wavelength, thus, optical applications can be generated. Preliminary experiments were carried out to develop nanostructured IrOx films with LLCs templates but were unsuccessful. For this reason, the work reported in this thesis entirely focused on the fabrication of the nanostructured materials from the colloidal template, the characterisation and the applications of the nanostructured material. The following sections will describe the background, the formation, and the application of the colloidal sphere templates in details.

1.3 Colloidal Template

1.3.1 Monodispersed colloidal spheres

The best known natural materials made by an assembly of spheres are probably the opals, which are composed of monodispersed spherical silica particles [50]. The descriptions of preparations and of some properties of synthetic “monodispersed” colloids date back to Faraday who produced gold sols of different colours and recognized their particulate character [51]. Colloidal particles have a long history for applications as the major

components of industrial products such as foods, inks, paints, coating, cosmetics, and photographic films. They are also frequently studied in chemistry, material science and biology.

The most studied and popular two categories of colloidal particles are made from silica and latex. There is a wide range of chemical methods for preparing highly monodispersed colloids [51, 52]. The most commonly used methods include controlled precipitation from an inorganic oxide or the emulsion polymerisation of a polymer [53]. With these methods, monodispersed silica spheres with diameter ranging from a few nm to 1.0 μm and polymer latex spheres with diameter ranging from 20 nm to 100 μm have been synthesised. Figure 1-2 below shows two transmission electron microscopy (TEM) images of such colloidal spheres: silica spheres with diameter of 400 nm and polystyrene beads with diameter of 200 nm.

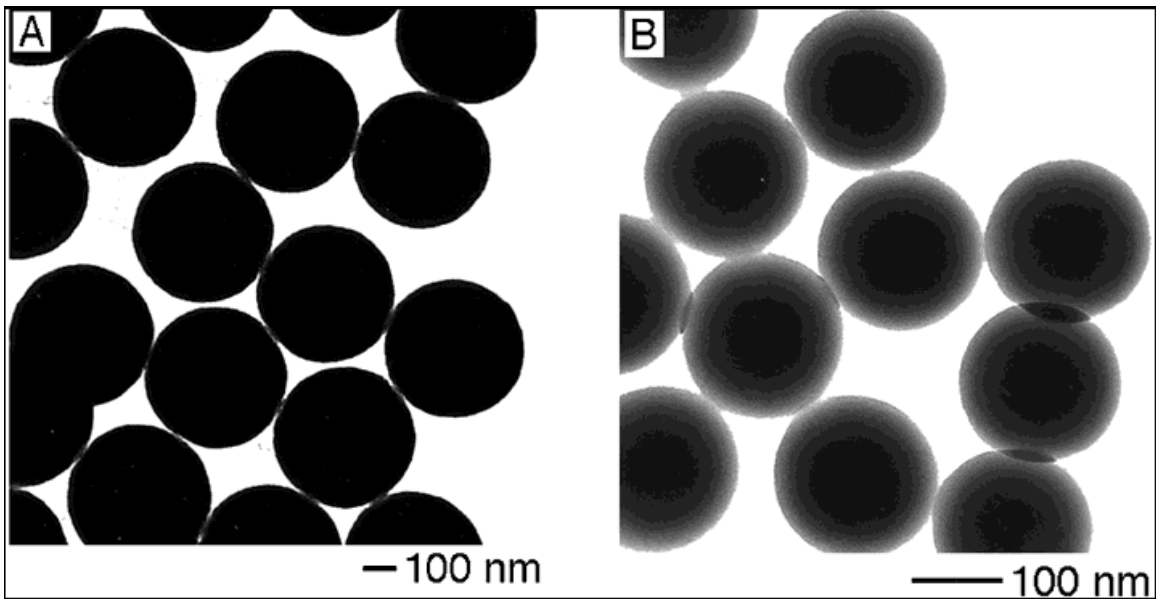

Figure 1-2: The TEM images of two representative colloidal systems that can be readily prepared as monodispersed samples at large quantities: A) ~ 400 nm silica spheres; and B) ~200 nm polystyrene beads. Images taken from reference [53].

In order to avoid the spheres aggregating together, the surface of the spheres should be treated with either positively of negatively charged functional groups. The surface of silica spheres was treated with silanol groups (-Si-OH); while the surface groups for polymer latexes spheres are based on three categories: acid groups e.g. –COOH, $–SO_4H$, $-SO_3H$; basic groups e.g. $–NH_2$, -OH, and epoxy groups. The polarity of these surface groups can be altered by changing the pH value of the dispersion medium as shown in Figure 1-3 below [54].

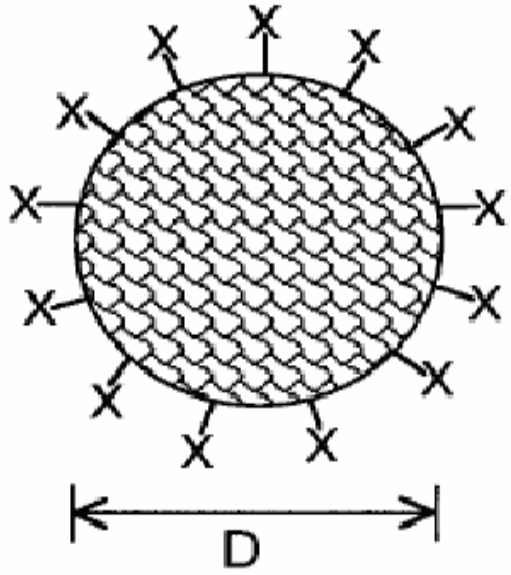

Figure 1-3: Schematic illustration of a solid sphere. The size of the surface groups, X has been exaggerated. The polarity and density of charges on a colloidal sphere are mainly determined by the surface group. Image taken from [53].

Spherical colloidal particles of polymers or silica with different diameters are readily available from commercial suppliers [55]. The spheres are usually supplied as stabilised suspensions in either water or organic solvents.

1.3.2 Formation of 2D arrays from colloidal spheres

In order to use the colloidal spheres as the template for further application, monodispersed colloidal spheres are self-assembled into ordered 2D or 3D arrays on solid

supports or in thin films of liquids. There are a number of strategies to self assemble colloidal spheres into 2D arrays [54, 56-58]. Figure 1-4 shows the schematic diagrams of

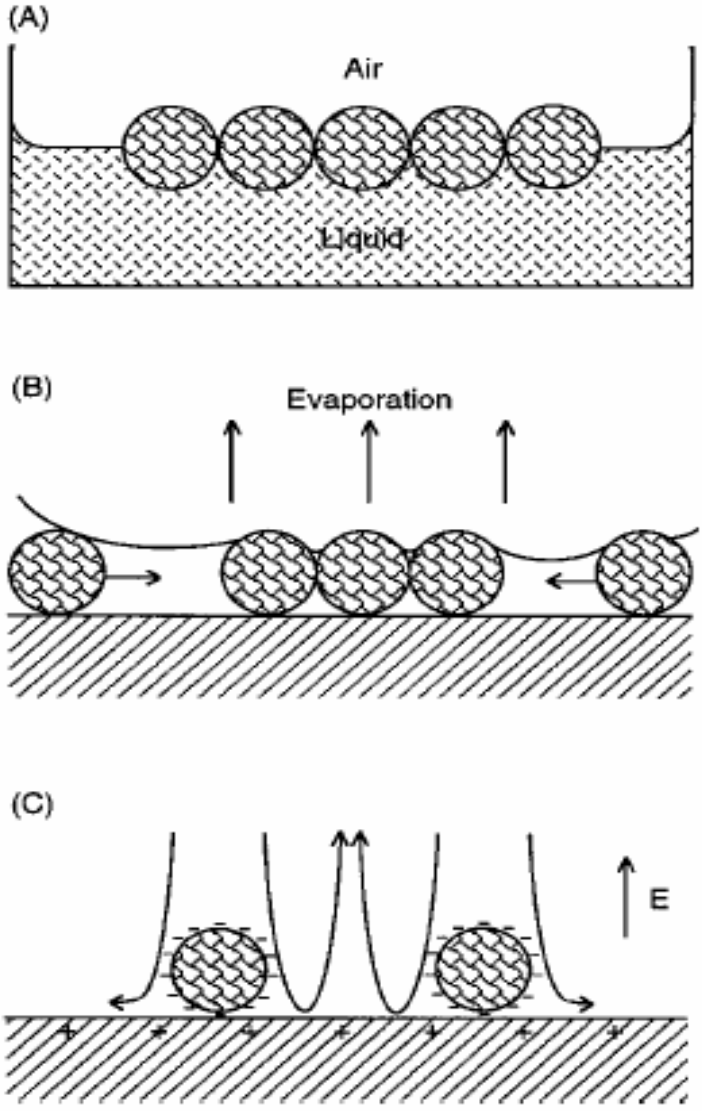

Figure 1-4: Schematic illustrations of three approaches that have been demonstrated for organizing monodispersed colloidal spheres into 2D hexagonal arrays: A) at the air/ liquid interface via long-range attractive interactions [59, 60]; B) in a thin liquid film spread on a solid substrate via attractive capillary forces [57, 61-63]; and C) on the surface of a solid electrode via electrophoretic deposition[64, 65] .E is the electric field applied. The two arrows in C) indicate the force that draws the spheres towards each other. Image adapted from [53].

three approaches, in which methods colloidal spheres have been assembled into closely packed 2D hexagonal arrays.

In the first method (Figure 1-4 A), a 2D array of colloidal spheres is organised at the air / liquid interface and then this array can be transferred onto a surface of a solid substrate. The strong interaction among the colloidal spheres leads to the spontaneous formation of a 2D aggregate at the interface.

The second method was explored by Nagayama and co-workers [57, 61], who found that neither the electrostatic repulsion nor the Van der Waals attraction between the particles is responsible for the formation of two-dimensional crystals; the latter is instead driven by attractive capillary forces and the convective transport of particles. In a typical experiment, a liquid dispersion of colloidal spheres is spread onto the surface of a solid substrate[61]. When the solvent evaporates slowly under a controlled condition, the colloidal spheres are self-assembled into a closely packed, hexagonal array as shown in Figure 1-4 B. Nagayama and co-workers followed this self-assembled process with an optical microscope as shown in Figure 1-5 below. They found that a nucleus, recognised as an ordered region that consists of a number of colloidal spheres, was first formed when the thickness of the liquid layer approached the diameter of the colloids. More colloids were driven toward this nucleus by a convective transport, and eventually organised around the nucleus by the attractive capillary forces.

Later on, Colvin and his co-workers [38] demonstrated the capability and feasibility of this approach in forming 3D opal lattices with well-controlled numbers of layers. The third approach is usually referred as electrophoretic deposition [66, 67]. In this approach (Figure 1-4 C); a liquid dispersion of colloidal spheres is confined between two parallel solid electrodes. In the presence of an efficient electric field, the colloidal spheres that were originally randomly deposited on the anode will move towards each other to form a stable 2D hexagonal array. Two arrows in Figure 1-4 C indicate the electric force which draws spheres to each other.

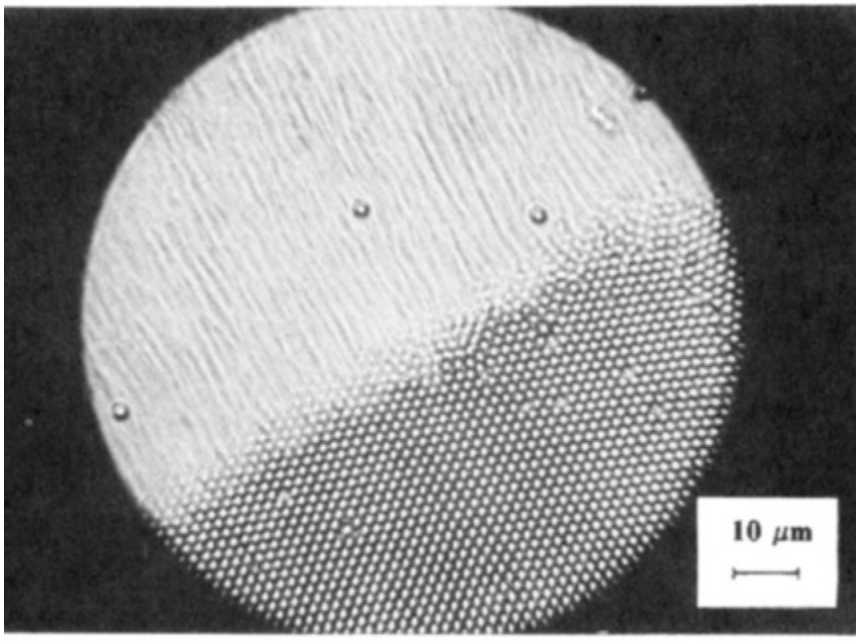

Figure 1-5: Photograph of the 2D ordering process for the colloidal spheres. The particles ("worms" in the upper left part of the photograph) are moving toward the ordered phase, building up the hexagonal array (lower right). Image adapted from reference [61].

1.3.3 Formation of 3D arrays from colloidal spheres

A variety of methods are available for organizing monodispersed colloidal spheres into highly ordered 3D arrays. A simple method of creating colloidal crystals is gravity sedimentation of colloids from dispersion [68-71]. This method involves several processes such as gravitational settling, translational diffusion (or Brownian motion), and crystallization (nucleation and growth). Monodispersed silica colloids are the most commonly employed in sedimentation due to the high density of silica.

The other method is the crystallisation based on repulsive electrostatic interactions. Under proper conditions, highly charged colloidal spheres suspended in a dispersion medium can spontaneously organise themselves into a wide range of crystalline structures as driven by minimisation of the repulsive interactions. These ordered 3D arrays are often referred as colloidal crystals [71]. This method seems to be the most powerful and successful route to produce large scale 3D crystalline arrays. However, this method has a very strict requirement on the experimental conditions: such as the temperature, monodispersity in size, density of spheres, density of charges on the surface of each sphere and the concentrations of counter-ions in the dispersion medium [53].

Another approach particularly applied in polymer colloids uses the flow of a solvent through micromachined channels to create dense colloidal arrays of multilayers, that was known as the self-assembly under physical confinement [72, 73]. In this approach, colloidal spheres with a diameter ranging from 50 nm to 1 μm were assembled into highly ordered structure in a specially designed packing cell. The key to success of this method is a continuous sonication. Figure 1-6 demonstrates these three approaches for organising 3D arrays from colloidal spheres.

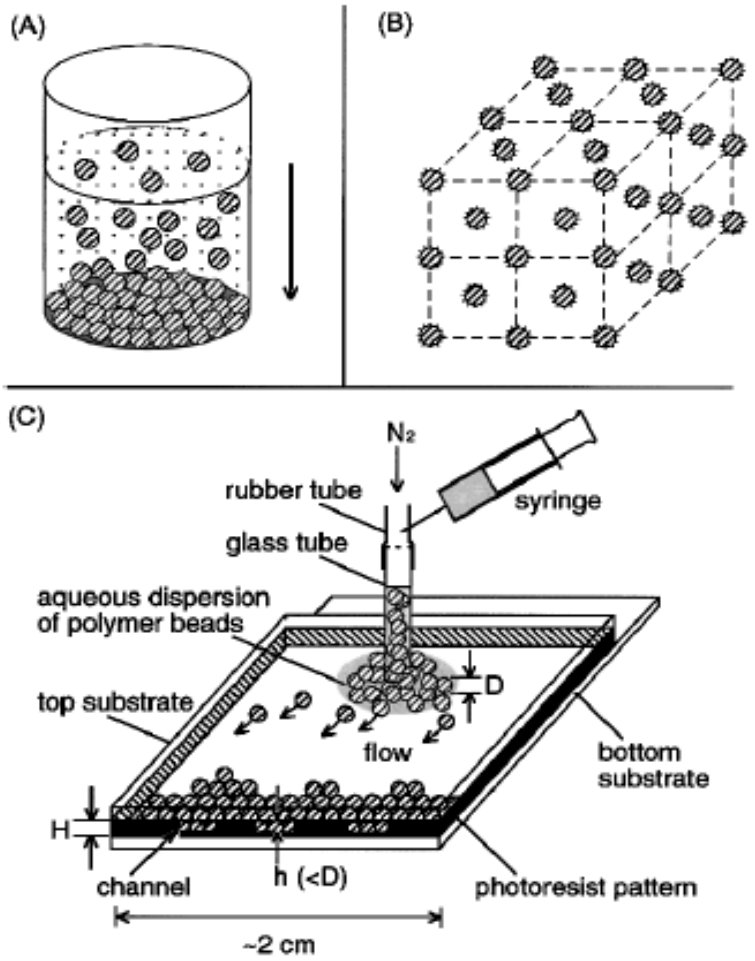

Figure 1-6: Schematic outlines of three experimental methods used to assemble colloidal spheres into 3D crystalline lattices: A) sedimentation by gravity [74, 75]; B) self assembly via repulsive electrostatic interactions [76]; C) crystallization through physical confinement and hydrodynamic flow [48, 77, 78]. Image taken from [53].

1.3.4 Deposition of nanostructured materials through colloidal templates

Templated synthesis of macroporous materials is a convenient and versatile method. A wide range of porous materials including metals, metal alloys, metal oxides, and organic polymers have been synthesised with this method. Figure 1-7 shows SEM images of

several typical examples of 3D porous materials that were fabricated by templated synthesis, they are: macroporous thin films of polyurethane, SiO_2, SnO_2, and TiO_2.

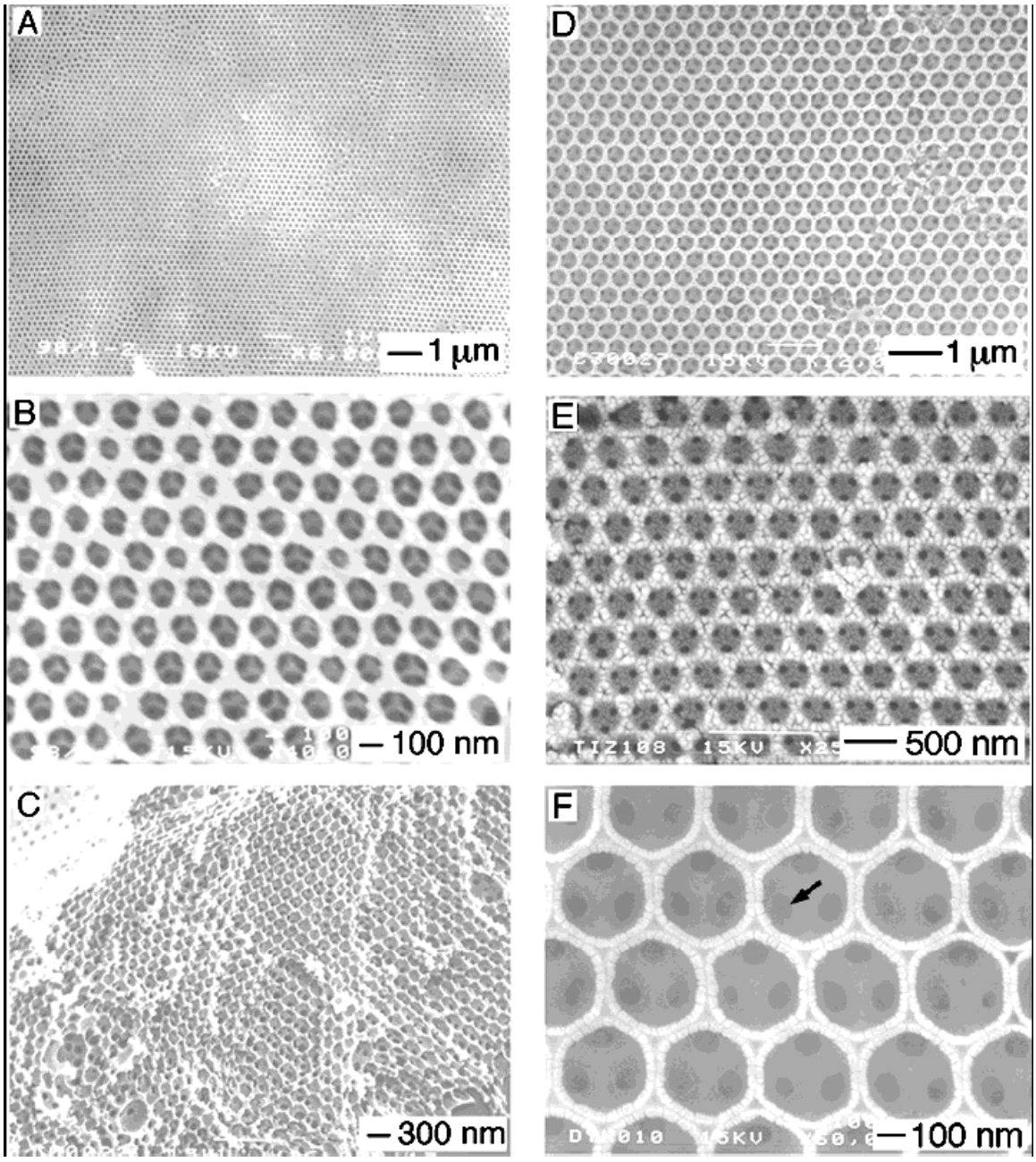

Figure 1-7: SEM images of 3D porous materials that were made of: A-C) polyurethane; D) SiO_2; E) SnO_2; and F) TiO_2. Picture adapted from [43, 48, 49, 79].

In terms of metal oxides, nanostructured oxides of Ni, Zn, Si, Ti, Zr, Al and Fe have all been obtained by filling the space between close packed arrays of polystyrene or silica spheres with a precursor solution which is then either chemically or thermally converted to a solid oxide skeleton around the spheres. Table 1 below gives a partial list of those 3D porous materials that have been fabricated and characterised.

Table 1-1-1: Macroporous materials fabricated by templating against 3D colloidal arrays, table modified from reference [53]

Template	Porous materials	Precursors	Comments	Reference
Polymer beads	Polyurethanes, poly(acrylate-methacrylate) copolymers	UV-curable prepolymers	Extraction with solvents, ordered	[48, 49, 79]
	Au	Gold nanoparticles	Extraction with solvents, partially ordered	[39]
	Au, Ag, Pt, Pd, Ni, Co, ZnO, PbO_2, semiconductors, conducting polymers	Electrodeposition	Dissolved in organic solvents, ordered	[80-88]
	Ni, NiO	$(CH_3CO_2)_2Ni$	Calcination, partially ordered	[89]
	SiO_2	Snowtex Zl and OL	Calcination, ordered	[90]
	TiO_2	Titania nanoparticles	Calcination, ordered	[90, 91]
	SiO_2, ZrO_2, $Al_2O_3{\cdot}H_2O$, WO_3, Fe_2O_3, Sb_4O_6,	Metal alkoxides and metal	Calcination or extraction with	[40, 41, 45, 46, 79, 92,

	Nb_2O_5, $AlPO_4$, TiO_2, ZrO_2	chlorides	solvents, ordered or partially ordered	93]
Silica colloids	Organic polymers	Organic monomers	HF etch, ordered and partially ordered	[47, 79, 94, 95]
	Carbon	Thermally cured phenolic resin, or chemical vapour deposition	HF etch, ordered	[42]
	Ni, Cu, Ag, Au, Pt	Electroless deposition on gold nanoparticles	HF etch, ordered	[38]
	CdS, CdSe	$CdSO_4$, SeO_2	HF etch, ordered	[43]
	CdSe	CdSe nanoparticles	HF etch, ordered	[96]
Emulsion templating	Polyacrylamide	$H_2C=CHCONH_2$ and $(H_2C=CHCONH_2)_2CH_2$	Drying, disordered	[97]
	SiO_2, TiO_2, ZrO_2	Metal alkoxides	Drying, calcinations, disordered	[97, 98]

In this work, electrochemical deposition was employed to synthesize macroporous nanostructured IrOx films. Electrochemical deposition has significant advantages, particularly for the deposition of thin, supported films of macroporous materials. First, electrochemical deposition can be used to prepare a variety of materials from both aqueous and non aqueous solutions under conditions which are compatible with the template. Second, electrochemical deposition allows fine control of the film thickness of the resulting macroporous film by controlling the total charge passing during the deposition of the film. Third, the electrochemical deposition is an ideal approach for the production of the thin supported layers for applications including photonic mirrors since the surface of the electrochemical deposition can be very uniform.

The first example of electrochemical deposition through a colloidal template was produced by Braun and Wiltzius [43]. In their report, CdS and CdSe were electrochemically deposited through a 466 nm diameter polystyrene spheres template on an indium tin oxide electrode. Nanostructured metal films (Pt, Au, Ag, Co, Nickel tin, Co alloy) and conducting polymers were fabricated using this approach [80-88]. Sumida and Ghanem have obtained nanostructured macroporous ZnO and PbO_2 films respectively [85, 99]. However, there are fewer reports in electrochemical deposition of nanostructured metal oxide films.

1.4 Optical applications of nanostructured materials

1.4.1 Surface plasmon and plasmon modes on nano-void substrates

Surface plasmons are collective oscillations of the free electron gas density, often at optical frequencies [100-102]. Surface plasmons, also known as surface plasmon polaritons (SPPs), are surface electromagnetic waves that propagate parallel along a metal/dielectric (or metal/vacuum) interface. Surface plasmons are of interests to a wide

spectrum of scientists ranging from physicists, chemists, material scientists to biologists. For instance, surface plasmons were explored in optics, microscopy and solar cells, as well as used by biochemists to study the mechanisms and kinetics of ligands binding to receptors [100]. More recently surface plasmons have been used to control the colours of materials [103].

Surface plasmons cannot be generated on a flat surface by optical fields due to an electromagnetic momentum mismatch with photons. There are three methods in which this momentum mismatch could be solved: (a) scattering from a defect on a surface; (b) scattering from a periodically corrugated metal surface such as a diffraction grating [100]; and (c) using a prism for coupling.

The SPP mode can not only provide the extra momentum to help couple a photon into the surface but also decay and radiate a photon by losing momentum to the surface as represented in Figure 1-8.

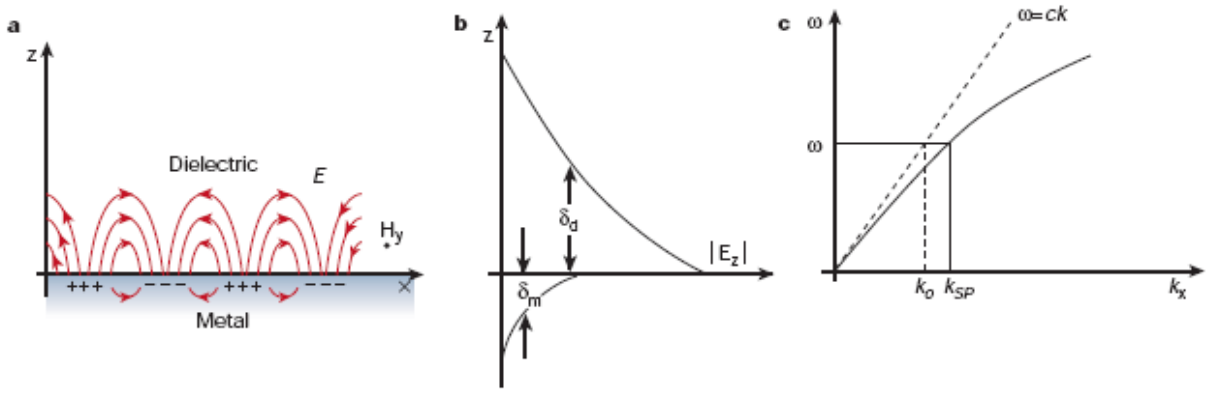

Figure 1-8: Surface plasmons at the interface between a metal and a dielectric material (SPPs) have a combined electromagnetic wave and surface charge character as shown in ***(a):*** *They are transverse magnetic in character, and the generation of surface charge requires an electric field normal to the surface. This combined character also leads to the field component perpendicular to the surface being enhanced near the surface and decaying exponentially with distance away from it* ***(b)****: The field in this perpendicular direction is said to be evanescent, reflecting the bound, non-radiactive nature of SPs, and prevents power from propagating away from the surface. In the dielectric medium above the metal, typically air or glass, the decay length of the field,* δ_d*, is of the order of half the wavelength of light involved, whereas the decay length into the metal,* δ_m *is determined by the skin depth.* ***(c):*** *The dispersion curve for a SP mode shows the momentum mismatch problem that must be overcome in order to couple light and SP modes together, with the SP mode always lying beyond the light line, that is, it has greater momentum than a free space photon of the same frequency ω. Adapted from reference [100].*

By altering the structure of the metal surface, the properties of the surface plasmons, in particular the interaction with light can be tailored. There has been increasing interest in SPPs on nanostructured surfaces in recent years since the first discovery of a 2D SPP band gap [104]. Barns and co-workers found that if the periodicity of the structure is half the effective wavelength of the SPP an energy gap is formed. Consequently, the high enhancement of electric fields can occur at the edges of the band gap. In general, the existence of SPP modes on nanostructured surfaces can generate large increases in

optically produced local electric fields on the surface under proper conditions [102]. Surface- enhanced Raman Spectroscopy (SERS) – a sensitive technique now can detect a single molecule has been particularly applied in these substrates [105, 106].

In the electrodeposition approach of templated syntheses of nanostructured materials, the controlling of the charge passed during deposition can generate a number of different and complex morphologies of the nanostructured materials. The structure can vary from an array of shallow dishes, disconnected voids, to almost encapsulated air spheres. The interaction and coupling with optical fields within these different structures can generate different plasmon modes. Below is a brief introduction of these plasmon modes based on current understanding [107].

When the thickness of samples is less than 0.3 *d* (thickness normalised with the sphere diameter *d*), the surface forms a hexagonal array of shallow dishes. SPP modes are observed when surface plasmons couple to incident light. These states multiply scatter at the rims of the dishes – modelled with Bragg diffraction, forming plasmonic band gaps similar to those formed in 2D dielectric photonic crystals [107]. Since, the surface is anisotropic their energies strongly depend on the angle of incident radiation and the direction of propagation [108]. These are delocalised modes which can travel several microns on gold and silver before decaying. Only pure Bragg modes are observed on these thin samples. The Bragg modes disappear as the top surface breaks into islands and reappear when the thickness is above 0.75 *d*. There are two plasmon modes when the film thickness is above 0.75 *d*: Bragg plasmons supported on the flat connected surface and Mie Plasmons localised in the voids (the surface plasmon polaritons will be termed as Bragg Plasmons since their coupling is via Bragg diffraction and the localised plasmons will be termed as Mie Plasmons).

The Mie plasmon modes only occur when the film thickness increases above 0.3 *d*. The high energy localised plasmons are observed as trapped inside the voids. When a SPP wave is reflected between barriers in the spherical cavity, it will interfere with itself and form a localised mode. The energies decrease as the thickness increases. These void

plasmons are called Mie Plasmons as modelled using the Mie scattering theory [109, 110]. The Mie plasmon wave functions correspond to spherical harmonics similar to atom orbitals, labelled by angular and azimuthal quantum numbers (l, m respectively). Since the voids are symmetric and nearly isotropic, the Mie plasmons are independent of the angle of incident light and their electric fields are not influenced by those from the neighbouring voids. As the voids get deeper, the energy of Mie plasmons decreases.

Between shallow dishes and fully encapsulated voids, the film surface breaks up into disconnected islands interspersed with voids. The Bragg modes start to disappear just below 0.5 d film heights and reappear when the islands reconnect above 0.75 d film heights. When the film structure is between these two heights, mixed modes are observed. As the voids get deeper, the energy of Mie plasmon modes drops from the two dimensional plasmon around 2.5 eV, down through the propagating Bragg modes. It is strong coupling between these modes that controls the plasmon properties on the nanostructured surface. The energy levels split as the bonding and anti-bonding orbitals except that it is the coupling between delocalised and localised plasmons. The Bragg plasmons can be tuned by a variation of sphere size since they depend on the periodicity of the sample. And the Mie plasmons can be tuned by changing the film height. Figure 1-9 below shows the surface and localised plasmons (Bragg and Mie Plasmons) on nanostructured gold surfaces.

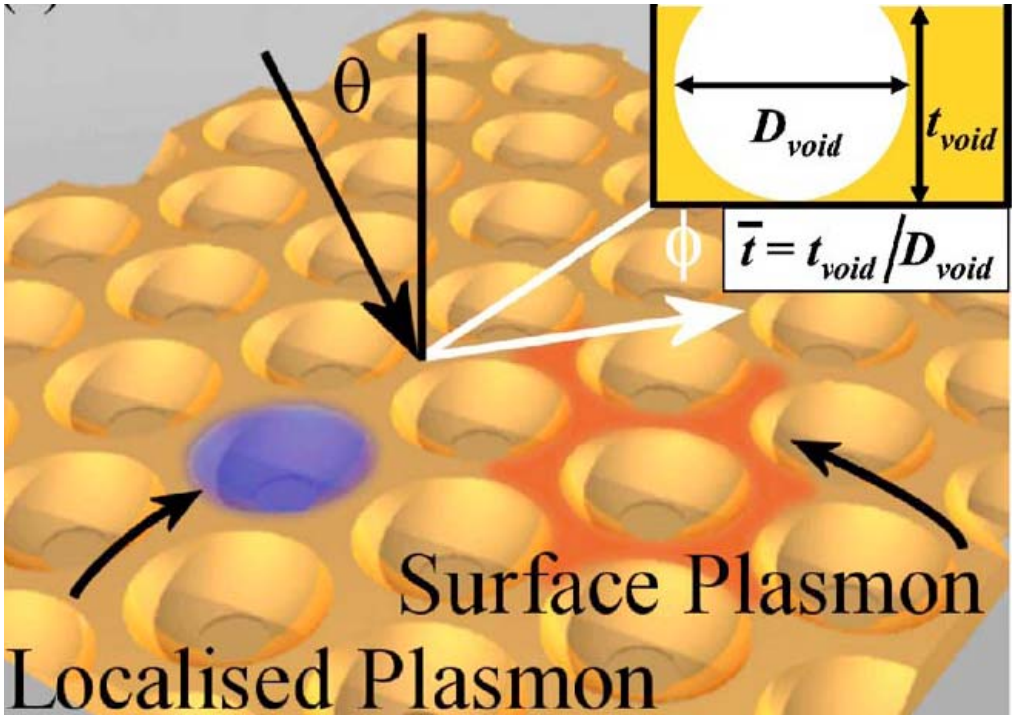

Figure 1-9: Schematic of surface- and localized plasmons on nanostructured gold surfaces. Inset shows definition of normalized thickness [21].

Surface plasmon modes on nanostructured materials generate a wide range of extraordinary properties, and therefore lead to many applications. For example, these surfaces are ideal for Surface-Enhanced Raman Spectroscopy (SERS) which is strongly enhanced in the localized Mie regime [111] They are also promising in commercial production for a variety of applications in medical and pharmaceutical screening and environmental monitoring.

1.4.2 Photonic crystals

1.4.2.1 The concept of the photonic crystal

Recently, photonic crystals have received a lot of research attention due to their unique property in manipulating photons [112]. Photonic crystals were first proposed by Yablonovitch and John in 1987 [113]. A photonic crystal is an artificial composite of dielectric materials and air with a periodicity in the order of the wavelength of light

which diffracts light over a certain range of frequencies. In such photonic crystals, the propagation of light within a certain frequency range is forbidden irrespective of the direction of propagation, thus causing a photonic band gap [114]. The width of photonic band gap increases with the increasing of dielectric constant. It is a measure of the strength of the interaction between light and the photonic crystal [115, 116].

A prominent example of naturally occurring photonic crystals is gemstone opal. It consists of silica spheres which have sub-micron diameter and are arranged in a face centered cubic close packed structure. The bright colours result from a photonic crystal phenomenon based on Bragg diffraction of light on the lattice planes of crystals. Another well-known example of photonic crystals is the wings of some butterflies such as those of genus Morpho. Figure 1-10 (a) shows a photograph of Morpho butterfly, the iridescent blue wings are due to diffraction periodic structures in the scales of the wing. Figure 1-10 (b) shows a TEM image of the wing-scale cross session of the Morpho butterfly.

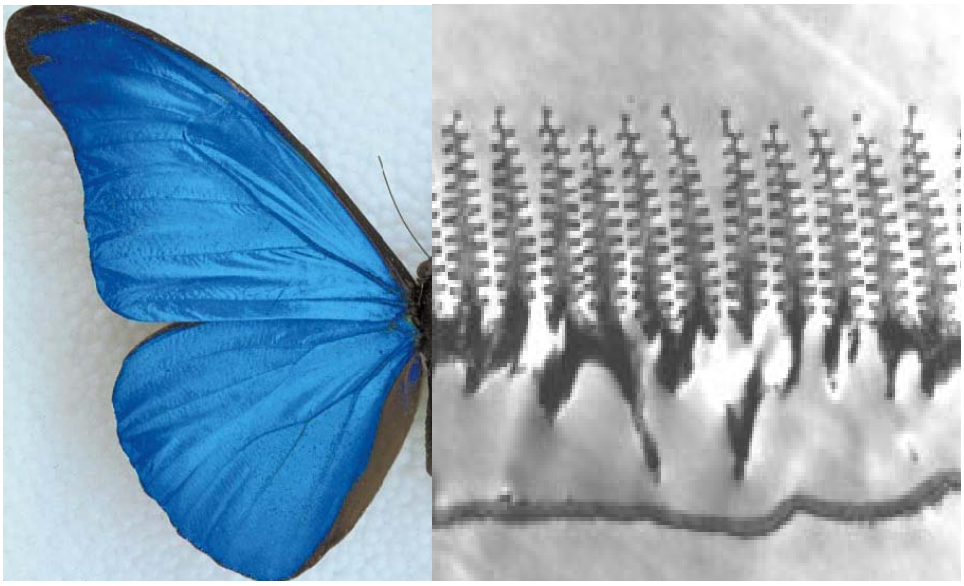

Figure 1-10: a) Blue iridescent wings of Morpho butterfly; b) Transmission electron microscope(TEM) image of the wing-scale cross section adapted from reference [117]. Scale a: 1 cm, scale b: 1.8 µm.

1.4.2.2 Types of photonic crystals

There are basically three types of photonic crystals. A one-dimensional photonic crystal is the simplest possible type of photonic crystals. It consists of alternating layers of materials with different dielectric constants. When light interacts with such a layered structure material, light of appropriate wavelength is completely reflected. That is due to the light wave scattering at the layer interfaces and the layer spacing matching the wavelength of the light. The multiple scattered waves interfere destructively inside the material. This one-dimensional photonic crystal is well known for applications of dielectrical mirrors and optical filters since it can act as a perfect mirror for light with a frequency within a sharply defined range.

The other type of photonic crystals is a two-dimensional photonic crystal which is periodic along two of the axes and homogeneous along the third. A typical mode is a stack of cylinders of given dielectric constant as shown in Figure 1-11. An example is the case of a photonic crystal fibre, one possible geometry of which is a number of fibres stacked together in a manner to make a bundle of fibres [118].

Another one is a three-dimensional photonic crystal in which the dielectric composition is modulated in three dimensions as shown in Figure 1-11. Such a system can manifest a full photonic band gap where wave propagation is forbidden in any direction and for any polarisation over the range of light wavelength (400 nm – 800 nm). There have been many attempts to fabricate photonic crystals working at optical frequencies.

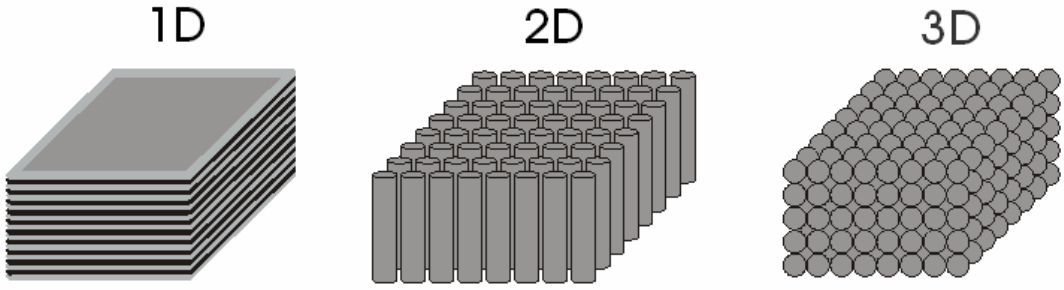

Figure 1-11: Real-space representation of photonic crystals, from left to right: one-dimensional photonic crystal, two-dimensional photonic crystal and three-dimensional photonic crystal. Adapted from reference [119].

In 1996, Gruning et al. [120] electrochemically etched silicon to produce a photonic crystal, while Krauss et al. [121] performed lithography on AlGaAs to obtain photonic a band gap at λ= 850 nm. Colloidal crystals assembled from charged silica or polystyrene spheres with diameter ranging from 100 to 1000 nm have been proposed as a possible routine to create 3D photonic crystals [122-127]. Lopez and co-workers [70, 128], Vlasov and co-workers, Zhang and co-workers [123] and Colvin and co-workers [94] have extensively investigated the photonic properties of artificial opals fabricated from monodispersed silica colloids. Further more, Lopez and co-workers and Xia and co-workers studied the capability to fine tune the stop band of the 3D crystalline array fabricated from Polystyrene beads or silica beads by sintering the samples at elevated temperatures [69, 129].

However, artificial opals have a narrow photonic bandwidth since the refractive index contrast between silica spheres and air is small. Computational studies have suggested that a porous material consisting of an opaline lattice of interconnected air balls (embedded in an interconnected matrix with a higher refractive index) could give rise to a complete gap in the 3D photonic band structure [130]. Thus, silica or polystyrene spheres have been used as templates to synthese inverted opal structures consisting of three-

dimensional regular spherical air holes imbedded in a dielectric medium with high refractive index as shown in Figure 1-12.

Figure 1-12: Three-dimensional visualisation of a fcc inverse opal photonic crystal, the spherical air spheres imbedded in the dielectric matrix are non-overlapping and each of them is connected to all of its 12 nearest neighbours by air tunnels, image taken from [131].

The dielectric medium could be metal [132, 133], metal oxide [24, 90, 91, 134, 135], carbon [136-138], polymer [139, 140] or semiconductors [141, 142]. To the best of our knowledge, there is only one report of inverse opal 3D photonic crystal fabricated with electrochromic material. Electrochromic tungsten trioxide WO_3 inverse opals have been fabricated by polystyrene colloidal crystal templating to study the tunable photonic stop band gap induced by electrochromic property [112].

1.5 The fabrication, properties and applications of IrO_x films

1.5.1 IrOx films

Numerous papers on iridium oxide films were written due to a wide range of applications in pH sensors [15, 143-151], electrochromic devices [152, 153], H_2O_2 detectors [154], microsensors [155], electrocatalytic sensors [156] and neural stimulations [157-162]. Iridium oxide films are known to have a super-Nernstian (> 59 mV / pH) pH sensitivity [163] and remarkable stability in both acidic and basic solutions. Among metal oxides iridium oxide is the most widely used for pH sensing. IrOx has also been used to make microscopic pH sensor as a SECM probe [7].

Methods for the fabrication of iridium oxide films include electrochemical growth on iridium wires [164], anodic electrodeposition [165], thermal salt decomposition [166], reactive sputtering [167], melt oxidation [168], sol-gel methods [169], and direct oxidation from iridium wire [170]. The substrates used for depositing iridium oxide layers are also numerous. Pure iridium, glassy carbon, gold, and titanium are frequently used substrates.

IrOx nanocrystals and nanorods have been fabricated [171, 172]. To the best of our knowledge, the fabrication of macroporous nanostructured IrOx film has not been reported.

1.5.2 Deposition methods for fabrication of IrOx films

A wide range of deposition methods has been reported for fabrication of IrOx films. Four frequently used methods are briefly reviewed below.

Hydrous IrOx films can be grown electrochemically by continuous cycling or pulsing between specific upper and lower potential limits on an Ir metal substrate, either a metal wire or a metal foil [173]. Although it is a simple and easily controlled method, electrochemical growth of IrOx film is highly costly since Ir metal is very expensive.

Reactive sputtering of IrOx film is normally operated in Ar/O_2 plasma using commercial equipment [174]. Argon ions are accelerated by an outside dc electric field toward a cathode (a target made from the coating material). Single cathode atoms are sputtered by the incident ions and then deposited on a suitable substrate. By adding adequate reactive gases, it is possible to deposit a combination of elements or compounds including iridium oxide films. When sputtering IrOx films, the concentration of the oxygen in the sputtering plasma is one of the important factors. However, the real oxygen concentration during the sputtering is difficult to monitor [175].

The sol-gel process is an attractive method for preparing metal oxides especially mixed metal oxide [176]. The sol-gel process involves metal alkoxides or metal salts as raw materials and some kinds of alcohol as organic solvents [169]. The most conventional method for sol-gel preparation of iridium oxide films is using a coating solution made from iridium chloride and ethanol. During the preparation, the coating substrate is heat treated to more than 100 ^{o}C [169, 176, 177]. It is not a suitable method when using a polystyrene template to make a nanostructured IrOx film since the polystyrenes spheres melt at around 90 ^{o}C.

Electrochemical deposition produces IrOx deposits either by reduction of hexachloroiridates or by oxidation of some iridium complexes [165, 178-181]. The deposition solution is easily synthesised and it is suitable for coating a large substrate. The deposition solution can be used with various electrochemical techniques.

Comparing the advantages and the disadvantages of each method, it is possible to select the most suitable one to achieve the goal of the project.

1.5.3 Electrochemical deposition of IrOx

In this work, an inexpensive electrochemical approach would be preferred to be used to synthesise macroporous IrOx films. The electrochemical deposition of macroporous

materials has the least drawbacks among all the templated deposition methods. A few electrochemical methods of fabrication IrOx films have been described [178-182]. Cox and co-workers [179] produced IrOx deposits by reduction of hexachloroiridates, while Yamanaka employed the route of oxidation of iridium complex.

Two reported methods for the direct deposition of an iridium oxide film in alkaline solutions were used in this work. These methods suggest that electrochemical deposition of nanostructured iridium oxide films is feasible. Yamanaka [180, 181] produced an iridium oxide film with anodic deposition using a solution containing iridium chloride, oxalic acid and sodium carbonate. Baur and co worker [165] fabricated a glassy carbon-iridium oxide electrode from a basic solution of saturated Ir (III) oxide. In this research, both methods have been carried out and compared in order to find the better choice for the purpose of fabricating nanostructured films.

1.5.4 The electrochromic property of IrOx films

Electrochromism is the process by which a material exhibits reversible and persistent colour change following a change in oxidation state induced by an electric current or applied potential [183]. Electrochromic materials switch from the uncoloured state to the coloured state by simultaneous ion and electron injection/extraction. This property has wide applications in energy efficient smart windows [184], electrochromic devices e.g. rear view mirrors in cars, and transmittance cells [181].

Many electrochromic materials have been reported e.g. tungsten oxide [185-188], nickel oxide [189-192], molybdenum oxide [193, 194], niobium oxide [195, 196], etc. IrOx is one of the well studied electrochromic materials. IrOx films display pronounced electrochromism and respectively bleach/colour, when ions are intercalated/ deintercalated. The electrochromism mechanism of IrOx has been the object of controversy in the past. Nevertheless, it is now generally agreed that the optical effects are due to ion intercalation/deintercalation as for Mo-oxide and W-oxide. Some earlier researchers [197-199] claimed that the electrochromism in IrOx would be entirely

dependent on the electronic nature, which has since been disapproved [200]. Essentially two mechanisms have been put forward for electrochromism of anodic films in aqueous electrolytes [200]:

1) cation mechanism requiring colouration via proton extraction;
2) an anion mechanism requiring colouration via hydroxide ion insertion

These two mechanisms are both applied depending on the pH value of the electrolytes.

The electrochromic properties of IrOx films produced from different approaches have been widely investigated. More commonly, the electrochromism of iridium oxides prepared by sputtering method [201] and sol-gel process [169] have been studied. Patil and co-workers [200, 202] for the first time used the simple and inexpensive pneumatic spray pyrolysis technique to prepare iridium oxide and investigate the electrochromism of IrOx films. The following colouration and bleaching process is proposed for spray deposited IrOx thin film:

$$Ir(OH)_3 - H^+ - e^- \underset{\text{bleach}}{\overset{\text{colour}}{\rightleftharpoons}} IrO_2 \cdot H_2O$$

at 0.7 V vs. SCE *Equation 1-1*

Or

$$Ir(OH)_3 + OH^- - e^- \underset{\text{bleach}}{\overset{\text{colour}}{\rightleftharpoons}} IrO_2 \cdot 2H_2O$$

at 0.7 V vs. SCE *Equation 1-2*

According to the above equations, it can be concluded that extraction of protons and electrons from the film leads to colouring while insertion of protons and electrons into the film causes bleaching.

In chapter 1, the literature background of the project has been reviewed from the templated deposition of nanostructured materials to the optical applications of those macroporous materials to the fabrication and property of IrOx films. With the

understanding of the project background, Chapter two will describe the experiment set-up for the fabrication and characterisation of both nanostructured and non-structured IrOx films. It will also describe the experimental details for the investigation of the optical properties of IrOx films.

2 Experimental

2.1 Generalities

2.1.1 Reagents and solutions

Iridium complexes ($IrCl_4$ 99.95%, $IrCl_3$ 99.99%) were obtained from Alfa-Aesar. Isopropanol (reagent grade), dimethylformamide (DMF, reagent grade), Acetone (reagent grade), and Ethanol (reagent grade) were purchased from Fisher Scientific. Cyclohexane (99.99%) and cysteamine hydrochloride were obtained from Aldrich. Hydrogen peroxide (30%, unstabilised, A.C.S., Fluka), alumina powders (Buehler), Parafilm (Pechiney Plastic Packing), KCl (>99.5%, BDH) were used in the work. All reagents were used as received without further purification. They were all AnalaR grade or above. Argon gas was obtained from BOC. 1 M or 0.5 M sulphuric acid wad prepared from concentrated sp.gr. 1.84 acid, >95%, BDH) and 1 M or 0.5 M Na_2CO_3 solution was made from Na_2CO_3 powder (AnalaR BDH).

The templates were made of monodispersed polystyrene latex spheres (Duke Scientific Corporation) supplied as a 1 wt. % solution in water. Before use, the suspensions were homogenized by successive, gentle inversions for a couple of minutes followed by a sonication for 30 s. The commercial cyanide free gold plating solution (Tech. Gold 25, containing 7.07 g / L gold) was obtained from Technic Inc. (Cranston, RI, USA).

All aqueous solutions were prepared using purified water from a Whatman RO80 system combined with a Whatman STILLplus carbon filter.

2.1.2 Glassware and electrochemical cells

All glassware was cleaned with 5% Decon90 solutions and rinsed thoroughly with purified water before use. The glass cells for electrochemical measurements were constructed by the glass-blower.

2.1.3 Instrumentation

All the pH measurements were carried out with a Mettler Toledo 320 pH meter. Three-electrode voltammetric measurements were performed with a PPR1 waveform generator (Hi-Tek) and a homemade potentiostat whereas two-electrode voltammetry was carried out with a PPR1 waveform generator and a homemade current follower. Care was taken to avoid electrical noise and all experiments were carried out in an aluminium Faraday cage connected to the earth. All connections were made with BNC cables. An Autolab PGSTAT 30 (EcoChemie) was used to control the potential when conducting the in-situ reflectivity measurements.

Scanning electron microscopes (XL30 ESEM Philips, and JSM 6500F Jeol) were used to study the surface morphology of the electrodes. A UV-visible spectrometer (USB2G5758 200 nm -850 nm, Oceanoptics Inc.) was used to measure the transmittance of the film. The reflectance measurements will be described in detail in section 2.4. The Raman spectra were recorded on a Renishaw Raman 2000 system using a 633 nm HeNe laser with 1 μm diameter spot size. The Raman spectra of the nanostructured IrOx films were obtained using 3 mW power and a single 10 s accumulation. X-ray diffraction (XRD) measurements were performed with a Siemens Diffraktometer D5000.

2.1.4 Reference electrodes

The reference electrodes used in all experiments Hg/Hg_2Cl_2, sat. KCL (SCE) and Hg/Hg_2SO_4, sat. K_2SO_4 (SMSE) were homemade. The SCE was stored in a saturated KCl solution and rinsed with purified water before use. Freshly prepared electrodes were left to stand for 24 hours in saturated KCl to reach equilibrium. The electrodes were tested regularly against a second SCE, which was always stored in a saturated KCl solution and solely used for testing.

The SMSE was prepared with the same procedure as SCE, except that Hg_2SO_4 replaced Hg_2Cl_2 and K_2SO_4 replaced KCl. All reference electrodes were rinsed with purified water before use.

2.1.5 Working electrodes

The 25 μm diameter electrode was produced in the laboratory. Initially, the glass body of the electrode was washed with water, followed by acetone and dried with a flowing stream of air (water pump). The microwire was handled with special tweezers. A piece of microwire of 3 cm was cut and inserted into the narrow end of the glass body. The end with the microwire was roughly sealed first. It was then sealed with a heating coil under vacuum. The glass was sealed allowing 5 to 10 mm of exposed microwire. An electrical connection was made by filling small pieces of indium into the glass electrode body and inserting a nickel wire. The heating coil was employed again to melt the indium pieces. The connecting wire was pushed into the molten metal until almost to the bottom. Then it was fastened at the top of the glass electrode body to prevent movement of the indium connection. The surface of the microelectrode was polished with silicon carbide paper using grades 320, 600 and finally 1200, and alumina aqueous slurry of grades 1.0 μm and 0.3 μm.

The glassy carbon electrode of 3 mm diameter was produced in the laboratory. The glassy carbon rod was obtained from Tokai Carbon. The glassy carbon electrode consisted of two parts: a head and a body connected by a stainless steel thread. The glassy carbon rod was sealed in a glass tube by the glass-blower, this made the head part. This structure made it possible to place the head with the film on the SEM stage.

Gold electrodes used as substrates were prepared by evaporating 10 nm of chromium, followed by 200 nm of gold onto 1 mm thick glass microscope slides. ITO electrodes were made by cutting commercial ITO slides (Vision Tek Systems Ltd).

2.2 Preparation of templates

The substrates (gold or ITO) were thoroughly cleaned before use by sonication in deionized water for 30 min followed by sonication in isopropanol for 90 min. They were then rinsed with deionized water and dried under a gentle stream of argon. Cysteamine was self-assembled onto the evaporated gold electrodes by immersing the freshly cleaned

gold substrate in a 10 mM ethanolic solution of cysteamine at room temperature for several days.

The deposition of the colloidal template layers was carried out in a thin layer cell (2 cm×1.5 cm) made up of the cysteamine coated gold electrode (or ITO electrodes) and a clean, uncoated, microscope cover glass held 1 mm apart by a spacer cut from Parafilm (Pechiney Plastic Packaging, Inc.). The parafilm was then slightly heated in order to hold the two plates together. The space between the two plates was filled with the aqueous 1 wt. % suspension of polystyrene latex spheres. The transparent glass plate allows the filling of the cell to be monitored and a very slight argon stream was used to remove any trapped air bubbles. The filled thin layer cell was held vertically in an incubator (Model LMS series 1) in order to control the rate of evaporation from the cell. After drying the template appears opalescent with colours from green to red, depending on the angle of observation, clearly visible when illuminated from above with white light. This is consistent with the presence of an array of spheres with diameter similar to visible wavelength and behaving as a grating. The templates are robust and adhere well to the gold substrates (or ITO).

2.3 Electrochemical Deposition of iridium oxide

Two recipes were tested for the electrochemical deposition of IrOx films. The successful one was selected and applied in the remaining parts of the research. The electrochemically induced deposition of iridium oxide was carried out by using the substrate as a working electrode and performing cyclic voltammetry within the potential range -0.8 to +0.7 V vs. SCE at 100 m V s^{-1}.

In some experiments, iridium oxide films were grown with a series of steps in thickness to form so called “graded samples”. This was achieved by gradually lifting the substrate out of the deposition solution using a microstage to carefully control the immersion depth. The typical length of the steps is around 0.5 mm according to the gold substrates size. This microstage was made by mounting a homemade electrode holder on a manual

positioning (Newport M-460A series SM-13). The micrometer of the manual positioning can be sensitive to 0.5 mm. By fine control of the micrometer, the immersion depth of the deposition substrate can be controlled. Figure 2-1 below is the illustration of the controlled deposition procedure and the process of completing a thickness graded sample.

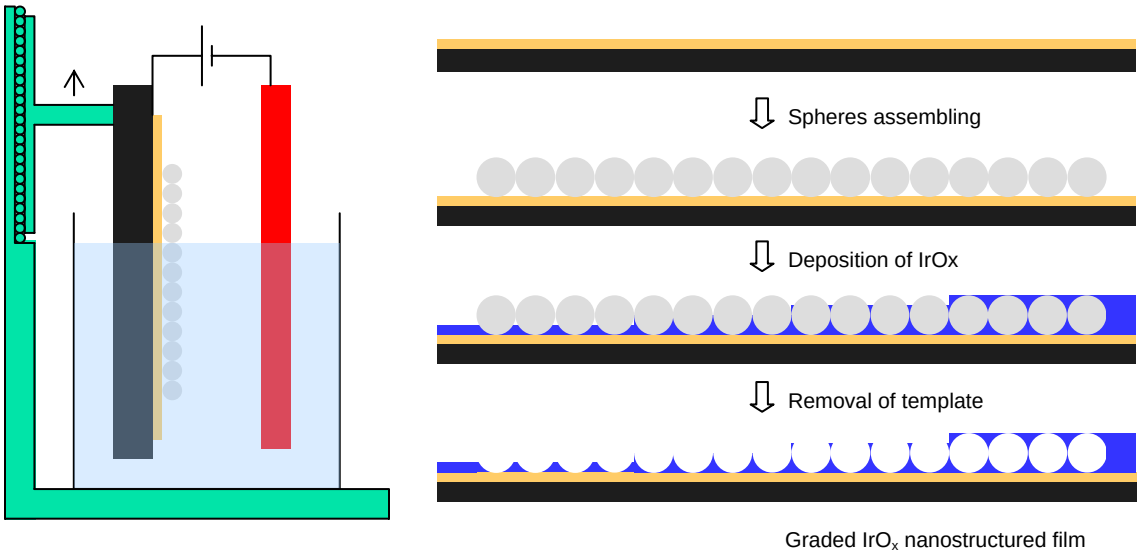

Figure 2-1 : Left: the fine control of the immersion depth of the electrode in the deposition solution; Right: procedure for preparing a thickness graded sample. These steps, from top to bottom, include: pre-treating the substrate, spheres self assembling, depositing IrOx film, and removal of template.

When the deposition was complete the samples were soaked in DMF to dissolve the polystyrene template. This step often took less than 30 mins with sonication. A defined area was created by nail polish when depositing both non structured and structured IrOx films.

A few experiments on different methods to remove the spheres of deposited samples have been tested in this project.

2.4 In situ reflectance measurements

The electrochromic studies of iridium oxide films were carried out in situ. The reflectance data of iridium oxide films were recorded for both coloured and bleached states on nanostructured IrOx films (chap. 5) and on thin iridium oxide films deposited on thickness-graded macroporous gold films (chap. 6). The electrochemical cell was mounted inside an optical measurement cell. The reflectance data of the iridium oxide films were measured under potential control through a transparent $(NH_4)_2SO_4$ electrolyte (pH 4). Figure 2-2 presents the design of the optical measurement instruments. Spectra were collected using both visible and infrared Spectrometers (Ocean Optics USB2000 and NIR512). A white laser source has been employed to illuminate the samples.

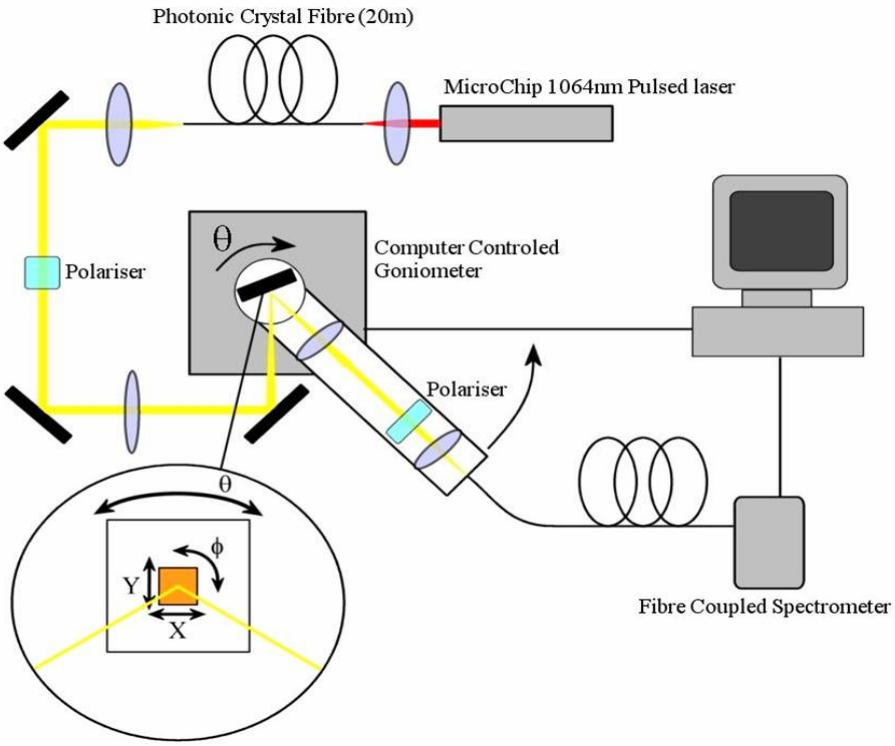

Figure 2-2: Schematic of the experimental design of the optical measurement used to measure the sample reflectance [203].

The reflectance spectrum of coloured iridium oxide films on structured gold was obtained when holding the potential at + 0.5 V after one scan (from -0.3 to +0.5 V vs. SCE) in the electrolyte at a scan rate of 20 mV s^{-1}; while the reflectance spectrum of bleached iridium oxide films on structured gold was obtained when holding the potential at - 0.3 V after one scan (from +0.5 to -0.3 V vs. SCE) in the same electrolyte at scan rate of 20 mV s^{-1}.

The same arrangement was also applied in the reflectance experiments of pure structured IrOx film deposited on a smooth gold substrate. The electrochemical cell was mounted inside an optical measurement cell. The reflectance data of the iridium oxide films were measured under potential control through a transparent $(NH_4)_2SO_4$ electrolyte (pH 4).

Chapter two described the experiments details of the project. The following chapter will consider the electrochemical deposition of non-structured IrOx films.

3 Electrochemical deposition of non-structured IrOx films

3.1 Two deposition recipes

Two alkaline electrochemical deposition methods for IrOx films have been selected after reviewing the literature. Experiments have been carried out according to the two recipes and are reported in the following paragraphs. Each step in the experiments was carried out by repeating the steps described in the recipes.

Baur's recipe [165]:

The first step in the preparation of the deposition solution is the formation of the diaquotetrachloroiridate (III) ion, $Ir(OH_2)_2Cl_4^-$ from $IrCl_6^{2-}$. In the experiment, ethanol was added as a reducing agent in a 23 mM solution of $IrCl_6^{2-}$ in 0.1 M HCl. The mixture was heated to the boiling point (around 70 ^oC) until the reduction was completed.

To ensure complete reduction, ethanol was added at regular intervals to replace that lost by evaporation. In the reduction process, it can be observed that the solution colour changes from a deep reddish-black to clear light brown. According to Baur, temperature is a critical parameter in the process. High temperature led to a vigorous reaction and to the formation of a black precipitate. The solution with this precipitate could not be used for deposition.

A UV spectrometer was employed to monitor the colour change in the reaction and assess the composition. In practice, clear spectra were not obtained due to the presence of solid particles suspended in the solution. According to spectra generated by Baur and co-workers [165], the colour change should be accompanied by a complete loss of the strong absorption bands for the $IrCl_6^{2-}$.

The second step in the preparation of the deposition solution is the formation of air sensitive iridium (III) oxide $Ir_2O_3 \cdot x\ H_2O$ from $Ir(OH_2)_2Cl_4^-$ in presence of NaOH:

After several failed experiments in the lab, it was concluded that oxygen must be removed before addition of the base. After a thorough argon sparge, the acidic solution of $Ir(OH_2)_2Cl_4^-$(pH ~ 2) was neutralized by the addition of 6 M NaOH. Additional base was added to make the pH of the solution to about 12.50. As the solution became basic, its color changed from light brown to light green as described in [165].

The oxidation of the iridium (III) oxide solution prepared can be initiated electrochemically and a precipitate can be formed on the electrode. In practice, deposition did not occur. Cyclic voltammograms recorded in this depositing solution, Figure 3-1 below, shows no peak for the growth of a film since peak current would be expected to increase when the film is growing.

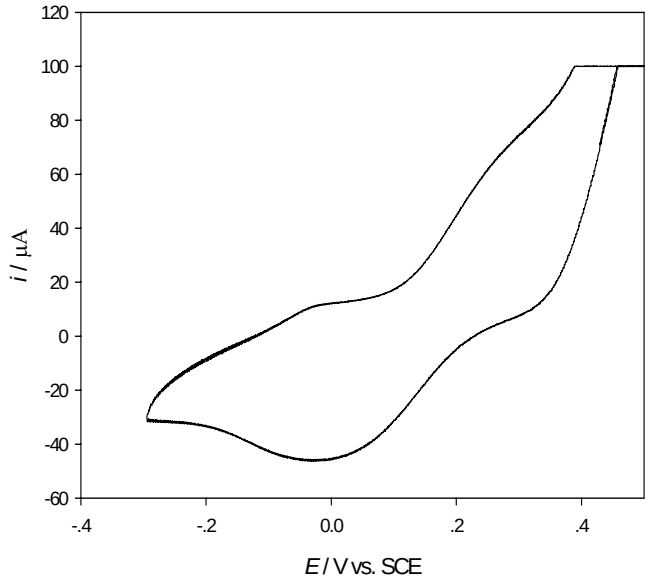

Figure 3-1: Cyclic voltammograms recorded with a glassy carbon electrode (3 mm Ø) at a scan rate of 100 mV s^{-1} in the depositing solution (degassed) made with Baur's recipe after repeated scans (Potential range between -0.3 V to 0.4 V).

The cyclic voltammogram was obtained by scanning up to 1.0 V. From circa 0.4 V the current increases continuously and saturates the recording system. Only the voltammogram between –0.3 V and 0.4 V is shown. After the cycling, the deposition

solution turned deep purple, and a black precipitate formed in a few minutes. It is likely that Ir(IV) oxide was formed in the solution by oxygen and that no deposition occurred on the electrode.

Iridium (III) oxide is extremely sensitive to oxygen. It is likely that oxygen leaked into the deposition cell when setting up the experiment and led to unsuccessful experiments. Despite additional information received from Baur's group, the conditions of Baur's recipe are difficult to control. Also, it is hard to avoid oxygen leaking into the electrochemical cell when depositing nanostructured IrOx films. Therefore, this method was not selected for this project.

Yamanaka's recipe [180]:

In Yamanaka's recipe, the electrodepositing solutions are made from iridium tetrachloride, hydrogen peroxide, oxalic acid and potassium carbonate. Oxalic acid is added to form an iridium complex in the depositing solution. The addition of hydrogen peroxide to the solutions makes it possible to deposit an oxide film at lower current densities, but its mechanism is not clear. From the literature [180], the deposition efficiency increases as the pH value of the solution increases, and reaches a constant value around a pH of 10.0. Based on this, the solution was prepared with a pH value of 10.5.

The anodic deposition of iridium oxide is thought to result from the precipitation of an Ir(IV) oxide formed by electrochemically induced oxidation of an Ir(IV) complex. The mechanism in which IrO_2 is formed by anodic oxidation of ligands in an Ir complex is reported to be [180]

$$[Ir\,(C_2O_4)\,(OH)_4]^{2-} \rightarrow IrO_2 + 2CO_2 + 2H_2O + 2e^- \qquad \textit{Equation 3-1}$$

The solution slowly decomposes and form $[Ir(C_2O_4)_3]^{3-}$. The oxalate ligand is oxidised to form CO_2, and IrO_2 which is insoluble and precipitates on the electrode. CO_2 evolution and formation of IrO_2 are caused by the oxidation of $[Ir(C_2O_4)_3]^{3-}$ by oxygen.

The depositing solution was prepared as follows. Iridium tetrachloride was dissolved in 50 ml of water. The solution was stirred for 30 min. A 0.5 ml aliquot of aqueous 30% hydrogen peroxide solution was added, and the resulting solution was stirred for 10 min. 250 mg of oxalic acid dehydrate was added, and the solution was stirred again for 10 min. The pH of the solution was adjusted slowly to 10.5 by addition of potassium carbonate [180, 181]. The resulting solution was yellowish brown. The solution was covered and left at room temperature for 3-4 days for stabilisation. The colour finally appeared deep purple.

3.2 Fabrication and characterisation of smooth IrOx thin films

3.2.1 Electrochemical deposition of IrOx film with cyclic voltammetry

Non-structured thin IrOx films were deposited on a platinum microelectrode and a glassy carbon (3 mm Ø) electrode in order to study the mechanism of electrochemically induced deposition and the quality of the iridium oxide films. Platinum microelectrodes were used because the initial objective was to fabricate an iridium oxide microelectrode for pH detection. The growth of the oxide film can be followed electrochemically because the oxide undergoes a reversible redox reaction in the solid state [165] when deposition on microelectrode. Figure 3-2 shows the growth of an iridium oxide film on the surface of a platinum microelectrode with repeated cycling of the potential between – 0.7 and + 0.7 V.

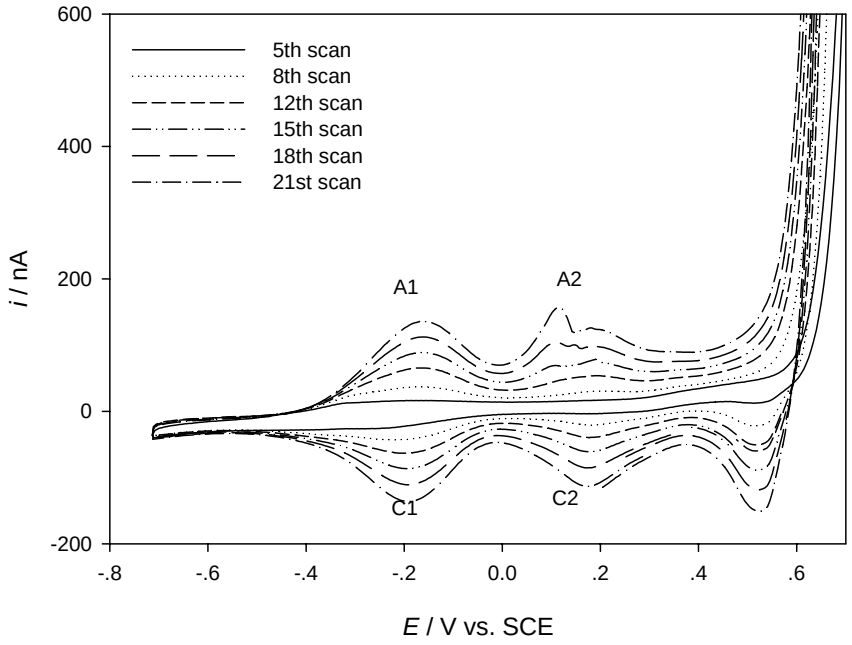

Figure 3-2: Voltammograms for the growth of iridium oxide on a Pt microelectrode (25 μm diameter) from the electrochemical deposition solution made using Yamanaka's recipe (pH = 10.5). Scan rate: 100 mV s^{-1}. Anodic peaks A1 and A2 and cathodic peaks C1 and C2 indicate the film is switching between the solid redox states of Ir oxide as the potential is swept.

Cathodic peaks at -0.2 V (C1) and +0.2 V (C2) and anodic peaks at -0.2 V (A1) and +0.2 V (A2) respectively reflect the Ir(III) / Ir(IV) and Ir(IV) / Ir(V) redox reactions within the IrOx oxide film. According to the literature [15], the degree of oxidation of iridium is as follows: E < -0.3 V for Ir(III); 0 V < E < 0.2 V for Ir(IV); and E > 0.3 V for Ir(V) [15]. The cyclic voltammograms grow when increasing the cycle numbers. Both the anodic and the cathodic peaks sit on top of each other symmetrically, thus suggesting the redox processes are reversible. The symmetric peaks indicate the surface redox processes are consistent with the voltammograms reported in the literature [180]. The cathodic peak at around 0.55 V is not explained at this stage.

IrOx films were fabricated on a glassy carbon electrode (3 mm diameter); the cyclic voltammogram is presented in Figure 3-3 below.

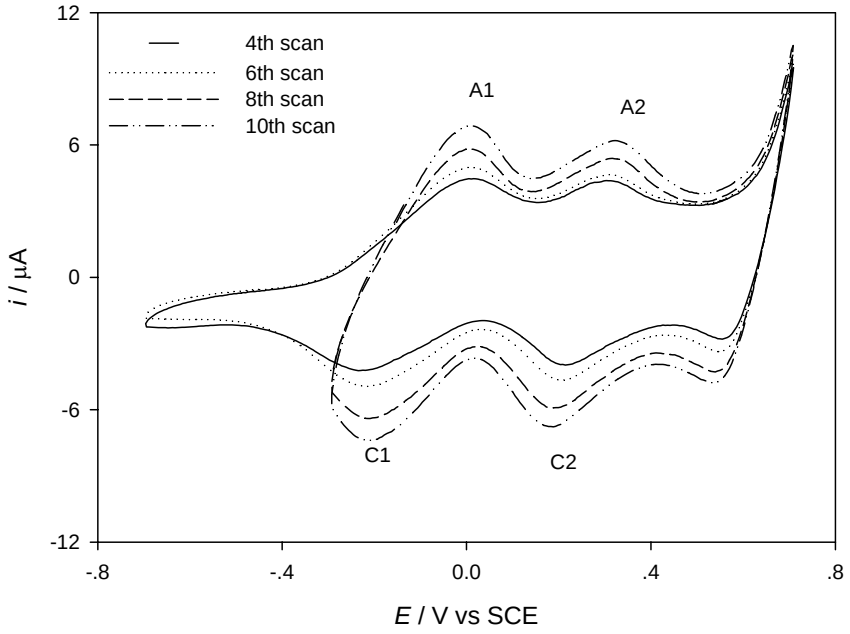

Figure 3-3: Voltammograms for the growth of iridium oxide on a glassy carbon electrode (3 mm diameter) from the electrochemical deposition solution (pH = 10.5). Scan rate: 100 mV s^{-1}. Anodic peaks A1 and A2 and cathodic peaks C1 and C2 indicate the solid redox states of Ir oxide.

The CVs on glassy carbon electrodes show some similarity to those on Pt microelectrodes; therefore it suggests the mechanism of deposition is the same in both cases, however the redox processes are less reversible on the glassy carbon electrode compared to those on microelectrodes. Also the peak separation is greater on the glassy carbon electrode. In Figure 3-3, the potential range for deposition on the glassy carbon electrode was changed after a few cycles to test the effect of the negative potential. The results show no significant effects.

3.2.2 Characterisation by cyclic voltammetry in acid and alkaline solutions

Once deposited, the iridium oxide films were characterized by performing cyclic voltammetry in base and in acids. Figures 3-4 and 3-5 show the voltammograms of the IrOx deposited on a glassy carbon electrode in H_2SO_4 (0.5 M) and Na_2CO_3 (0.1 M) solutions respectively. The redox process appears reversible in acid but not in base. Although not shown here the peak currents were found to be linear with the potential sweep rate.

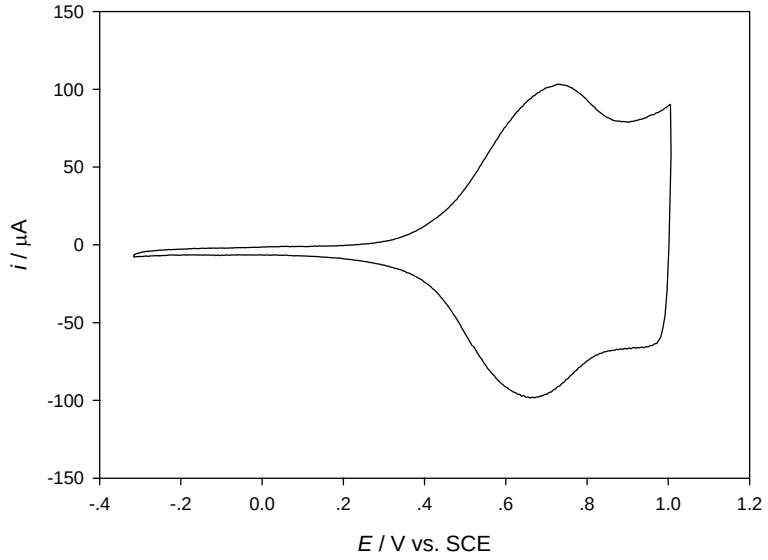

Figure 3-4: Cyclic voltammogram of an iridium oxide film on a glassy carbon electrode in H_2SO_4 (0.5 M) solution at scan rate 100 mV s^{-1}, after several scans. Potential range: -0.3 to +1.0 V.

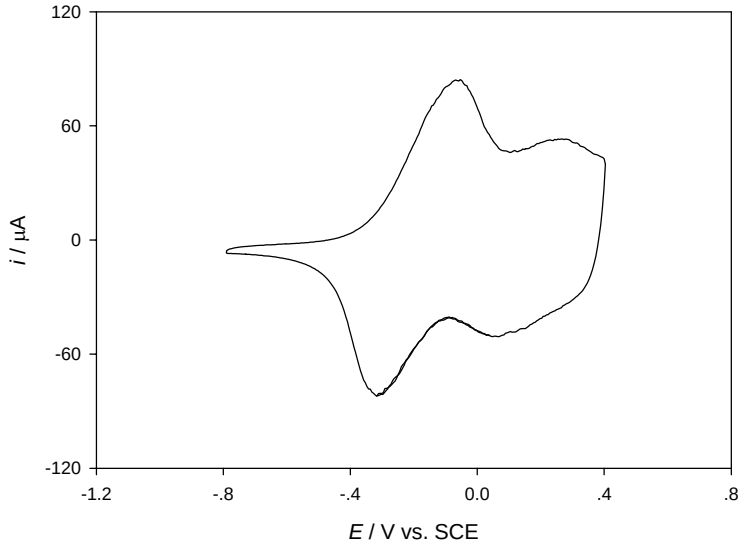

Figure 3-5: Cyclic voltammogram of an iridium oxide film on a glassy carbon electrode in Na_2CO_3 (0.1 M) solution at scan rate 100 mV s^{-1}, after several scans. Potential range: - 0.8 V to 0.4 V.

These two voltammograms indicate the same solid state redox processes as in the deposition solutions but without growth. In acid solution, the region of $E < 0.7$ V shows oxidation state iridium (III); region of $E > 0.7$ V shows the oxidation state iridium (IV). Because of the pH, the redox reaction Ir(IV) / Ir(V) occurs after oxygen evolution. In base solution, the degree of oxidation of iridium is as follows: $E <$ -0.4 V for Ir(III); -0.1 V $< E <$ 0 V for Ir(IV); and $E > 0.2$ V for Ir(V). The regions of the oxidation states of iridium in base are not as clear as in acid because the film is less reversible in base. However, the films are not very stable in acid. Thus, the CVs in base will be used to routinely characterise the films.

3.2.3 SEM Characterisation

IrOx films made by electrochemical deposition from Yamanaka's recipe were characterised by SEM. The deposited films are black blue in colour and so soft that they are easily scratched. Figure 3-6 presents a film made on a glassy carbon electrode. Half of the film on the electrode surface was scratched by a spatula. It helps to see the electrode surface and the film clearly.

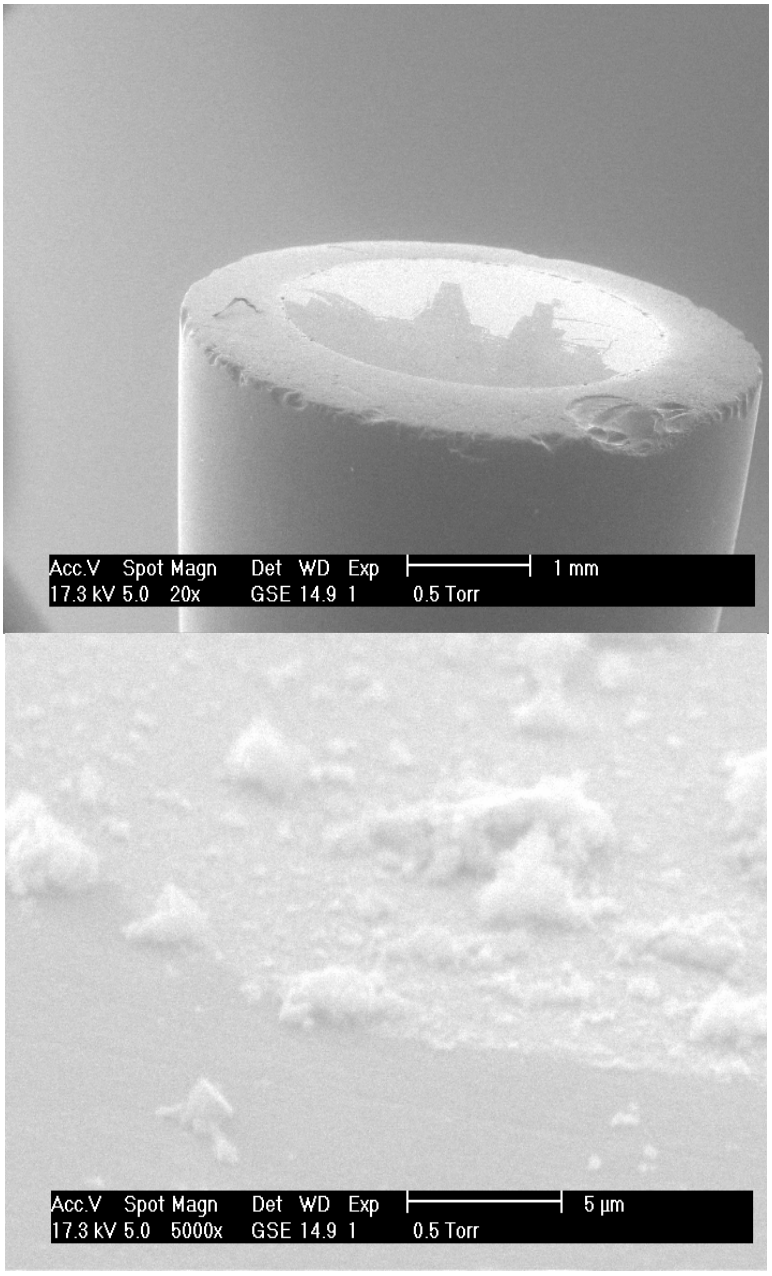

Figure 3-6: SEM pictures of electrochemically deposited IrOx film on a glassy carbon electrode: top, the scratched electrode surface, bottom, zoom on the surface. The image was taken under wet mode.

Another SEM micrograph of an IrOx film was recorded under high vacuum mode as shown in Figure 3-7. The surface of the oxide is rough with some larger crystalline deposits.

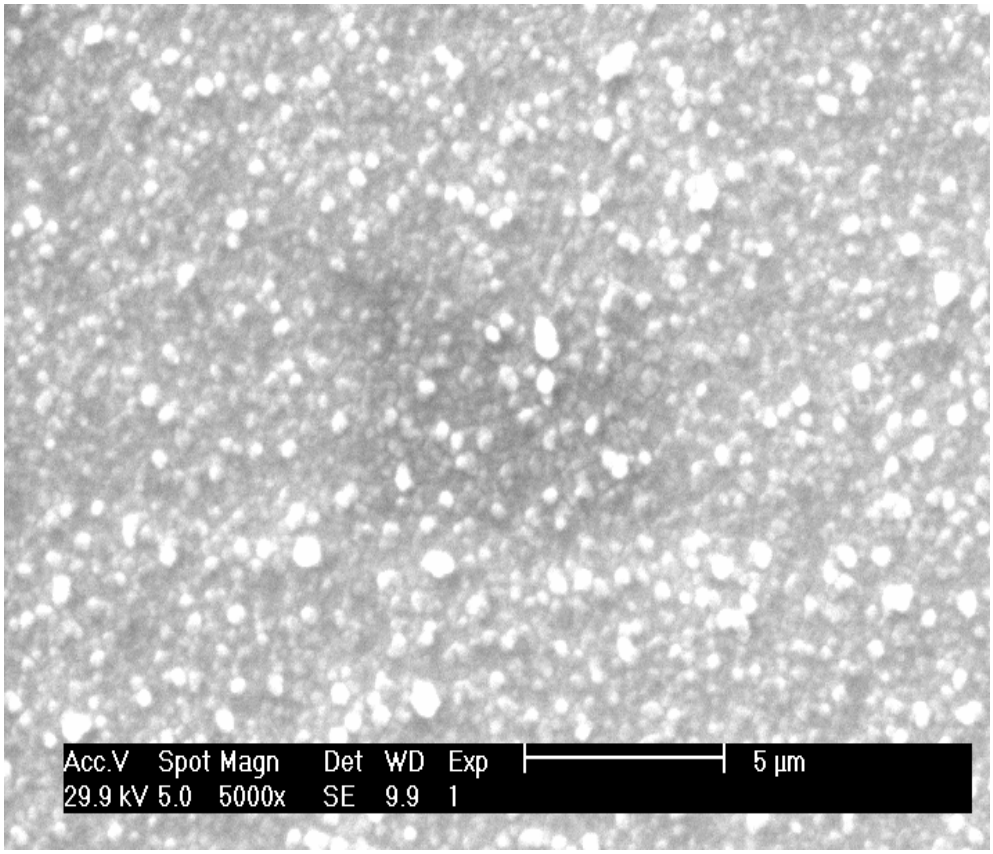

Figure 3-7: Electron micrograph of an IrO_x film deposited on a glassy carbon electrode. The white spots indicate large crystalline deposits.

SEM characterisation shows that the electrochemically deposited IrOx film has a rough, granular texture.

3.2.4 EDX characterisation

To identify the composition of the film, Energy Dispersive X-ray (EDX) analysis was carried out. Table 3-1 shows EDX information of the iridium oxide films deposited on a Pt microelectrode.

Table 3-1: Composition of elements in the iridium oxide film obtained by EDX analysis: Column 2 shows weight percentages and Column 3 shows atomic percentages.

Element	***Wt%***	***At %***
O	21	65.14
K	4.05	8.74
Cl	5.93	8.3
Ir	69.02	17.82
Total	100	100

The film was deposited from a solution rich in K and Cl elements, therefore, some of these elements stayed on the electrode surface when the film was deposited. From the information provided, the main composition of the film is iridium (wt % 69.02), however, the percentages for Ir and O do not suggest a 1:2 atomic ratio as expected for IrO_2; this may be due to the analysis being carried out in the wet mode of the SEM where the chamber is filled with a low vapour pressure of water (wet mode) thus giving a result richer in O.

3.2.5 X-ray diffraction characterisation

XRD was also employed to analyse the crystallinity of the non-structured electrochemically deposited IrOx films. Yamanaka claims that the electrochemically deposited IrOx film contains a large amount of water and has an amorphous structure. An IrOx film was produced by cycling in the deposition solution for up to 400 cycles. According to the thickness dependence calculation in Chapter 5, the film was estimated to have a thickness of around 2 µm.

The sample was fixed in an alumina sample holder for XRD measurements. Parameters for the measurements were: angle 10-80 ^{o}, increment 0.02 ^{o} and scan speed 12. An XRD spectrum is shown in Figure 3-8; all the red lines correspond to the fingerprint of gold. There are no peaks indicating the presence of crystalline IrOx in the film. Either this suggests that the film is amorphous or that the film is too thin for the diffraction of IrOx to overcome that of the gold substrate.

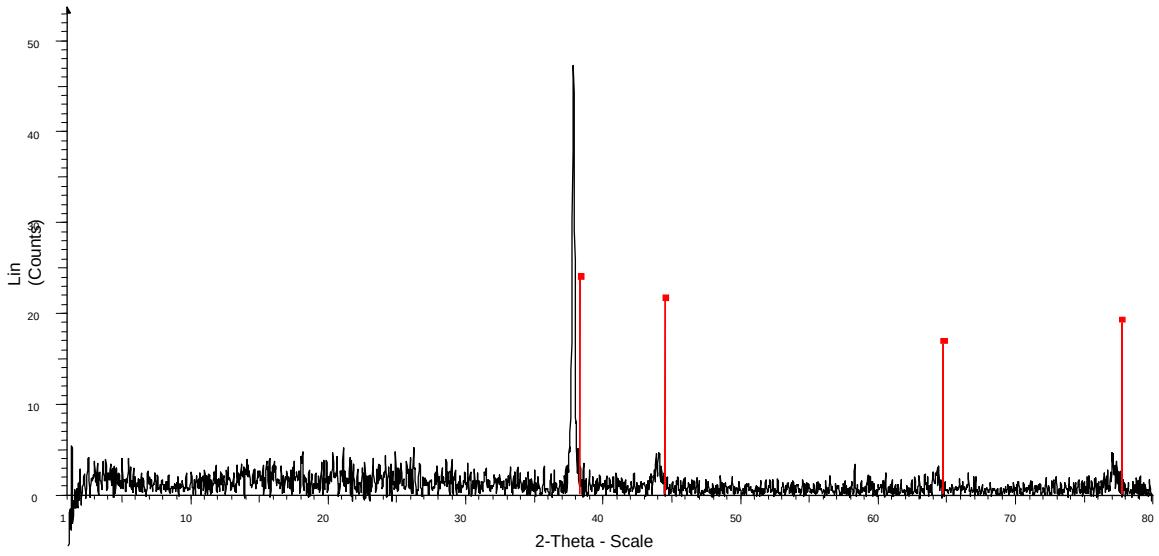

Figure 3-8: An XRD spectrum of an iridium oxide film deposited on a gold plate. The red peaks correspond to the Au fingerprints found by the software. No peaks are found that correspond to iridium oxide.

3.2.6 Raman spectroscopy characterisation

Raman spectroscopy has been employed to investigate the crystallinity of IrOx films, e.g. Raman scattering was used as a technique for characterisation of sputtered IrO_2 thin films [171, 172, 204, 205]. In this work, Raman spectroscopy is employed to investigate the structure of electrochemically deposited films.

Yamanaka found that the electrochemically deposited IrOx film has an amorphous structure as deposited but that the film becomes crystalline after annealing [181]. A flat IrOx thin film was produced on a gold coated glass electrode by cyclic voltammetry. Raman spectra of the deposited IrOx film were recorded using a 633 nm HeNe laser with 1 μm diameter spot size. A typical spectrum is shown in Figure 3-9.

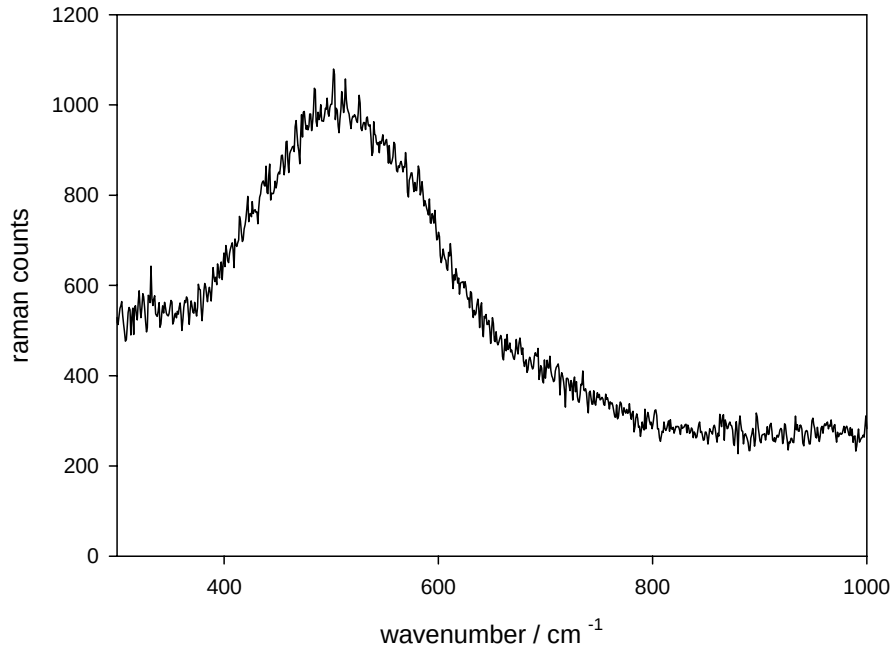

Figure 3-9: Raman spectrum of a thin IrOx film (~20 scans) electrochemically deposited on a gold slide. The Raman spectra were recorded on a Renishaw Raman 2000 system using a 633 nm HeNe laser with 1 μm diameter spot size.

A Raman spectrum of the annealed IrOx film was recorded and is shown in Figure 3-10. The sample used for annealing was made by cyclic voltammetry on a gold coated glass slide under the same condition. The annealing process took place at 460 ºC in an oxygen atmosphere for 1 hour. The temperature in the furnace was controlled carefully by increasing by 5 ºC every minute from room temperature to 460 ºC.

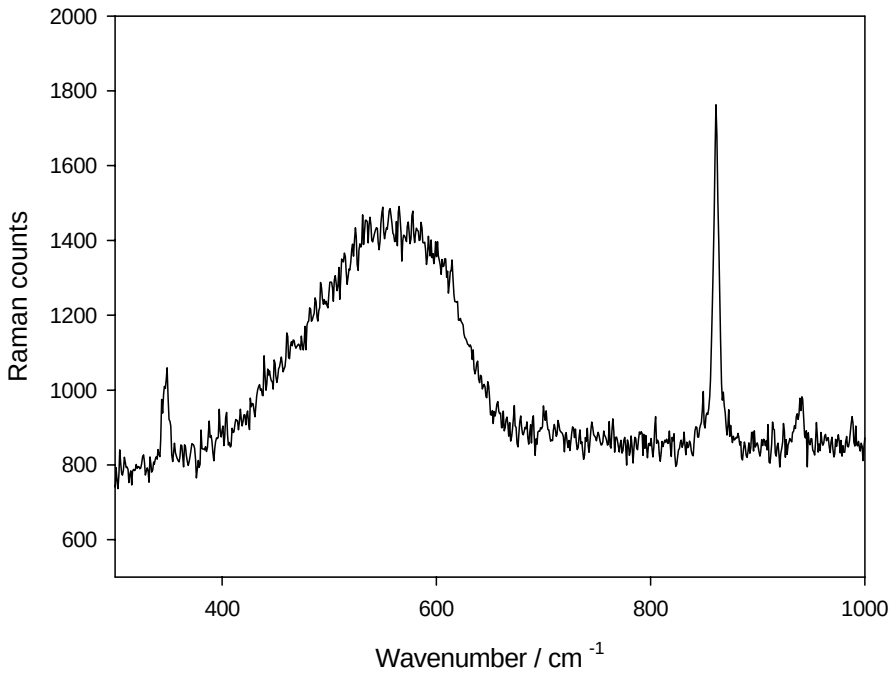

Figure 3-10: Raman spectrum of an annealed IrOx thin film. The annealing was carried out at 460 ºC in an oxygen atmosphere for 1 hour. The Raman spectrum was recorded on a Renishaw Raman 2000 system using a 633 nm HeNe laser with 1 µm diameter spot size.

Comparing to Figure 3-10, two distinct sharp peaks appear (at 300 and 900 cm^{-1} respectively) in the Raman spectrum for annealed IrOx films in Figure 3-11. A narrowing of the peak at 500 cm^{-1} can also be observed in Figure 3-11. The changes observed in the spectrum of the annealed film can be attributed to crystallization and structural ordering of the film during the annealing process.

Raman scattering characterisation shows that the electrochemically deposited IrOx films were amorphous as grown but became crystalline through heat treatment at 460 ºC for an hour.

3.3 Electrochemical deposition of non-structured IrOx with different electrochemical techniques

A thorough study of the different deposition techniques with the same recipe (the Yamanaka's alkaline anodic electrodeposition) was conducted in order to optimise the quality of the deposited film and find out the most suitable method. It can be observed that oxygen evolution occurs at ~ +0.63 V vs. SCE in the pH 10.5 deposition solution. The open circuit potential of the electrochemical cell containing the electrodeposition solution is ~ -0.327 V vs. SCE measured with a potentiostat galvanostat (Autolab). All the films were deposited on a carefully cleaned gold coated glass slide (working electrode) with a defined deposition area (0.25 cm^2).

A systematic study of the deposition of IrOx films with cyclic voltammetry is summarised in the table below. Four deposition experiments were carried out with the same recipe on a gold coated glass with scan rate at 100 mV s^{-1}.

Table 3-2: Experimental conditions for cyclic voltammetry when electrodepositing IrOx films from the alkaline solution, E_1 is the start potential, E_2 is the vertex potential, and the last column shows the possibility of film deposition. Presence of films observed visually. IrOx film appears to be dark blue. 100 cycles were used before measuring the charges with Autolab.

E_1 / V vs. SCE	E_2 / V vs. SCE (100 cycle 100 mV/s)	Deposition of film
-0.8	+0.7	yes
-0.8	+0.6	yes
-0.8	+0.5	No
-0.8	+0.4	No

In Table 3-2, E_1 is the start potential of the potential sweep while E_2 is the vertex potential. From the experiments, we can conclude, it is not possible to produce a film when $E_2 \leq 0.5$ V vs. SCE. However, the start potential is not important as indicated in later experiments. Table 3-3 below shows a series of results for the deposition of IrOx films with potential stepping methods.

Table 3-3: The experimental conditions for the potential step deposition of IrOx films. E_1 is the start potential and E_2 is the step potential. Presence of films observed visually. IrOx film appears to be dark blue.

E_1 / V vs. SCE	E_2 / V vs. SCE	Deposition of film
-0.7	+0.7	Yes
-0.7	+0.6	Yes
-0.7	+0.55	Yes
-0.7	+0.5	No

Table 3-3 indicates that the film cannot be produced when $E_2 \leq 0.5$ V as observed when using cyclic voltammetry. The results from both tables suggest that the oxidation of the oxalate ligand in the deposition solution does not occur to sufficient extent to form a film when the upper potential limit is below 0.5 V vs. SCE. Particularly, in Table 3-3 it is clear that the film can only be produced when $E_2 \geq 0.55$ V vs. SCE.

A galvanostatic method was also employed to obtain an IrOx film from the same solution. The experiment was conducting under a constant current density of 1.6 A m^{-2} for 1000 s as suggested by Yamanaka and a bluish film was obtained. The charges applied during the film growth with different methods are presented below in Table 3-4. It is important to notice that all the films were made on a substrate with the same area. The higher the charge, the thicker the film will be as we would expected.

After the deposition, all the films deposited were characterised in a Na_2CO_3 solution with pH 10.9 (0.1 M) by cyclic voltammetry; CVs were recorded with a potential range between -0.7 V and 0.5 V vs. SCE at 50 mV s^{-1}. Only the 2nd cycles were recorded. These CVs were analysed to estimate the charge under the anodic and cathodic regions.

The results prove that it is possible to deposit IrOx films using different electrochemical techniques with Yamanaka's deposition solution. It also gives us a minimum positive potential of +0.55 V in order to form the film. Figure 3-11 (a) and (b) show the characterisation voltammograms of IrOx films produced by cycling with 100 cycles at 100 mV s^{-1} to 0.6 V and 0.7 V, respectively.

Table 3-4: Autolab recorded charges of the IrOx film produced by different methods. The charges were measured by the Autolab programme with the characterisation CVs. Charges were measured between E1 and E2. E1 is the starting potential, E2 is the vertex or stepping potential.

Techniques	**Conditions E_2 (time)**	***Anodic charge*/m C**	***Cathodic charge*/m C**
Potential stepping	0.7 V (1500 s)	16.0 ± 0.8	16.0 ± 0.8
	0.6 V (1500 s)	7.6 ± 0.4	7.7 ± 0.4
	0.55 V (1500 s)	4.1 ± 0.2	4.2 ± 0.2
	0.7 V (1000 s)	8.7 ± 0.5	5.7 ± 0.3
	0.6 V (1000 s)	4.1 ± 0.2	4.0 ± 0.2
	0.55 V (1000 s)	1.7 ± 0.1	1.7 ± 0.1
	0.7 V (500 s)	1.9 ± 0.1	1.9 ± 0.1
	0.6 V (500 s)	3.4 ± 0.2	2.0 ± 0.1
	0.55 V (500 s)	0.3 ± 0.1	0.7 ± 0.1
Cyclic voltammetry	0.7 V (100 cycles)	7.3 ± 0.3	7.6 ± 0.4
	0.6 V (100 cycles)	2.2 ± 0.1	2.5 ± 0.2
Galvanostatic	1.6 A/ m^2 (1000 s)	4.0 ± 0.2	4.0 ± 0.2

The cyclic voltammograms of films made by cycling to 0.6 V and 0.7 V show a similar shape with major peaks at the same potentials. The CVs show a similar solid state redox process thus suggesting that the IrOx films have the same composition. The current scales between two CVs are slightly different; this is presumably due to the film thickness difference. Sample used in (b) is a much thicker film because the film was made by cycling to 0.7 V which gave more charge during the deposition, thus forming a thicker film as the deposition area is the same for both films.

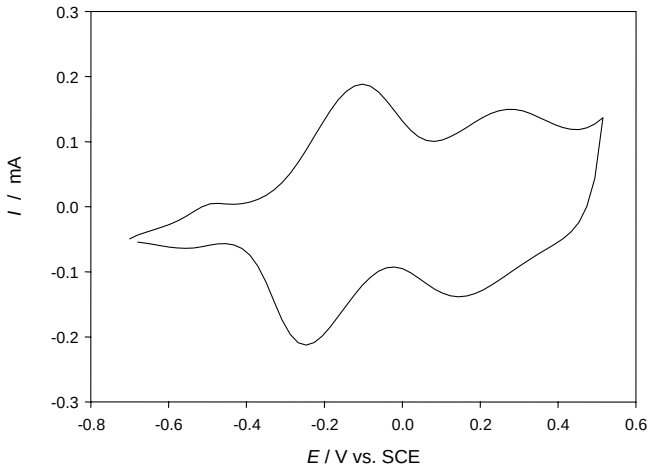

(a)

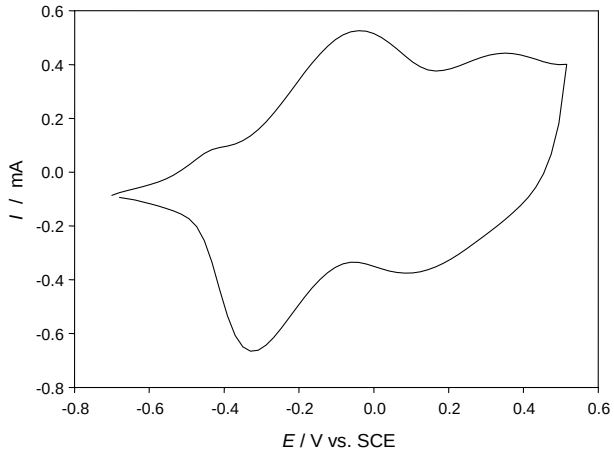

(b)

Figure 3-11: Characterisation voltammograms showing the 2nd scan in a 0.1 M Na_2CO_3 pH 10.5 solution of the samples made by cyclic voltammetry with upper limit potentials: (a) 0.6 V and (b) 0.7 V (both 100 cycles, at scan rate 100 mV s^{-1}). All the working electrodes used are gold coated glass slides and reference electrode is SCE.

Figure 3-12 (a), (b), and (c) present the 2nd cycles in the alkaline solution of the samples produced by stepping the potential from -0.7 V to 0.55 V, 0.6 V and 0.7 V for 1000 s, respectively.

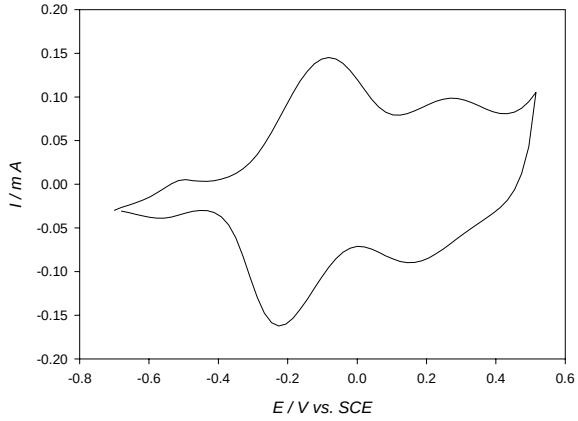

(a)

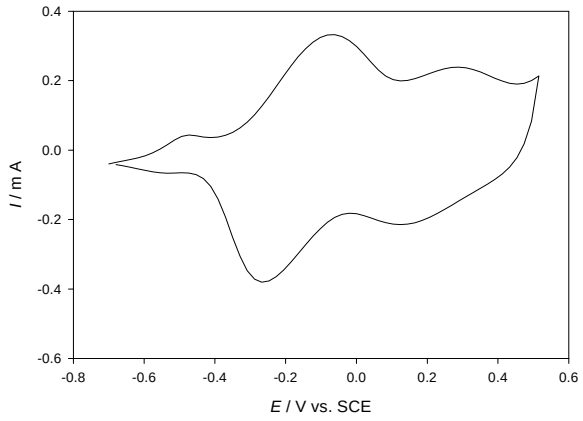

(b)

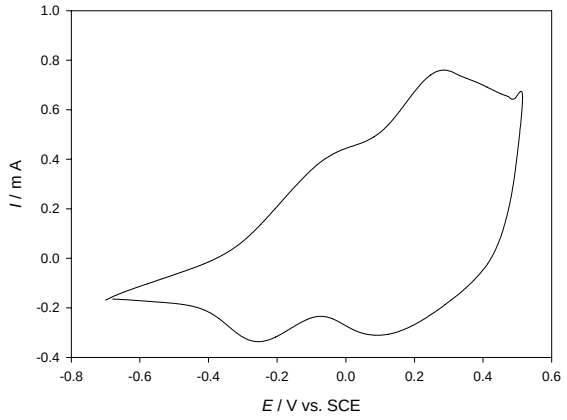

(c)

Figure 3-12: Characterisation voltammograms showing the 2nd scans in a 0.1 M Na_2CO_3 pH 10.5 solution of the samples on gold electrode produced by stepping from -0.7 V to (a) 0.55 V, (b) 0.6 V and (c) 0.7 V for 1000 s, respectively. Scan rate 100 mV s^{-1} vs. SCE. Gold substrate was used for deposition.

The current transients for each condition were recorded during the deposition, but they showed no distinguishing features and are not presented here. Cyclic voltammograms of

the IrOx films made by stepping to 0.55 V and 0.6 V have a similar shape and have peaks at the same position. The results suggest that the films have the same composition. The CV from the film made by stepping to 0.7 has a higher peak current at 0.3 V vs. SCE. However, it was not possible to determine the film composition during the course of this research.

Figure 3-13 is the cyclic voltammogram of the IrOx film produced with galvanostastic deposition. The 2nd set of peaks in this CV differs from the peaks in the CV of IrOx film made from other technique. So it is either more of the film is converted to Ir(V) thus implying that not all IrOx is involved in the redox process, or the process is faster, hence leading to higher peaks.

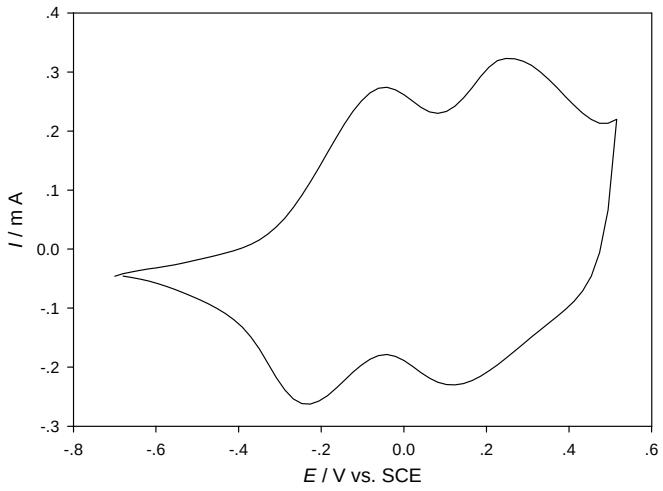

Figure 3-13: Characerisation voltammogram showing the 2nd scan in a 0.1 M Na_2CO_3 pH 10.5 solution of the sample produced by galvanostatic deposition the current at the rate of 1.6 A m^{-2}, 1000s.Gold substrate was used for deposition.

IrOx films can be produced with all kinds of electrochemical deposition methods with Yamanaka's recipe under the right conditions. The films produced by various techniques have a similar structure by visual observation.

3.4 Summary and conclusion of Chapter Three

Two recipes of electrochemical deposition of IrOx films have been applied in this project. Baur's recipe was compared to Yamanaka's recipe, the former was found to be unsuccessful and difficult to implement. The latter was found to be an easy and perfectly controlled procedure.

With Yamanaka's recipe, IrOx films can be produced with various electrochemical deposition methods, including: potential sweep methods (cyclic voltammetry), potential step methods and controlled current methods (galvanostatic deposition). Among all the techniques, cyclic voltammetry was found to be the easiest and the one that gave a greater degree of control. During deposition, the CV clearly presents the growing process as well as the surface redox process; therefore the deposition CV can be used for characterisation of the deposited IrOx film where other techniques do not offer this advantage.

IrOx films produced by cyclic voltammetry with Yamanaka's recipe were characterised with a range of techniques. The electrochemically deposited IrOx film was first studied by cyclic voltammetry in both acid and alkaline solutions to observe the solid state redox processes. The CVs show the change in oxidation states upon cycling. The charges under the peaks can be understood as reflecting the relative proportion of the different oxidation states. However, the chemistry of these films is so complicated that we can not really get an exact figure from this. EDX was also employed to investigate the film composition. However, this was not successful and nothing could be concluded about the composition of the films.

SEM was applied to examine the surface roughness of electrochemically deposited IrOx film. IrOx films were successfully deposited on various substrates: gold, platinum, glassy carbon, and ITO. Both films deposited on platinum and glassy carbon were investigated by SEM.

The crystallinity of the electrochemically deposited IrOx thin film was studied by both XRD and Raman spectroscopy. The XRD pattern of the IrOx film showed no sharp peak

for single IrOx crystals, which indicates either that the film was too thin or that it was amorphous. However Raman spectra clearly indicated that the films were amorphous but could be turned crystalline by annealing at 460 ºC under oxygen.

This chapter studied the deposition of the IrOx film without template. The following chapter will introduce the templated deposition of the IrOx film based on the same chemical recipe discussed in this chapter.

4 Electrochemical deposition of nanostructured IrOx films

4.1 Templated deposition of nanostructured IrOx film

4.1.1 Fabrication and characterisation of nanostructured IrOx films

A wide range of methods have been proposed to produce colloidal templates which are free from defects over macroscopic length scales [206]. Gravity sedimentation from a dispersion of the colloid is an effective approach. However, it is difficult to control the template thickness. Alternatively, the capillary forces which develop at a meniscus between a substrate and a colloidal solution have been employed in this research. This meniscus is slowly swept across a vertically placed substrate by solvent evaporation; thin planar opaline films can be deposited. In the present work, cysteamine was used to modify the gold surfaces.

There are two distinguished effects from modifying the surface with cysteamine [207]. First, it increases the efficiency of assembly of the polystyrene spheres on the substrate by increasing the substrate–particle interactions. The substrate surface is positively charged by the chemical modification with the cysteamine and the spheres have a negative surface charge as a result of the sulphate groups used to stabilise the polystyrene suspension from manufacture. Second, it increases the wettability of the gold substrate since the contact angle for water can be decreased by treating with cysteamine. This significant increase in the wettability contributes to the formation of a thin water film between the spheres and the substrate at the meniscus and this thin water film produces a substantial force - the capillary immersion force which directs the spheres to assemble in a well ordered and close packed structure [208].

The mechanism leading to the self-assembly of the template schematically is as shown below in Figure 4-1.

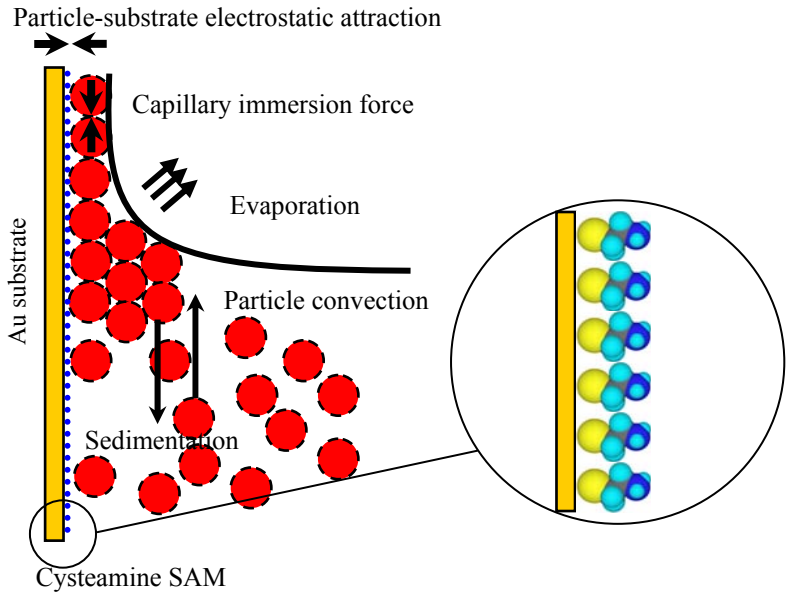

Figure 4-1: Sketch of the particle and water fluxes in the vicinity of monolayer particle arrays growing on gold coated glass substrate. The insert indicates the bonding effect created by the Cysteamine treatment. Figure taken from reference [209].

Figure 4-1 clearly presents the deposition of a template layer of polystyrene spheres. This is driven by these major forces: sedimentation, capillary force, particle convection induced by evaporation and the electrostatic force between the polystyrene sphere and Cysteamine treated gold substrate.

By careful control of the evaporation rate of the suspension, the polystyrene template can be designed into both monolayer and multilayer structures. The arrangement of the spheres in the template was investigated by scanning electron microscopy as shown in Figure 4-2 below. The spheres are close packed in an ordered hexagonal array.

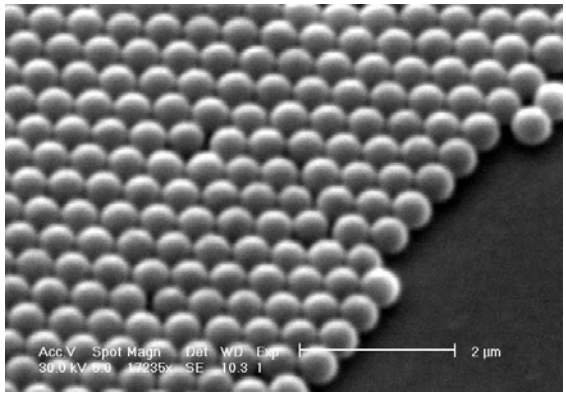

1 layer

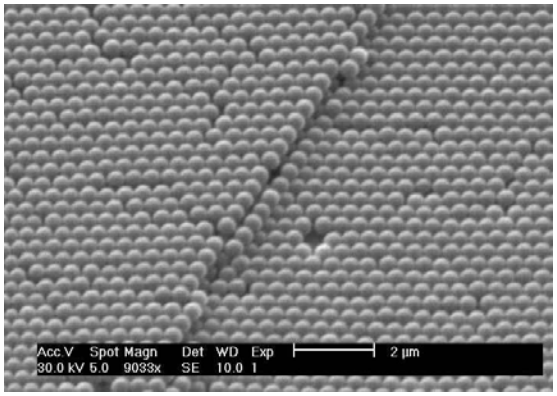

2 layers

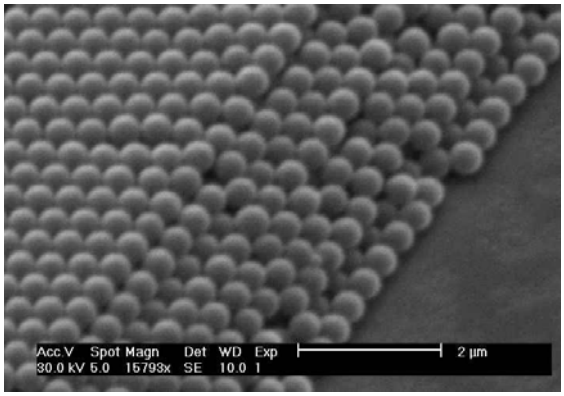

9 layers

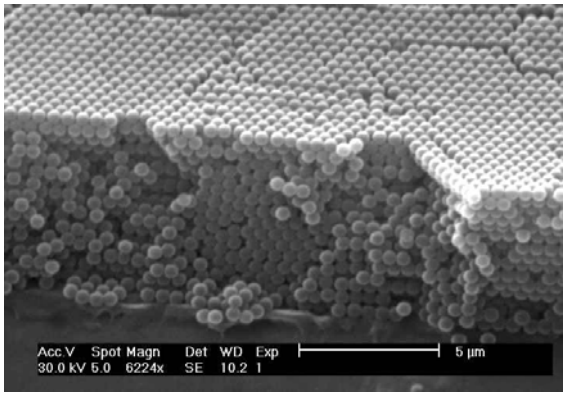

45 layers

Figure 4-2: *Well behaved polystyrene spheres template: monolayer and multilayer, reproduced from reference [210].*

Figure 4-3 presents the SEM images of one multilayered polystyrene template with a sphere diameter of 600 nm made in this work. In contrast to Figure 4-2, the templates shown in Figure 4-3 have defects in the stacking: e.g. dislocations, steps etc.

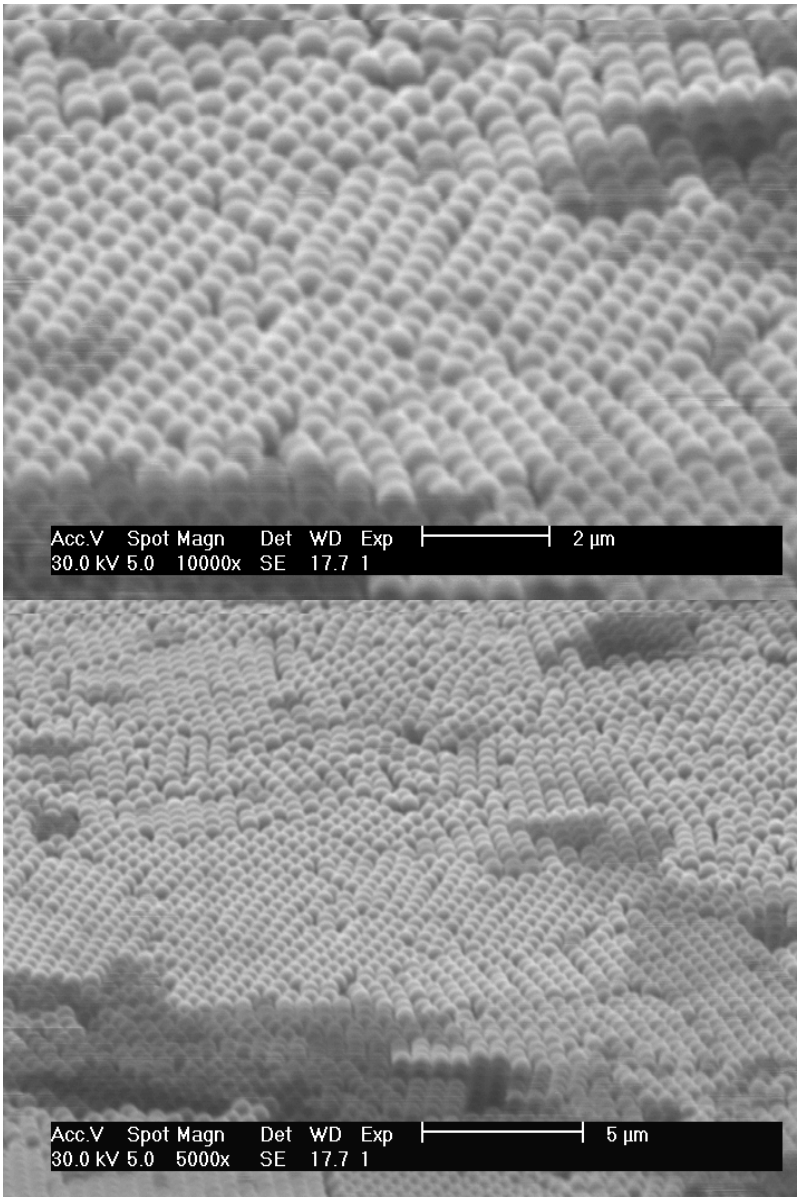

Figure 4-3: SEM image of a large scale of multilayered polystyrene spheres template with sphere diameter 600nm.

A thin gold layer has been sputtered on the surface of the polystyrene sphere template in order to make the template conductive for observation in the high vacuum mode of SEM.

Metal films including gold, platinum, and silver have been electrochemically deposited from aqueous solution through the assembled templates with controlled thicknesses. There were very few reports of metal oxides eg. PbO_2 [99], made from this approach as

described in the introduction. The deposition of iridium oxide films in the present work followed the templated deposition method using a polystyrene template; see Figure 4-4 below for an illustration.

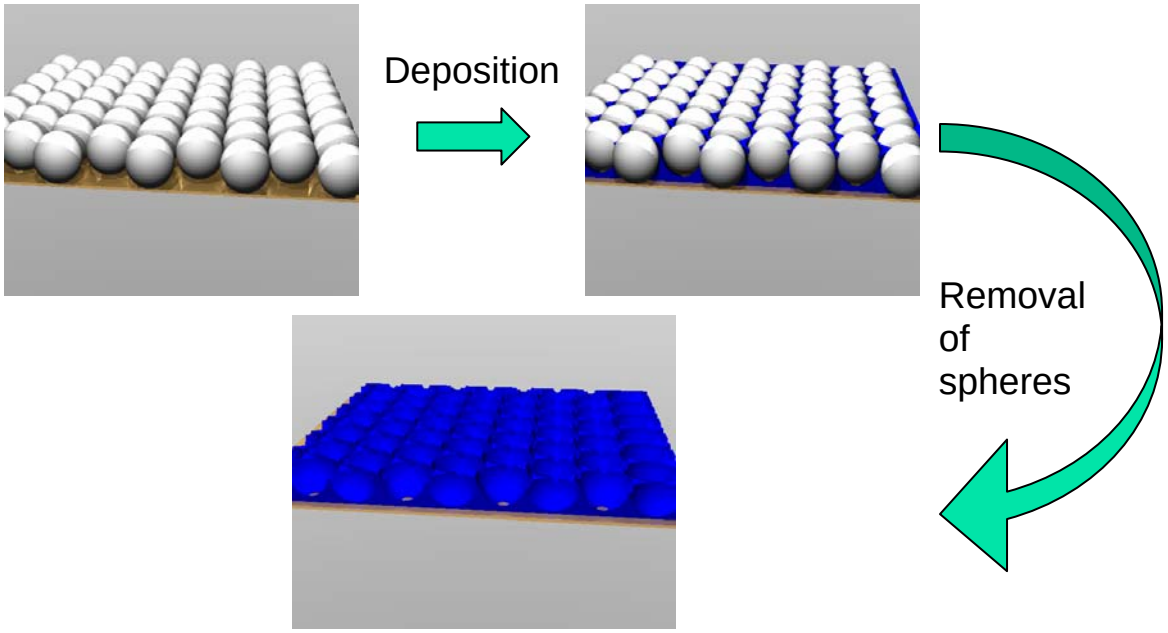

Figure 4-4: The illustration presents a templated electrochemical deposition process for nanostructured IrOx films. The three stages are template assembling, deposition of film and the removal of the spheres.

In this approach, a well ordered hexagonal polystyrene template was formed and the aqueous solution for deposition was made as discussed in chapter 3. Cyclic voltammetry was employed as for the deposition of non-structured IrOx films since it makes it easy to monitor the growth of the film. It is also a useful technique for the fabrication of thickness graded sample. By controlling the cycle numbers, the thickness of the deposition film can be well controlled. When making a thickness graded sample, more cycles can be applied each time the sample is pulled away from the deposition solution. Cyclic voltammetry also allows characterising the films during growth. After the

deposition, the samples were immersed in DMF and sonicated for 30 minutes in order to dissolve the polystyrene template completely.

Scanning electron microscopy was employed to observe the uniformity, surface morphology, and thickness of the structured iridium oxide film. The following figure presents the surface morphology and illustrates the quality of the nanostructured IrOx films. The sample was produced with graded thickness. The three images in Figure 4-5 show different growth stages of the nanostructured IrOx film.

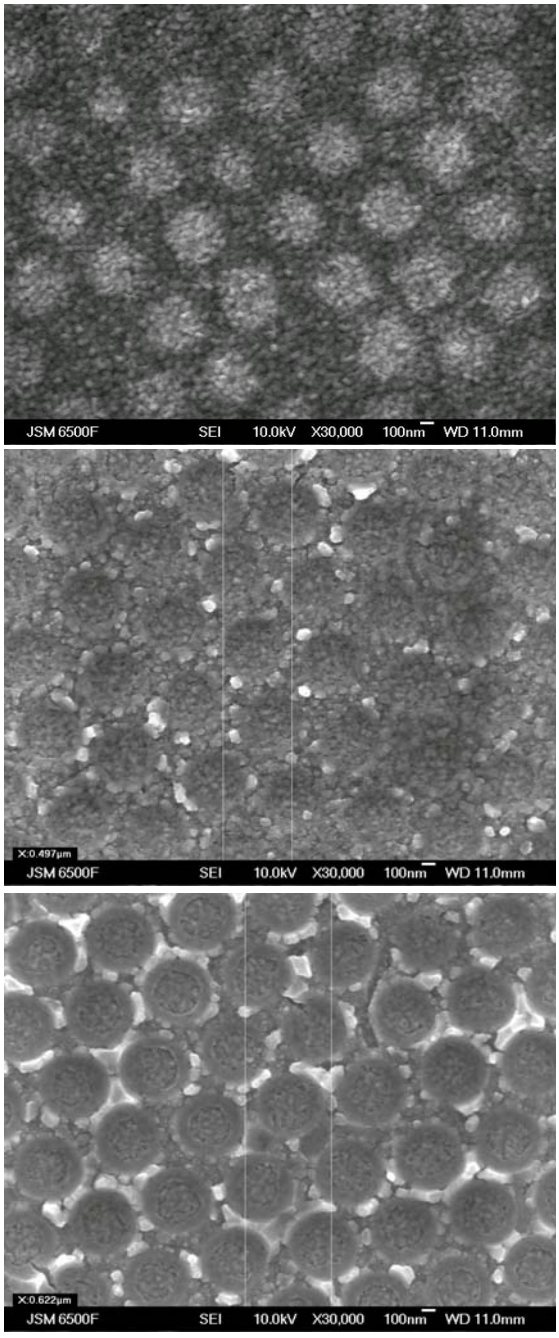

Figure 4-5: SEM pictures of template-deposited IrOx films taken at high magnification with the JSM 6500F. They were produced by cyclic voltammetry through a 600 nm diameter template with graded thickness on the same substrate, potential -0.8 to +0.7 V vs. SCE, 100 mV s^{-1}.From top to bottom, these films were made by 40, 120, and 240 cycles, respectively.

The structured iridium oxide film made with ten cycles is as rough as the evaporated gold surface which can be seen in the centre of the cups formed by IrOx deposits. With so few cycles, the oxide only decorates the underlying substrate texture with so few cycles. When the film gets thicker, the deposit appears granular. With more cycles, cups with smooth walls are clearly visible. The bottom of the film shows the holes left after dissolving the spheres. It can be observed that the internal walls of the cups are very smooth compared to the evaporated gold surface. These pictures indicate that the growth of the nanostructured IrOx film can be finely controlled with the number of voltammetric cycles. As observed with the templated deposition of Au with a well established plating bath containing additives such as brighteners, the templated deposition of IrOx produces very smooth cup walls despite the absence of additives designed to control the texture of the deposit.

In this work, the film thickness can be calculated from the diameter of the cavity. The illustration in the following figure describes how the film thickness can be related to the cavity diameter.

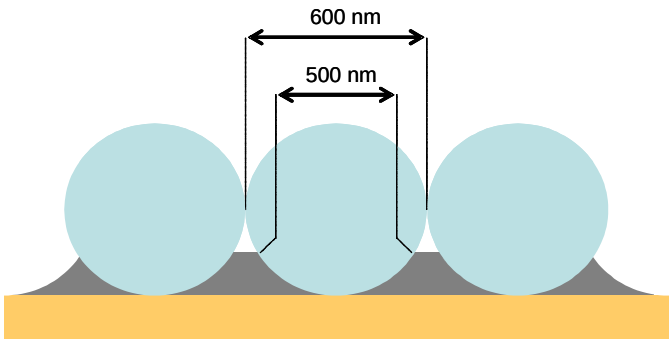

Figure 4-6: Illustration of the relationship between the film height and sphere diameter. Spheres of 600 nm diameter are shown as example.

When the nanostructured IrOx film has a cavity diameter equal to the sphere diameter, the film will have a thickness of half sphere diameter height. The thickness of thin films

can be estimated from the diameter of the cup and relating this to the diameter of the spheres. The calculation details will be discussed further in Chapter 5. In the following chapters, the film thickness will be described in terms of the sphere diameter *d.* 600 nm spheres are used throughout unless specified otherwise.

Figure 4-7 shows that the nanostructured IrOx film produced by cyclic voltammetry with Yamanaka's recipe has a very ordered hexagonal structure. The film is very uniform when observing at a magnification of 10,000. The only defects observed on this figure appear to be differences in the morphology of the top of the IrOx walls. Some walls appear to have smooth "tops" and others appear to have granular "tops". Uniform films as shown below were reliably made up to 4 cm^2. No attempt was made to produce larger surfaces.

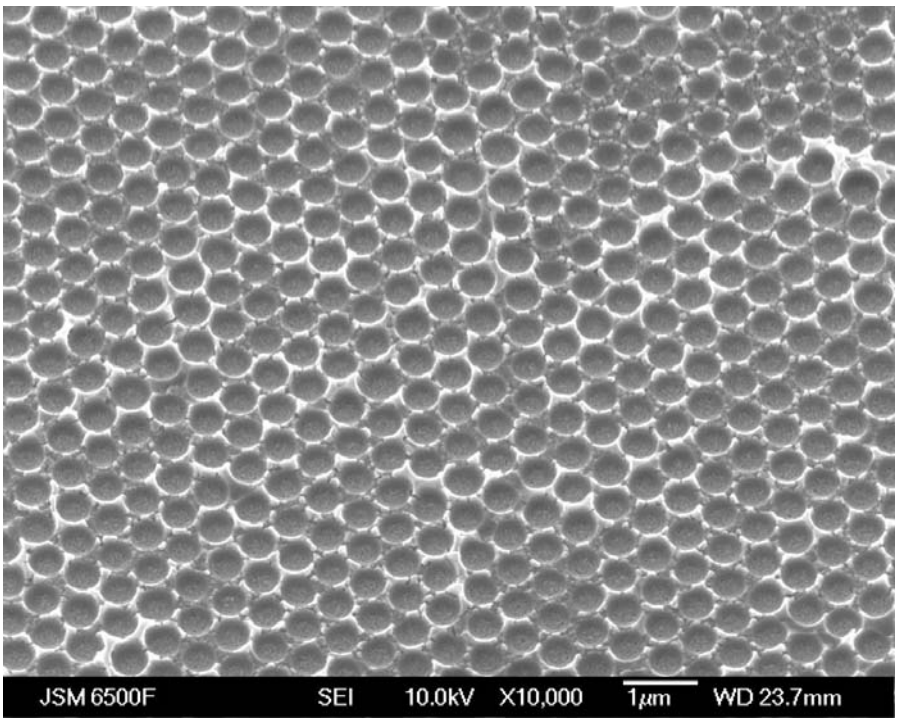

Figure 4-7: SEM picture of structured IrOx film produced by cyclic voltammetry through a 600 nm diameter template (potential cycles between -0.8 and +0.7 V vs. SCE at 100 mV s^{-1}*).*

The SEM images clearly prove that nanostructured IrOx films can be electrochemically deposited with a polystyrene template. The thickness of the structured film appears to be uniform and the film presents a hexagonal structure over a long range. However, in this approach, nanostructured IrOx films grown to more than one template layer tend to crack as shown in Figure 4-8.

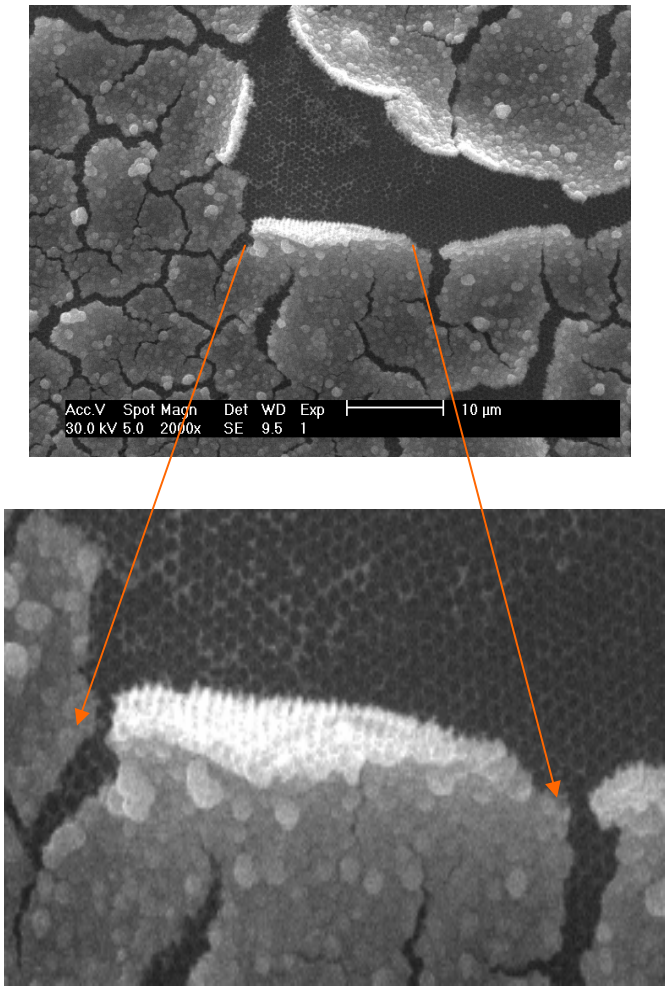

Figure 4-8: Films crack when grown to thicknesses greater than one template layer.

As indicated by Figure 4-8, the IrOx film grown to a film thickness around 1 diameter spheres height breaks at about half diameter height after immersing the film in DMF solution. The part of the film that peels off, Figure 4-8 seems to suggest that it might be possible to prepare free-standing nanostructured IrOx films however no attempt was made to prepare such films. There are a few possibilities which might explain the crack phenomenon: the gaps between the spheres at half diameter height are very narrow for IrOx deposition; IrOx itself is very brittle; the solvent, DMF, may cause the spheres to swell before dissolving them. Further research was carried out to find out the problem and solve the crack phenomenon.

4.1.2 Fabrication of multilayer nanostructured IrOx films

Multilayers of the nanostructured IrOx films can be synthesised in the same procedure with a multilayer template. As shown in Section 4.1.1, the film thickness increases when increasing the number of voltammetric cycles during deposition. Figure 4-9 below presents multilayered nanostructured IrOx films prepared by applying up to 400 scans.

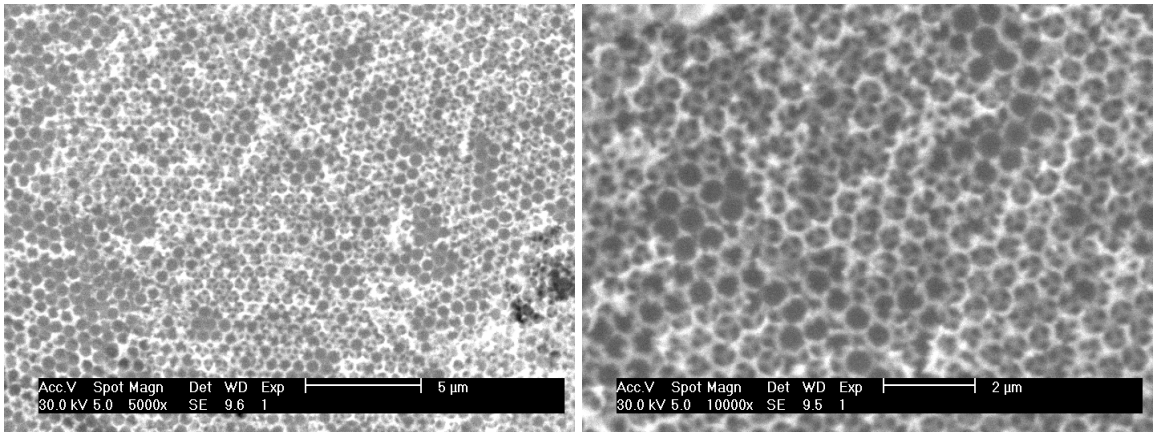

Figure 4-9: Multilayer growth of nanostructured IrOx films by cyclic voltammetry through a 600 nm diameter template (potential cycles up to 400 scans between -0.8 and +0.7 V vs. SCE at 100 mV s^{-1}).

Although the bulk of the film appeared to crack during dissolution of the spheres; some regions show evidence of multilayers. The SEM pictures show at least two layers of nanostructured IrOx films have been achieved. Regions with multilayers present a well ordered hexagonal honeycomb structure. The film has peeled off during dissolution and only ½ *d* height is left in some regions whereas other parts clearly show multilayers. This could be because of the brittleness of IrOx films and of the swelling of the sphere during their dissolution.

It is challenging to produce 3D structures but it is also useful for some applications. Multilayer nanostructures can greatly enhance the surface area; this could be useful to make pH sensors (a larger electroactive area would help define the film potential) or transmittance cell (the transmittance depends on the film thickness). It will also be useful for the study of the optical and electrochromic properties of IrOx films which will be presented in Chapter 6.

4.2 Improvement and control

4.2.1 Heat treatment

The Raman spectra for the electrochemically deposited IrOx films from both as deposited and annealed film shown in Chapter 3 show that the IrOx film can turn crystalline with heat treatment at 460 ºC for an hour. The nanostructured film is expected not to crack with heat treatment since the template is kept in the film without dissolution in DMF. The nanostructured IrOx film was treated under the same condition as the flat IrOx thin film. The nanostructured IrOx film was first produced by cyclic voltammetry through a 600 nm diameter template (100 cycles, potential between -0.8 and +0.7 V vs. SCE at 100 mV s^{-1}). After deposition, the IrOx film was placed in a furnace under oxygen atmosphere for an hour instead of immersing in the DMF solution. The polystyrene template inside the nanostructured film burned down at around 90 ºC according to the experiment result. The temperature in the furnace was increased slowly to 460 ºC with a rate of 5 ºC per minute. These conditions were obtained by trial and error.

After heat treatment, SEM was used to characterise the nanostructured IrOx film. Figure 4-10 below presents the SEM images of the films after annealing.

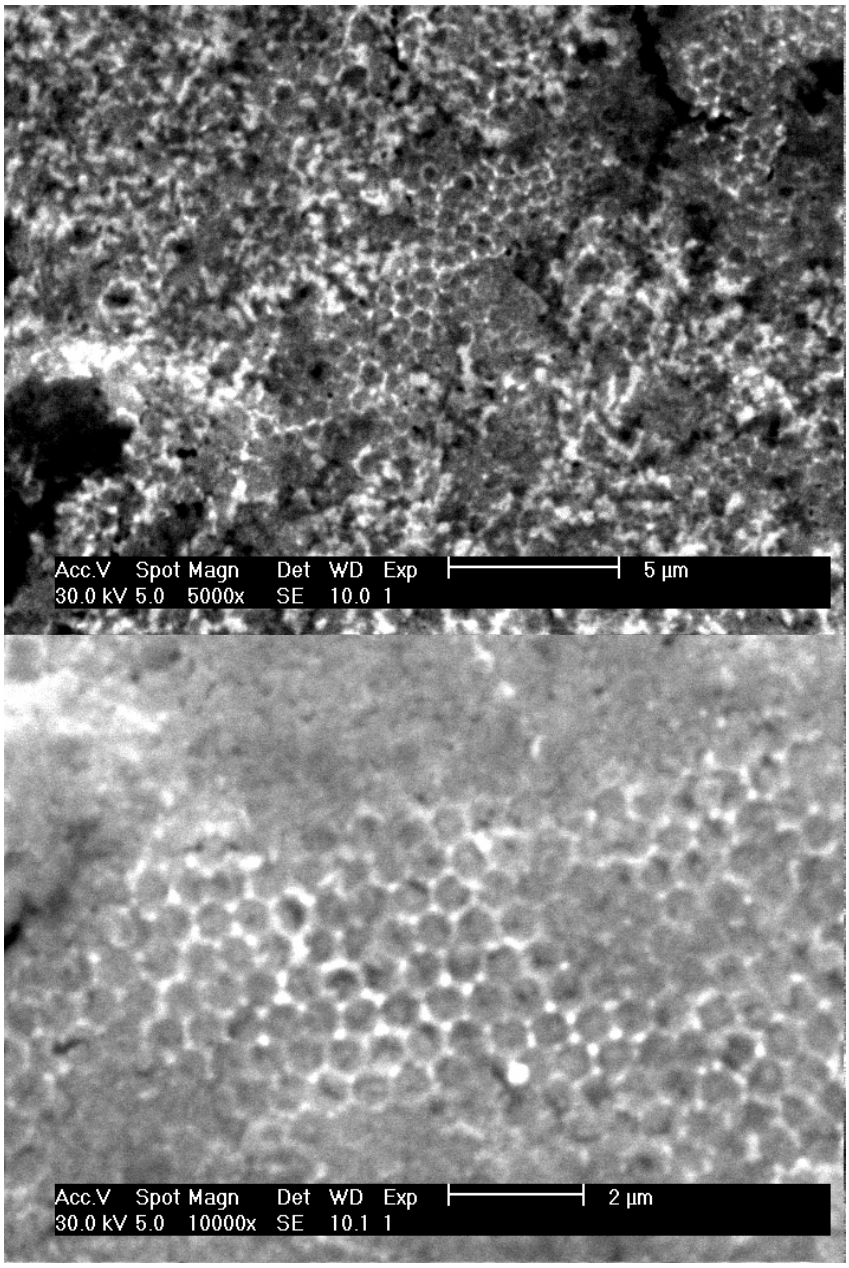

Figure 4-10: SEM images of an electrochemically deposited nanostructured IrOx film after heat treatment. The heat treatment was carried out in an oxygen atmosphere at 460 ºC for one hour. The lower picture is a magnified part of the top picture.

Heat treatment destroyed most of the nanostructure and the film became rough and mostly disordered when observed with the microscope. The structure of the nanostructured IrOx film deposited electrochemically was converted into crystalline at high temperature according to the Raman spectra of the flat IrOx films in Section 3.2.6. However, this method did not produce a good nanostructured film. In addition, IrOx films tend to lose their electrochromic property when treated at high temperature due to the dehydration of the film [211].

4.2.2 Different approaches to remove the template without damaging the film

Various polymer solvents have been used to dissolve the polystyrene spheres. Toluene, THF, acetone, and DMF have all been employed in removing polystyrene template from a metal nanostructure by the researchers in the group. DMF has been recognised to be the best at solubilising polystyrene based on numerous attempts in the laboratory. However, the nanostructured IrOx films tend to crack after immersing in DMF. The mechanism of polystyrene dissolution in these solvents is thought to start with a swelling process. The polymer chains of the polystyrene sphere expand in presence of these solvents and the volume of the sphere increases. This is thought to fracture the film around ½ *d*, where the vertical walls separating the spheres are the thinnest. To prevent the collapse of the film, the template should therefore be removed either by dissolution of the spheres without swelling or by decomposition of the spheres. Concentrated sulphuric acid and cyclohexane were employed to remove the polystyrene sphere without damage to the film.

Concentrated sulphuric acid is highly reactive towards polystyrene and it should decompose the polystyrene spheres by breaking the polymer chains into smaller units. Thus it should gradually reduce the diameter of the spheres without swelling. Nanostructured IrOx films were synthesised by voltammetric deposition. Figure 4-11 below shows a SEM micrograph of a nanostructured IrOx film deposited on a gold substrate with 600 nm cavity diameters. The spheres were removed by immersion in

sulphuric acid over night under room temperature. The picture clearly illustrates that the nanostructure collapsed producing a film less than one sphere diameter thick after repeated attempts. Experimental results therefore indicate that sulphuric acid is not able to remove the template without damaging the film. This also agreed to the results shown in section 3.2.2 where the films are not stable in weak acid.

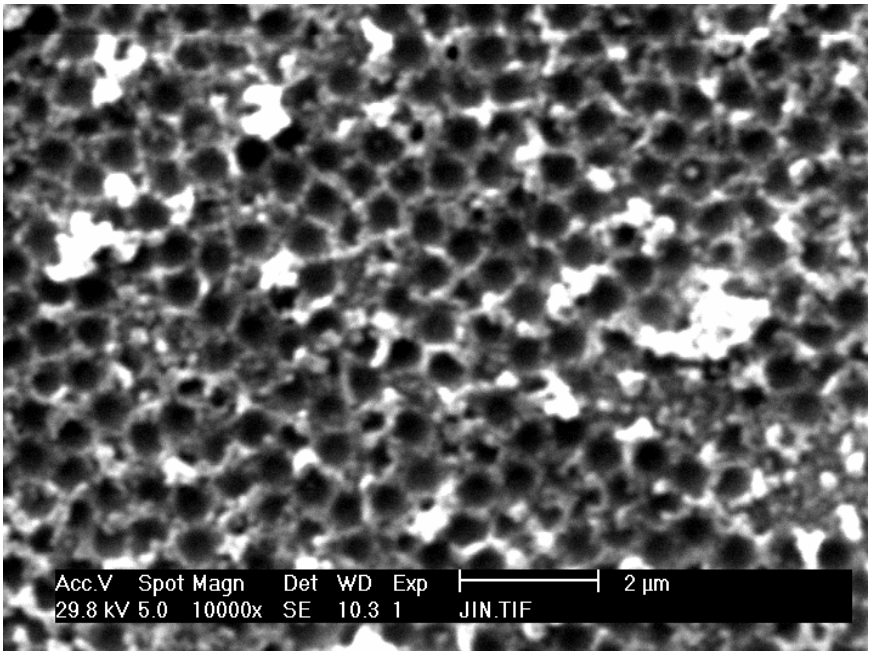

Figure 4-11: Nanostructured IrOx film deposited on a gold substrate through a 600 nm diameter polystyrene template. The template was removed by immersion in concentrated sulphuric acid overnight at room temperature but the structure collapsed at 0.5 d.

Cyclohexane is known as a non-polar solvent for chemicals. It dissolves polystyrene without swelling. Nanostructured IrOx films were synthesised with the electrochemical deposition using cyclic voltammetry. Figure 4-12 below presents a SEM micrograph of a nanostructured IrOx film deposited on a gold substrate through 600 nm diameter polystyrene spheres. The film was immediately immersed in cyclohexane for a week after deposition at room temperature. The dissolving time of one week is based on a systematic study by changing the dissolution time gradually from a day to a week. The SEM

micrograph in Figure 4-12 shows a very ordered smooth film with no apparent cracks. According to the illustration in Figure 4-6, the film has a thickness circa 0.75 sphere diameter. The film thickness is thicker than 0.5 *d* otherwise it will appear as the micrograph in Figure 4-3.

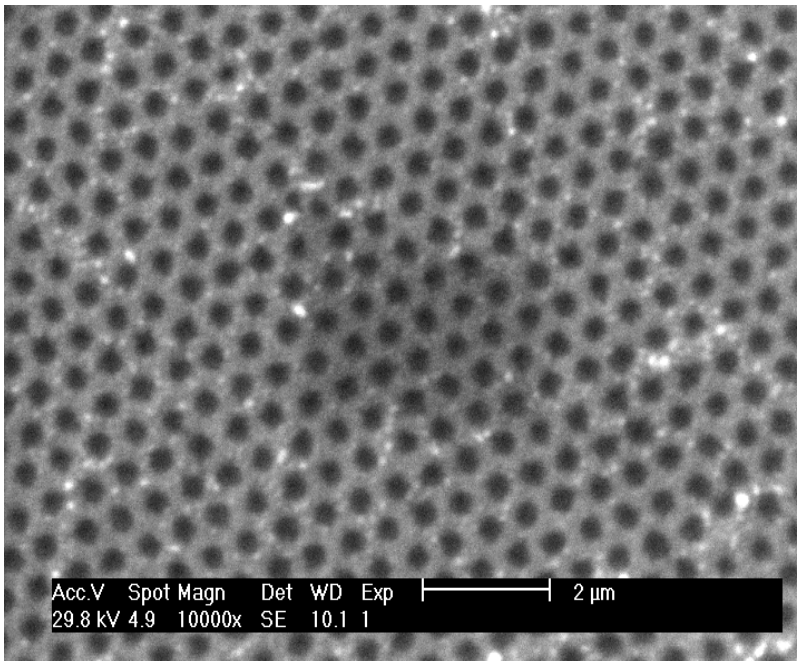

Figure 4-12: Nanostructured IrOx film deposited on a gold substrate through a 600 nm diameter polystyrene template. The template was removed by immersion in cyclohexane for a week at room temperature. From the pore diameter the film thickness is estimated to be circa ¾ d i.e. ~450 nm. The structure remains upstanding without crack.

The image of the SEM micrograph of nanostructured IrOx film after dissolution of the spheres in cyclohexane can be obtained repeatedly under the same condition. Cyclohexane was therefore used to remove multilayer templates when fabricating multilayer nanostructured IrOx films. The SEM picture presented in Figure 4-13 below shows a nanostructured IrOx film with a film thickness of ~1.5 sphere diameter. The polystyrene spheres used for fabrication have a diameter of 600 nm. The nanostructured IrOx film has a very ordered hexagonal distribution of pores inside which can be seen as

a sub-structure of lines converging at roughly 120 degree towards each other. This is characteristic of the honeycomb structure produced when the film grows beyond one template layer as observed previously with other materials. The film is smooth, uniform and continuous with no crack or break. Cyclohexane proved to be a non-swelling solvent for polystyrene. The disadvantage of cyclohexane as solvent is the time scale. It takes at least a week to remove the polystyrene template completely.

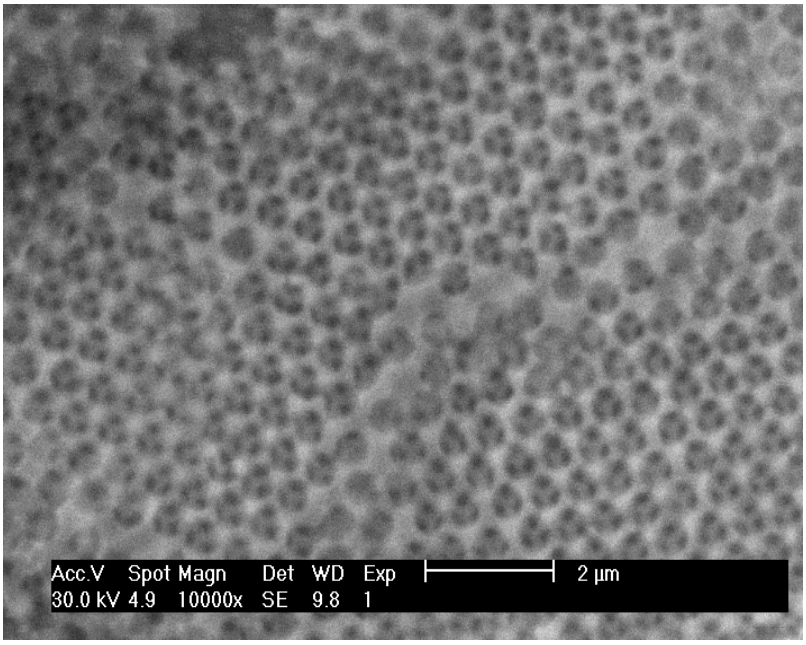

Figure 4-13: Multilayer nanostructured IrOx film deposited on a gold substrate through a 600 nm diameter polystyrene template. The template was removed by immersion in cyclohexane for a week at room temperature. From the pore diameters, the film was estimated to be about 1.5 sphere diameter thick. The structure is very ordered, honeycomb like, with no crack or collapse.

4.2.3 Deposition of nanostructured IrOx films with different size templates

Nanostructured IrOx films with different cavity sizes were fabricated by using polystyrene templates formed with different diameter spheres. Figures 4-14 and 4-15 present SEM micrographs of IrOx films electrochemically deposited through self-assembled templates respectively made with 500 nm and 1.6 μm diameter polystyrene spheres.

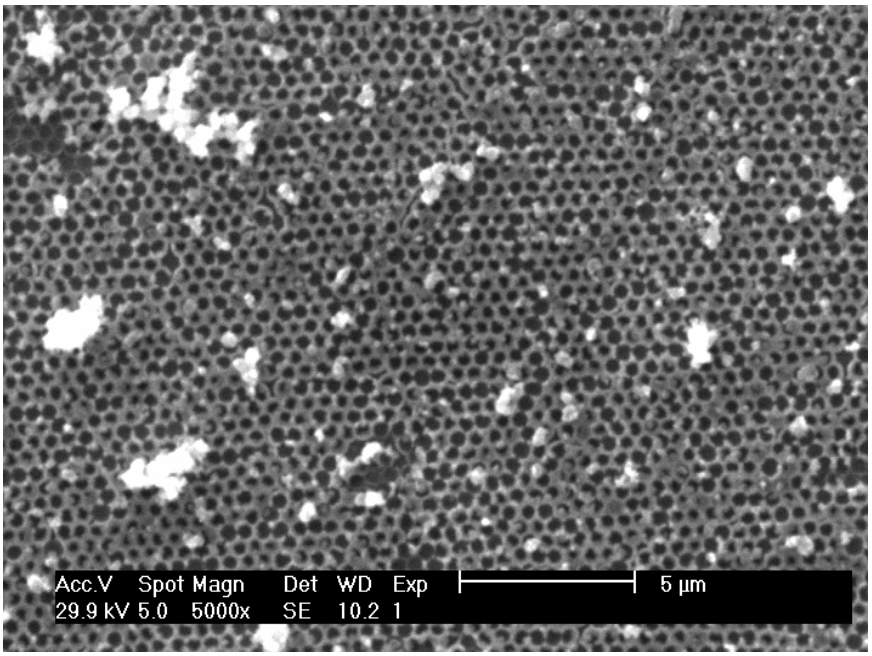

Figure 4-14: SEM micrograph of an IrOx film electrochemically deposited through a template made with 500 nm diameter polystyrene spheres. The film thickness is estimated to be half a sphere diameter thick.

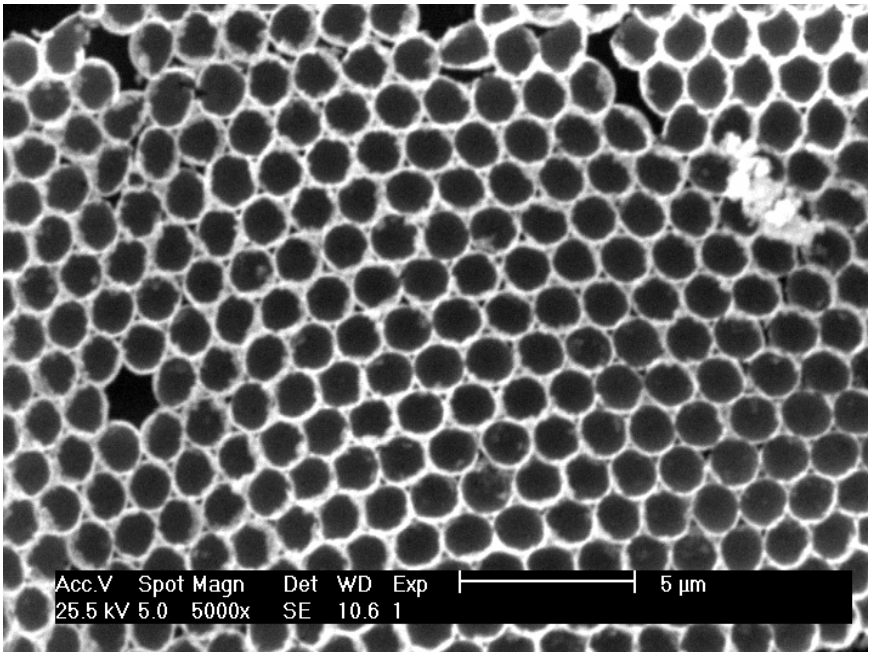

Figure 4-15: SEM micrograph of an IrOx film electrochemically deposited through a template made with 1.6 µm diameter polystyrene spheres. The film thickness is estimated to be half a sphere diameter thick.

Both films present a hexagonal close pack distribution of cavities as observed with 600 nm diameter spheres. The white particles appears on the film in both Figure 4-14 and Figure 4-15 are both large deposits of IrOx film. The film prepared with the large spheres appears to have grown around the spheres, thus leaving a void where three spheres join up. Such defect was not observed with smaller spheres. A similar defect also appears when growing polymers [80]. The SEM micrographs clearly show that nanostructured IrOx films can be prepared with a range of cavity diameters simply by choosing the dimension of the spheres used to make the template. So far, IrOx films made with polystyrene templates with a sphere diameter ranging from 400 nm (on ITO substrate) to 1.6 µm have been successfully synthesised in this work.

4.2.4 Nanostructured IrOx films deposited on ITO

IrOx films can be electrochemical deposited on a wide range of substrates: pure iridium, glassy carbon, gold, indium tin oxide (ITO) and titanium. In this work, nanostructured IrOx films have also been deposited on an ITO coated glass substrate in order to study the transmittance of the nanostructured IrOx film, see Chapter 6 for transmittance results. Unlike the deposition on gold substrate, the ITO substrate has not been treated in cysteamine ethanolic solution since the covalent bond cannot form between the thiol group and the ITO substrate. Therefore, the synthesis self-assembly of the polystyrene template on an ITO substrate is more difficult to control. However, the preparation of the template on ITO substrate is identical to those on gold surface apart from the absence of cysteamine treatment.

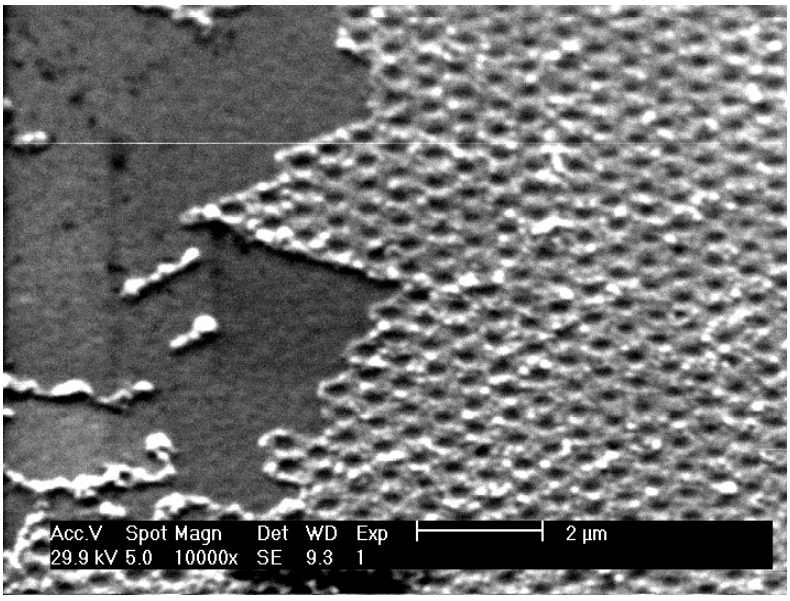

Figure 4-16: SEM micrograph of a nanostructured IrOx film deposited on an ITO substrate with a 600 nm Ø template. Half of the sample was scratched to observe the roughness of the substrate.

Figure 4-16 presents a SEM micrograph of a nanostructured IrOx film deposited on an ITO substrate with a 600 nm diameter polystyrene sphere template. The reason for choosing this substrate is that ITO is transparent and therefore makes it possible to assess the transmittance of the nanostructured films, see next chapter. The film was scratched deliberately in order to observe the surface roughness of the ITO glass surface. Compared with gold substrate, the ITO substrate is less rough under SEM observation at 1-2 μm scale.

Figure 4-17 gives a set of SEM micrographs of a thickness-graded nanostructured IrOx film deposited on the ITO substrate. From top to bottom, SEM images present a very thin film, circa ¼ *d*, a thicker film and a ½ *d* thick film. The three pictures clearly show that the film has the same structure on ITO substrates as that on gold substrates.

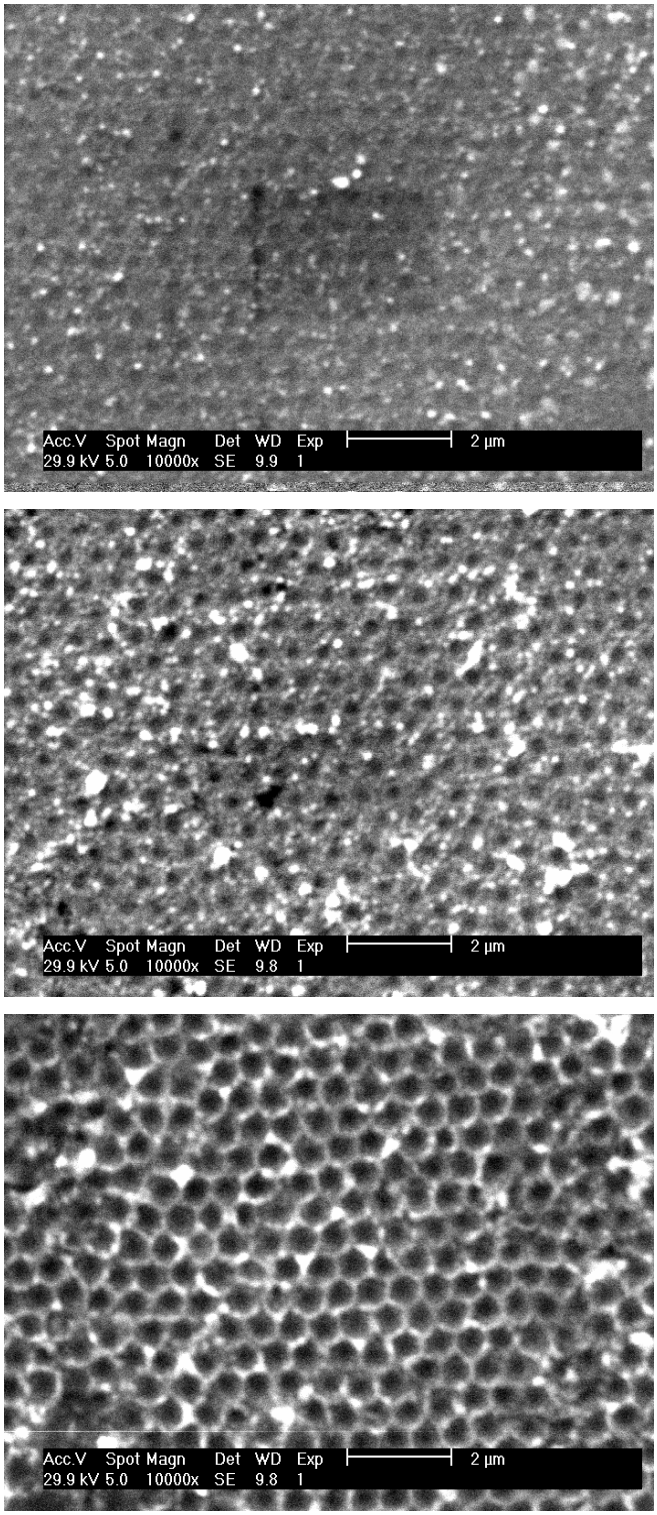

Figure 4-17: Nanostructured IrOx film (600 nm diameter) graded in thickness deposited on the ITO substrate. The film thickness increases from top to bottom.

The preparation of multilayer nanostructured IrOx films was attempted on an ITO substrate. In this work, it was found that the multilayer templates were less stable on ITO than on gold substrates. It was not possible to successfully deposit multilayer films on ITO substrates.

4.3 Summary and conclusion of Chapter Four

Polystyrene spheres are self assembled on cysteamine treated gold coated glass substrate driven by capillary force. These polystyrene templates can be controlled into both monolayer and multilayer structures. Nanostructured IrOx films were successfully deposited through these templates with cyclic voltammetry. Monolayer and multilayer nanostructured IrOx films were fabricated through monolayer and multilayer polystyrene templates respectively. These films are very uniform and have an ordered hexagonal structure. Multilayered nanostructured IrOx films even show a 3 D honeycomb structure. Nanostructured IrOx films can be made into graded thicknesses. The increase of film thickness can be observed by applying more cycles when depositing with cyclic voltammetry.

SEM images indicate the nanostructured cavities of IrOx tend to crack at the height of half sphere diameter and multilayer nanostructured IrOx films are often discontinuous when the polystyrene spheres are removed by immersion in DMF. Although DMF has been reported as an excellent solvent for polystyrene, the dissolution process is thought to first involve the swelling of the polystyrene spheres and the subsequent rupture of the IrOx structure. Hence this approach is not suitable for brittle metal oxide films such as ZnO, IrOx etc. Sulphuric acid and cyclohexane were tested to dissolve polystyrene spheres as alternative options. Immersion in acid removed the template but also broke the film at ½ *d*. In contrast, cyclohexane successfully dissolved the polystyrene template without breaking the film. However, this is long and typically required a week. Heat treatment was tried in order to increase the strength of the nanostructured IrOx films, but without success.

Nanostructured IrOx films were successfully deposited through 400 nm, 500nm, 600 nm and 1.6 μm diameter polystyrene templates with cyclic voltammetry. No other template size was investigated. Already this provides a wide range of choice for the cavity diameter of the nanostructured IrOx film. When combined with the range of film thicknesses available by controlling the number of voltammetric cycles, this generates a significant range of film geometries and structures. Nanostructured IrOx films were deposited on an ITO substrate through self-assembled polystyrene templates. This opens up the range of applications to optics and electrochromism.

After successfully depositing IrOx films both structured and non-structured, it is of our interest to study the thickness control during the electrochemical growth of the film.

5 Thickness control of electrochemical growth of IrOx films for both nanostructured and non structured IrOx films

5.1 SEM estimation of the thickness of IrOx films

5.1.1 SEM estimation of the thickness of non-structured IrOx film

One of the project objectives was to be able to grow non templated films with defined thicknesses; therefore it was important to estimate the dependence of the film thickness on the growing conditions. In this section, a flat thickness-graded IrOx film was produced to study the relationship between the film thickness and the number of voltammetric cycles. This was achieved by gradually lifting the substrate out of the deposition solution using a microstage to carefully control the immersion depth as described in Chapter two. The flat films were fabricated on a gold coated glass substrate with potential cycles between -0.8 and +0.7 V vs. SCE.

Figure 5-1 below shows SEM pictures taken from the side of the thickness-graded sample made with 20, 40, 60, 80, 100, and 120 cycles. The SEM pictures were taken with the microstage holding the sample tilted to 60°. It was difficult to obtain higher resolution images with the instrument used (Philips ESEM XL30) however the figures qualitatively prove that the thickness of the non-structured film is increasing with the cycle number.

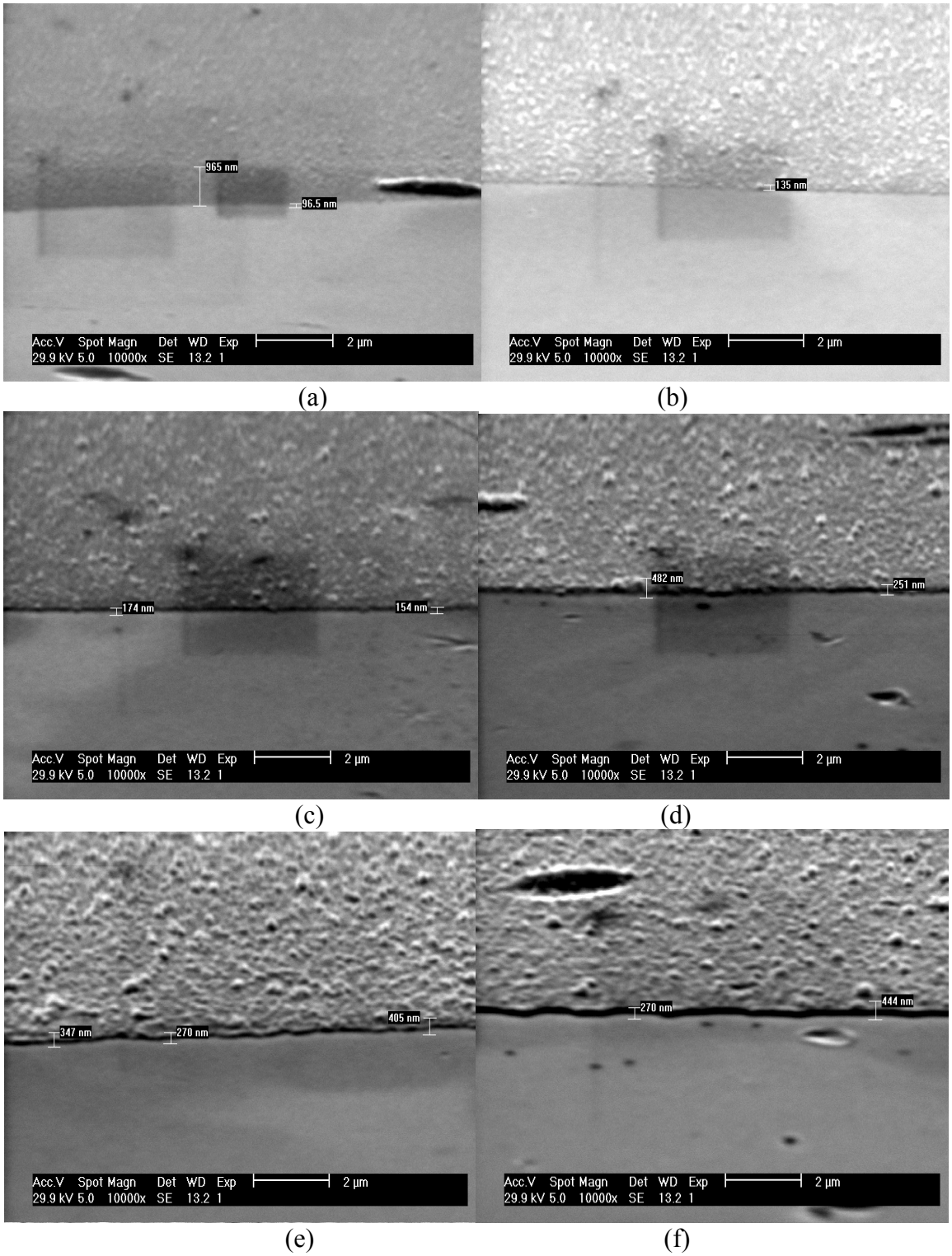

Figure 5-1: Side view of films grown with 20 (a), 40 (b), 60 (c), 80 (d), 100 (e), and 120 (f) cycles without template. These films have estimated thicknesses of 90 nm, 135 nm, 174 nm, 251 nm, 270 nm and 270 nm respectively with a 50 nm estimated error.

As discussed in the experimental section, the films were grown in a designed area using a painting insulation solvent (commercial nail polish).Nail polish was painted on the area of the substrate which was not needed for deposition. The area without nail polish stay conducted and deposition took place on this area. After deposition, films were dipped in DMF in order to dissolve the nail polish. Thus, a clear film edge can be observed in those SEM micrographs. The film thickness was estimated after ignoring the height of the granules observed as the SEM micrographs. The film thickness measured in this way has a huge error at least ± 50 nm based on Figure 5.1.a. The height of the edge between the iridium oxide film and the substrate increases as the cycle number increases.

Since the microstage with the sample holder was tilted to 60^{o}, the real film thickness was calculated according to the trigonometry described in Figure 5.2 below.

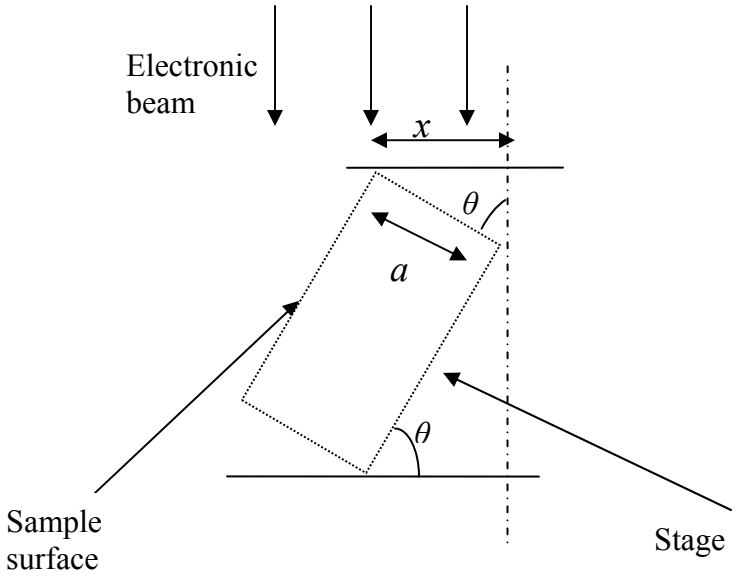

Figure 5-2: Schematic illustrating the trigonometry used to estimate the film thickness of nanostructured film.

where

θ = the angle to which the sample is tilted in the SEM

x = the thickness measured by SEM as seen in the SEM micrograph

a = the real film thickness

therefore

$$a = x / \sin \theta \qquad \textit{Equation 5-1}$$

The calculated film thicknesses are shown in table 5-1 below.

Table 5-1: SEM estimated film thicknesses of non structured IrOx film after sample tilt correction

Voltammetric Cycle number	**Film thickness (*a*) / nm**
20	111 ± 11
40	156 ± 20
60	201 ± 20
80	290 ± 30
100	312 ± 50
120	312 ± 100

The table clearly shows that the film thickness increases with the voltammetric cycle number. To study the relationship between the film thickness and cycle number numerically, the data from the Table 5-1 are transferred into a plot. Figure 5-3 presents a plot of the film thickness against potential cycle number for both flat and structured films. The data is based on the SEM estimation with a correction due to the stage angle.

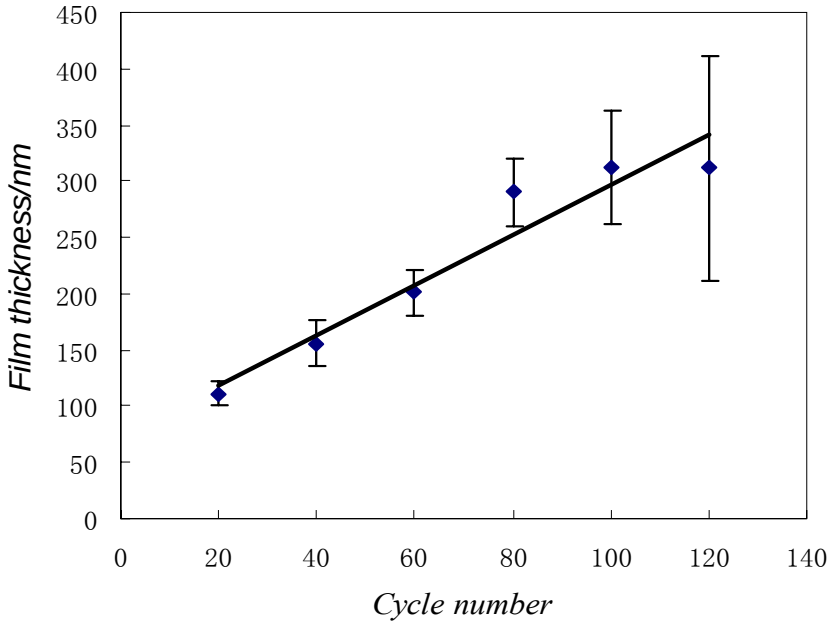

Figure 5-3: Plot of the film thickness against potential cycle numbers for non structured films. The thickness was estimated by SEM.

The plot suggests that the film thickness of the non structured IrOx film increases nearly linearly with the cycle number with a large error bar.

5.1.2 SEM estimation of the thickness of nanostructured IrOx films

In this section, a nanostructured iridium oxide film was produced graded in thickness to study the relationship between film thickness and the voltammetric cycle numbers. This was achieved by gradually lifting the substrate out of the deposition solution using a microstage to carefully control the immersion depth as described in chapter two. A 600 nm diameter polystyrene template was used to make the nanocavities. When the electrochemical deposition was complete the samples were soaked in DMF to dissolve the polystyrene template. Both the flat and structured films were fabricated on a gold coated glass substrate with potential cycles between -0.8 and +0.7 V vs. SCE at 100 mV s^{-1}.

SEM pictures were taken from the side of the nanostructured sample with the microstage holding the sample tilted 60^{o}. Figure 5-4 below shows the structured film fabricated with a series of steps from 20 to 240 cycles with 20 cycle increments. Attempts were made to determine the film thickness with the SEM, however, the height of the edge of the nanostructured film turned out to be very rough and it is difficult to determine the film thickness accurately. This is a common difficulty encountered with films made by templated deposition and is not specific to IrOx films.

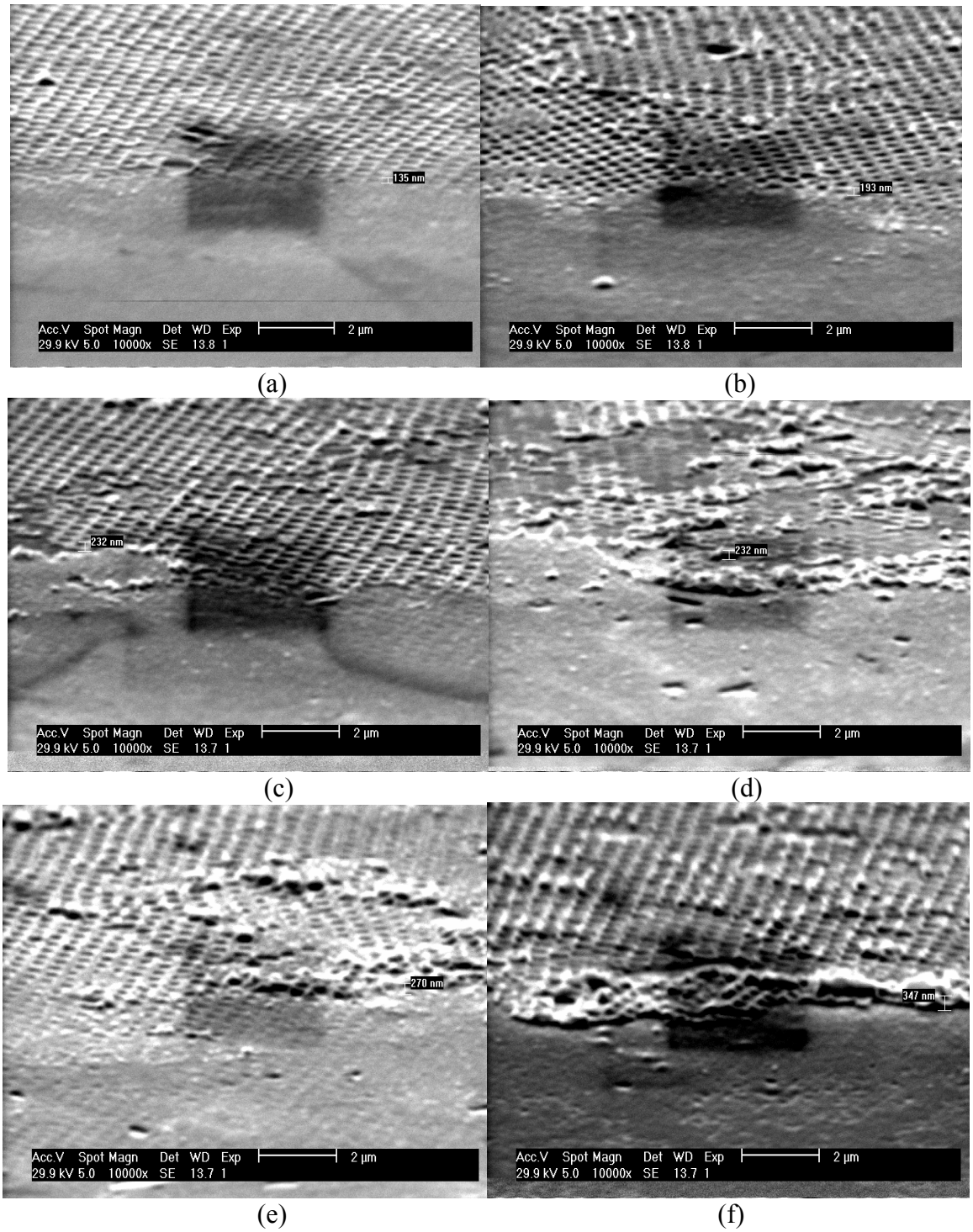

Figure 5-4: Side views of graded nanostructured Iridium oxide films on a gold coated glass. Pictures show the film regions corresponding to cycle number 40 (a), 80 (b), 120 (c), 160 (d), 200 (e) and 240 (f).

Since films in the SEM micrographs in Figure 5-4 show no edge at all, the estimating of the nanostructured IrOx film thickness is actually impossible. The black shades observed in those micrographs are caused by SEM electron damage after focusing at those areas with higher magnitude. In contrast to the non structured IrOx films, the tendency of film thickness to increase with voltammetric cycle numbers is not clear.

It is noticeable that the films look remarkably similar despite a significant difference in cycle number between the pictures. Some thicker patches are visible but otherwise all the films seem to have a thickness less than 1/2 *d*.

5.2 Estimation of IrOx film thickness with the voltammetric charges

5.2.1 Estimation of film thickness with the voltammetric charges for non-structured IrOx films

Flat thin films were deposited on a gold slide in order to study the mechanism of electrochemical deposition and the quality of the iridium oxide films. The gold slide was cleaned thoroughly before deposition and an area of 0.25 cm^2 was defined by painting insulation solvent around for deposition in order to calculate the charge density. In the next section, the same procedure is reported for a structured film to build up a comparison between non-structured and structured films. Figure 5-5 below is a set of cyclic voltammograms recorded for the electrochemical deposition of a non-structured IrOx film. The potential range is between -0.8 V and +0.7 V and the scan rate is 100 mV s^{-1}.

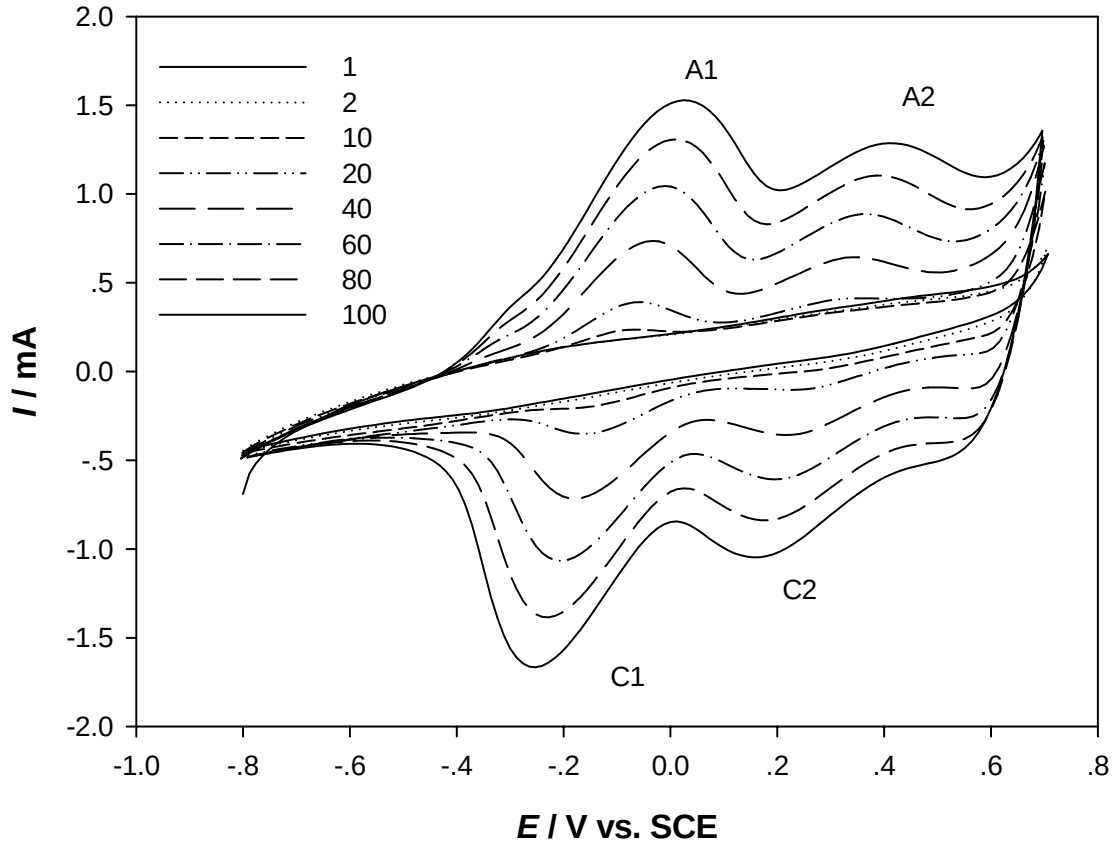

Figure 5-5: Voltammograms for the growth of IrO_x on a gold electrode from the electrochemical deposition solution (pH = 10). Potential range: –0.8 to+0.7V, scan rate: 100 mV s^{-1}. The electroactive area is 0.25 cm^2. Number 1, 2, 10…, 100 indicate the voltammetric cycle number.

By integrating the peak area using the Autolab programme, the charge passed during the deposition of IrOx film can be obtained for each cycle. The starting and the ending potential can be set up with the Autolab. The first cycle is used as the baseline. The charge against each cycle during deposition is presented in the table below:

Table 5-2: The anodic and cathodic charges recorded for different cycles during deposition of flat IrOx films. In this table, $Q\,a = Q_{A1} + Q_{A2}$, $Q\,c = Q_{C1} + Q_{C2}$, where A1, A2, C1, C2 are the peaks shown in Figure 5.5.

Number of voltammetric cycles	***Qa* / mC**	***Qc* / mC**
1	4.3 ± 0.2	-2.9 ± 0.2
2	4.1 ± 0.2	-2.7 ± 0.1
3	4.0 ± 0.2	-2.8 ± 0.1
4	4.1 ± 0.2	-2.8 ± 0.1
5	4.1 ± 0.2	-2.8 ± 0.1
6	4.1 ± 0.2	-2.8 ± 0.1
7	4.1 ± 0.2	-2.8 ± 0.1
8	4.2 ± 0.2	-2.9 ± 0.2
9	4.2 ± 0.2	-2.9 ± 0.2
10	4.2 ± 0.2	-3.0 ± 0.2
20	4.8 ± 0.2	-3.6 ± 0.2
30	5.6 ± 0.3	-4.4 ± 0.2
40	6.5 ± 0.3	-5.4 ± 0.3
50	7.6 ± 0.4	-6.5 ± 0.3
60	8.6 ± 0.4	-7.7 ± 0.3
70	9.6 ± 0.5	-8.7 ± 0.4
80	10.6 ± 0.6	-9.7 ± 0.5
90	11.6 ± 0.6	-10.8 ± 0.5
100	12.5 ± 0.6	-11.8 ± 0.7

Since

$$Q = V\, d_M\, n\, F / M_w \qquad \textit{Equation 5-2}$$

Where d_M is the density of iridium oxide, n is the number of electrons transferred, F is the Faraday constant and M_w is the molecular weight of iridium oxide.

and

$$V = A \times h \qquad \textit{Equation 5-3}$$

Where A is the surface area. So, h, the thickness of the deposited IrOx film can be easily calculated using equation 5.2 and 5.3

$$h = \frac{QM_w}{nd_M FA} \qquad \textit{Equation 5-4}$$

In this work, a film density of 11.69 g cm^{-3} [200] was taken assuming the film has a composition approaching the formula $IrO_2 \cdot 2H_2O$; n is equal to 2 in this case based on the cyclic voltammograms. The voltammograms suggest the redox process on the electrode surface from Ir (III) to Ir (IV) and then Ir (IV) to Ir (V).

It must be noted that this calculation relies on three main assumptions: 1) the whole charge is due to the IrOx redox states; 2) the whole deposited film is involved in this redox process; 3) the film density is uniform i.e. the film density is homogeneous. The calculation would not be reasonable if any of the assumptions failed.

The anodic and cathodic charges are both shown in Figure 5.6. However, only anodic charge figures were used to calculate the film thickness. Figure 5-6 also presents the film thickness and the charge during cycling deposition against the cycle number.

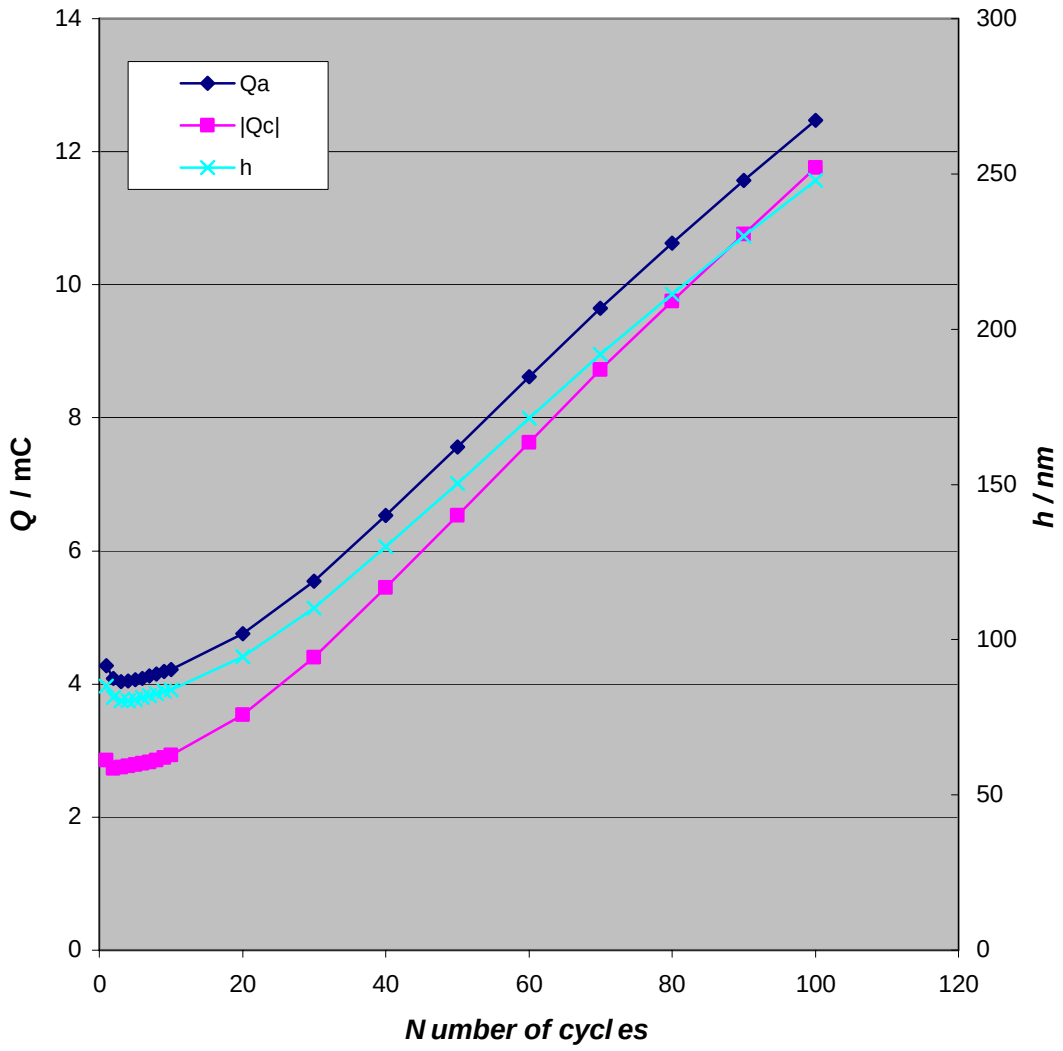

Figure 5-6: Plot showing the dependence of the anodic and cathodic charges / Qa and Q c and of the corresponding theoretical film thickness against the number of the voltammetric cycles used during the deposition of a non structured IrOx film. $Q_a = Q_{A1} + Q_{A2}$, $Q_c = Q_{C1} + Q_{C2}$, *where A1, A2, C1, C2 are the peaks shown in Figure 5.5. The film deposition area is 0.25* cm^2. *Magnitude error of the data points for charge is 0.5 mC.*

After ten voltammetric cycles, the film appears to grow uniformly with a thickness almost linearly related to the number of cycles. Figure 5-6 suggests that a constant amount of IrOx is deposited each time. Moreover, the calculated thickness appears to be

of the same order of magnitude as that seen in Figure 5.1. These observations therefore support the assumptions made above.

5.2.2 Estimation of film thickness with the voltammetric charges for structured IrOx films

Since the SEM estimation of the nanostructured film thickness has a big experimental error, a theoretical estimate of the film thickness is desirable. The calculation of film thickness for non-structured IrOx film follows the approach presented in the previous section. The cyclic voltammogram presented in Figure 5-7 below corresponds to the growth of the IrOx film through a 600 nm diameter polystyrene template.

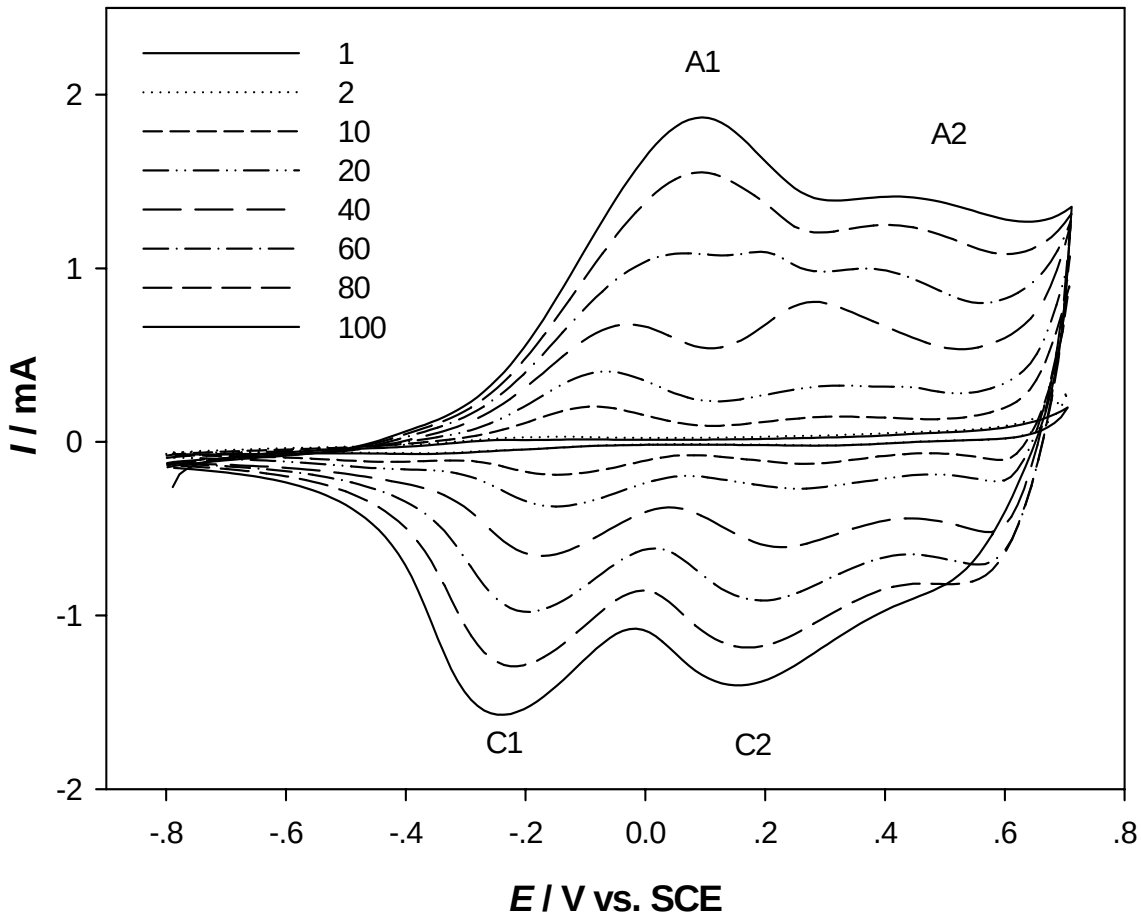

Figure 5-7: Voltammograms for the growth of IrO_x with a 600 nm Ø polystyrene template on a gold electrode from the electrochemical deposition solution (pH = 10). Potential range: -0.8 - 0.7 V, scan rate: 100 mV s^{-1}. The electroactive area is 0.65 cm × 0.35 cm. Number 1, 2, 10…, 100 indicate the voltammetric cycle number.

The potential range for the electrochemical deposition is between -0.8 V and +0.7 V vs. SCE and the scan rate applied was 100 mV s^{-1}. To calculate the film thickness precisely, a defined deposition area was used with a painted insulation solvent. The geometric area of the template coated gold electrode surface is 0.65 cm × 0.35 cm. As observed with the deposition of flat film, the peak heights increase with the voltammetric cycle number when depositing through a polystyrene template. Based on observations made with the

flat films, it is reasonable to expect that the film thickness also increases with cycle numbers.

As described for non structured IrOx films, the charge passed during the deposition of IrOx films for each cycle can be obtained by integrating the peak area using the Autolab programme. The starting and the ending potential can be set up with the Autolab. The first cycle is used as the baseline. The charge against each cycle during deposition is presented in the table below:

Table 5-3: The anodic and cathodic charge applied for different cycles during deposition of structured IrOx films. In this table, $Q\,a = Q_{A1} + Q_{A2,}$ $Q\,c = Q_{C1} + Q_{C2,}$ *where A1, A2, C1, C2 are the peaks shown in Figure 5.7.*

Number of voltammetric cycles	***Qa* / mC**	***Qc* / mC**
1	0.5 ± 0.1	0.8 ± 0.1
10	1.8 ± 0.1	1.9 ± 0.1
20	3.3 ± 0.2	3.4 ± 0.2
30	4.8 ± 0.2	4.9 ± 0.3
40	6.1 ± 0.3	6.3 ± 0.3
50	7.5 ± 0.4	7.7 ± 0.4
60	8.8 ± 0.4	9.1 ± 0.5
70	10.1 ± 0.5	10.4 ± 0.5
80	11.3 ± 0.6	11.7 ± 0.6
90	12.4 ± 0.6	12.7 ± 0.6

The volume of nanostructured film deposited can be calculated with Equation 5-2 as described in the previous section. However, the thickness of the deposited nanostructured IrOx film is different from that of the non-structured film because of the voids. The relationship between the volume deposited and the film thickness is:

$$V = 2\cos(30°)\, r_s^{\,2} h - \pi h^2 (r_s - h/3) \qquad \text{Equation 5-5}$$

This equation is obtained assuming a film with unit volume from which the volume of a sphere is subtracted. r_s is the radius of the polystyrene spheres employed in the templated deposition. In this one unit, the whole volume is $2\cos(30°) r_s^{\,2} h$ and the subtracted volume is the volume of a sphere, which is $\pi h^2 (r_s - h/3)$. Again, it is noted that this calculation relies on three main assumptions: 1) the whole charge is due to the IrOx redox states; 2) the whole deposited film is involved in this redox process; 3) the film density is uniform i.e. the film is homogeneous. Moreover, this calculation is only valid when depositing through a monolayer template. The calculation results are shown in the Table below:

Table 5-4: The structured IrOx film thickness estimated through calculation. h / r_s is the film height divided by the sphere radius.

Number of voltammetric cycles	h / r_s	h / **nm**
1	0	0
10	0.0044	1.32
20	0.053	15.9
30	0.1042	31.26
40	0.1586	47.58
50	0.2201	66.03
60	0.2911	87.33
70	0.3726	111.78
80	0.4689	140.67
90	0.5845	175.35
100	0.7086	212.58

The term h / r_s will be referred as the dimensionless film thickness. It is common to normalise the nanostructured film thickness by the sphere diameter but here, the sphere radius was used instead. In this research, 600 nm diameter spheres have been mostly used. The results have been plotted and are shown in Figure 5-8.

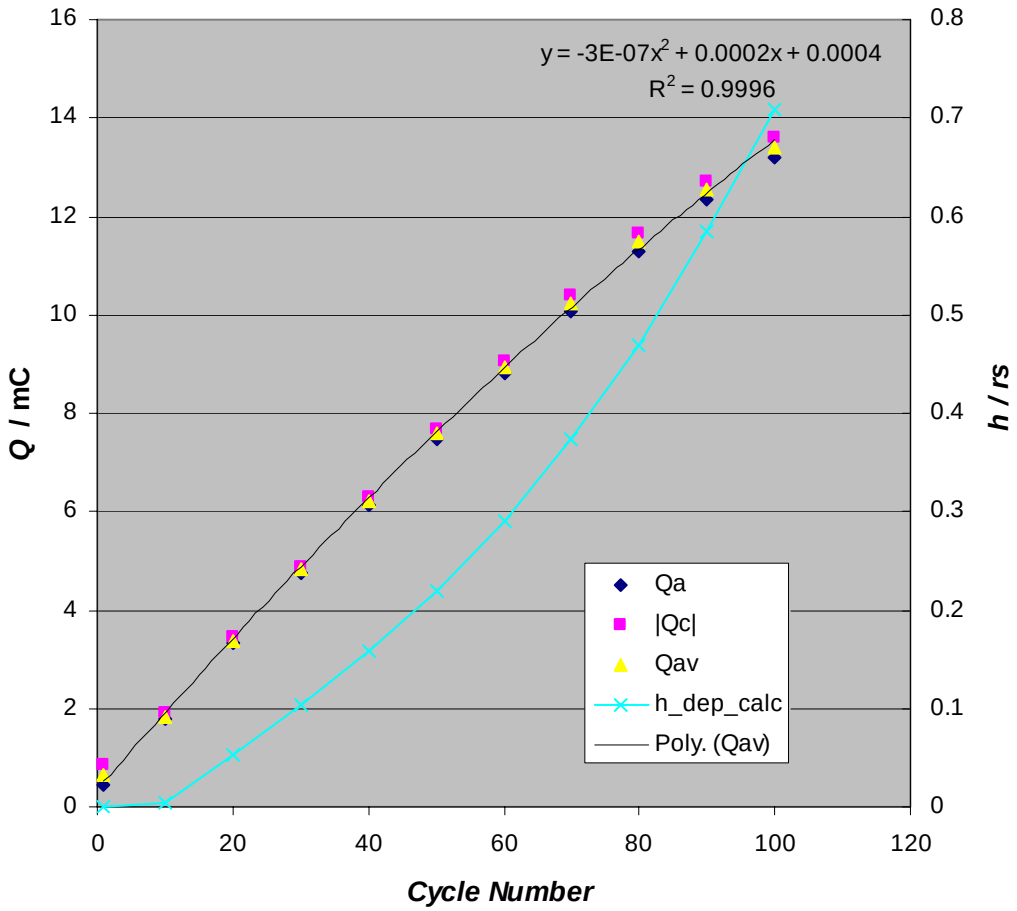

Figure 5-8: Plot showing the dependence of the anodic (Qa) and cathodic charges (Qc)/Qa and Qc and of the corresponding theoretical dimensionless film thickness against the number of the voltammetric cycles used during the deposition of a nanostructured IrOx film.

Figure 5-8 shows that the anodic and cathodic charges (*Qa* and *Qc*) seem to be quite equal. It is very clear that *Qa* and *Qc* increase almost linearly with the voltammetric cycle number at almost the same rate. However, the polynomial fit suggests that the charge may be levelling off after a large number of cycles. The parameter h / r_s was calculated using the equation 5.5.

5.3 Summary

The SEM characterisations of non-structured and nanostructured IrOx films indicate that the film thickness increases with the number of voltammetric cycles. However it is technically difficult to measure the film thickness accurately and the SEM measurements have a large experimental error.

The integration of the voltammograms show a clear, almost linear, relationship between charge and cycle numbers thus indicating that voltammetry provide a fine degree of control over the film thickness. However, theoretical calculations of the film thickness based on the charge passed must be taken with care because they involve severe assumptions about the efficiency of the redox process and the density of the film. The case of templated deposition is more complex because the template effectively means the electroactive area changes periodically with height. This can be calculated and simulated however the experimental voltammograms indicate that the rate of deposition is greater in presence of the spheres (peak currents in Figure 5.7 are greater than in Figure 5.5), thus making any attempt at modelling a lot more challenging.

In conclusion, we estimated the quantitative information between the film thickness and the cycle numbers for both structured and non structured IrOx film. This provides information in order to control the film thickness for future application.

6 Optical properties of nanostructured IrOx films

6.1 The sample of IrOx coated on thickness graded structured gold

The idea of coating a thin layer of IrOx film on a structured gold film was generated in order to make use of the electrochromic property of the iridium oxide. Iridium oxide is known for its electrochromic phenomenon [13, 198, 200, 212]. In recent years, a thorough research of Surface Enhanced Raman Spectroscopy (SERS) on nanostructured metal surface has been undertaken in the Southampton Electrochemistry Group [111, 213] in collaboration with the Physics Department. This SERS feature (described in chapter 1) of nanostructured metal gave great advantages in *in-situ* electrochemical SERS studies and Surface Enhanced Raman Spectroscopy studies of reactive species and intermediates on surfaces. The thin IrOx film coated on a structured gold surface is expected not to destroy the surface plasmon of the gold surface but to work as a switch. By changing the colour of IrOx electrochemically, the IrOx film should absorb the light when the film is in the dark state and allow the light through when it is transparent.

A thickness graded nanostructured gold film was produced with a 600 nm diameter size template. The iridium oxide films used for optical measurements were deposited on one half of a graded gold structured film previously deposited on a gold coated glass substrate. The IrOx film was around 100 nm thick. Figure 6-1 overleaf shows the sample used for optical measurements. The left column of pictures presents the thickness graded nanostructured gold, while the right column of pictures presents the IrOx coated nanostructured gold surface.

Figure 6-1: The sample used for optical measurements. The LHS column of pictures shows the thickness graded nanostructured gold, the RHS column shows the IrOx coated nanostructured gold surface. From top to bottom the thickness is increasing by 6% of the spheres diameter height: 36 nm, 72 nm, 108 nm 144 nm, and 180 nm.

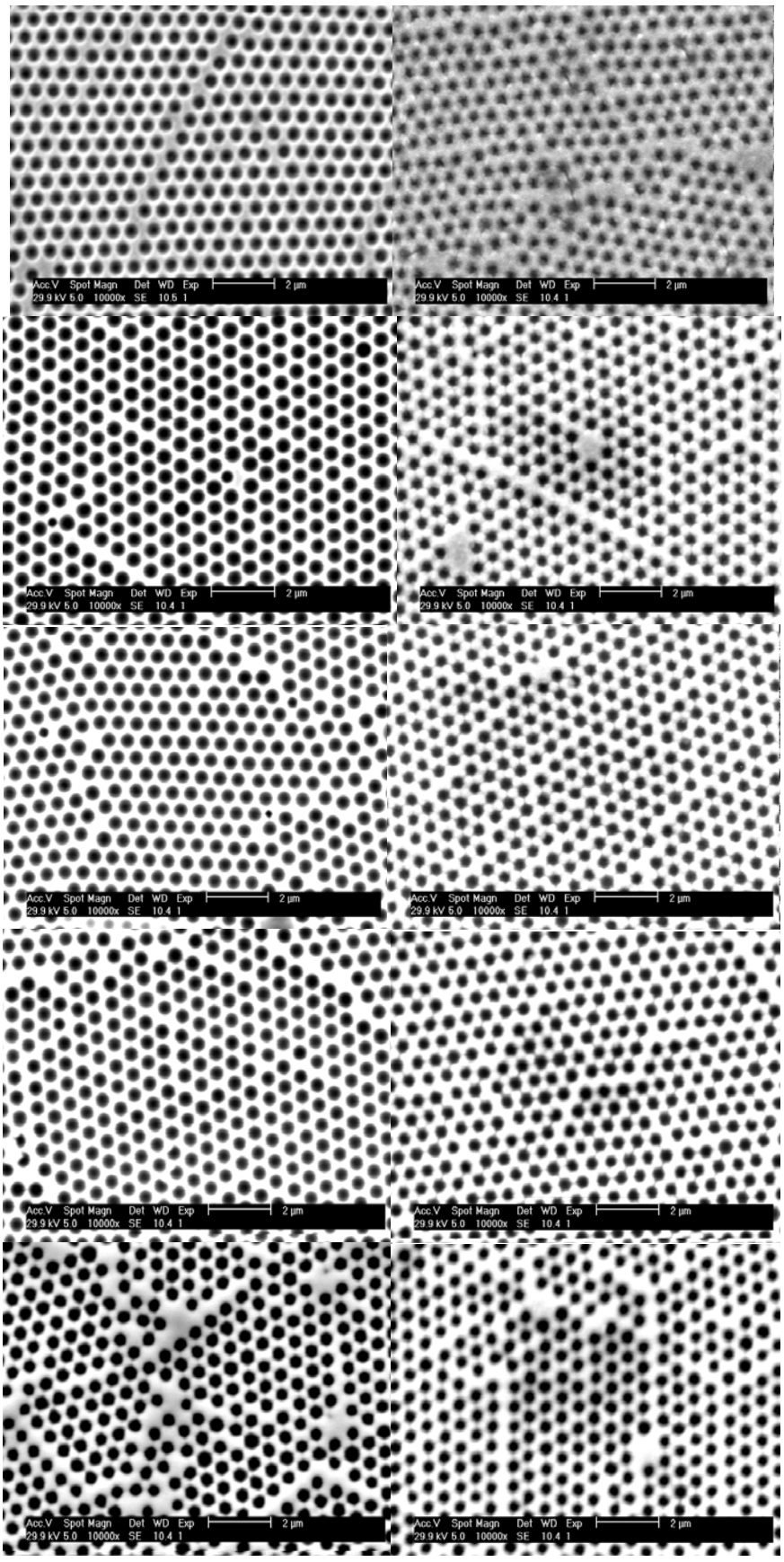
Acc.V Spot Magn Det WD Exp 2 µm
29.9 kV 5.0 10000x SE 10.5 1
Acc.V Spot Magn Det WD Exp 2 µm
29.9 kV 5.0 10000x SE 10.4 1
Acc.V Spot Magn Det WD Exp 2 µm
29.9 kV 5.0 10000x SE 10.4 1
Acc.V Spot Magn Det WD Exp 2 µm
29.9 kV 5.0 10000x SE 10.4 1
Acc.V Spot Magn Det WD Exp 2 µm
29.9 kV 5.0 10000x SE 10.4 1
Acc.V Spot Magn Det WD Exp 2 µm
29.9 kV 5.0 10000x SE 10.4 1
Acc.V Spot Magn Det WD Exp 2 µm
29.9 kV 5.0 10000x SE 10.4 1
Acc.V Spot Magn Det WD Exp 2 µm
29.9 kV 5.0 10000x SE 10.4 1
Acc.V Spot Magn Det WD Exp 2 µm
29.9 kV 5.0 10000x SE 10.4 1
Acc.V Spot Magn Det WD Exp 2 µm
29.9 kV 5.0 10000x SE 10.4 1

For a given thickness, reflectance measurements were made on the structured gold area and on the iridium oxide covered structured gold area. A white light laser source [111] was applied through the electrolyte in an electrochemical cell. The measurements were taken under potential control to drive the electrochromic switching and to record the reflectance spectra for bleached and coloured states. Measurements were then repeated on the parts of the sample made with thicker gold structures. Figure 6-2 shows clearly the area of the structured film with uniform thickness. The sample has been carefully marked and it can be determined that the left side is the gold surface and that the right hand side is the gold coated with IrOx film.

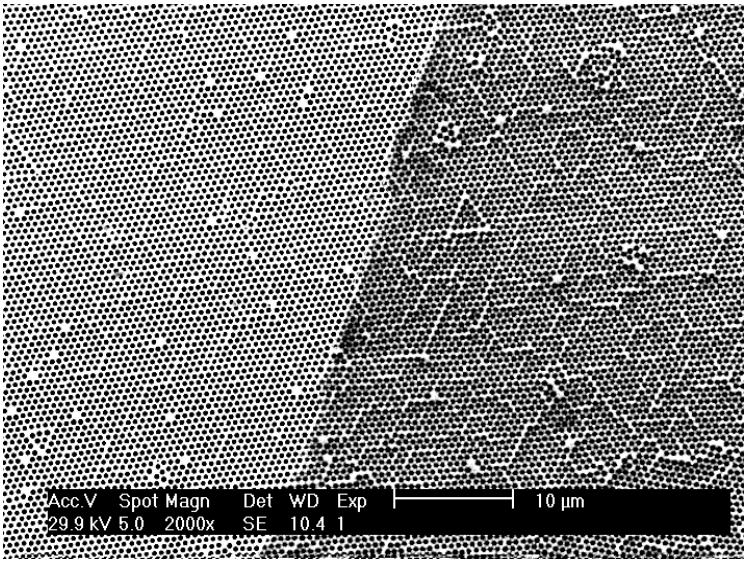

Figure 6-2: SEM micrograph of an iridium oxide film deposited on a structured gold film. Left: structured gold made with a 600 nm diameter template; right, iridium oxide deposited on this structured gold by cyclic voltammetry (~100 cycles). The gold structured film was graded in thickness, but the region shown corresponds to one thickness.

The reflectivity of the sample was measured in an *in-situ* electrochemical cell. The optical measurements were conducted with the sample immersed in the electrolyte and under potential control. By switching the potential, the colour of the IrOx film could be

changed between transparent and dark blue states. Figure 6-3 presents the illustration for the optical measurement of the sample under potential control.

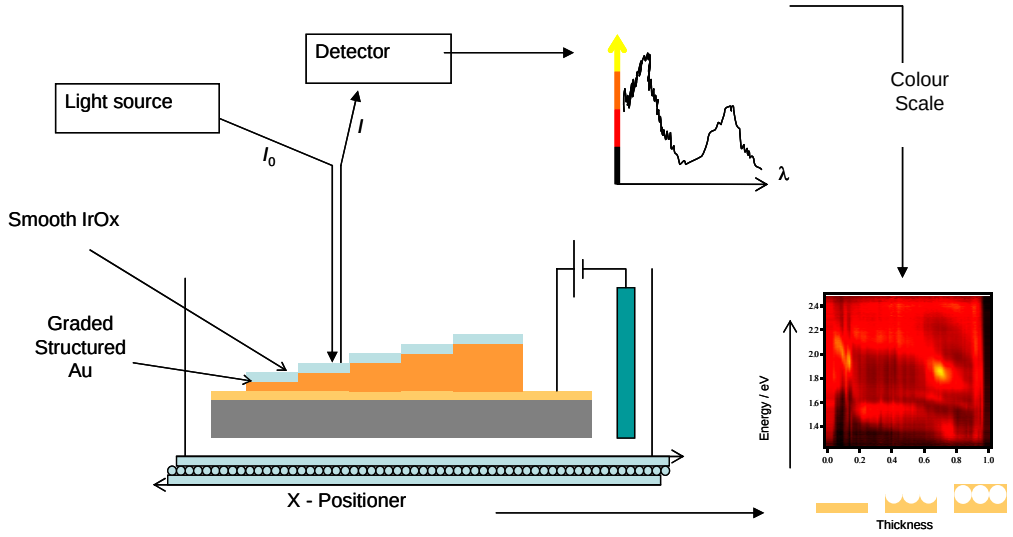

Figure 6-3: Schematic representation of the instruments for in-situ measurement of the optical reflectivity of IrOx coated nanostructured gold sample graded in thickness. This design allows measuring the reflectance of the sample under the potential control. The electrochemical cell was set on an optical bench. A white laser light was directed at normal incidence on the sample and the reflected light was collected by a spectrometer. The potential of the sample was controlled by a potentiostat. The positioner allows moving the sample holder so that the laser light can be focused on the specific part of the sample. The red graph presents a typical optical measurement result. The colour scale indicates the intensity of the substrate absorbance. Further explanation of the graph is given in the text.

Figure 6-4 shows a 2D map of the reflected spectra recorded on a structured gold substrate. The vertical axis shows the energy of the reflected light while the horizontal axis shows the structure thickness normalised by the sphere diameter. The colour scale represents the absorbance normalised by that recorded on a flat gold substrate. The

patterns observed are analysed in terms of surface plasmons. The bright yellow colour indicates strong substrate absorbance of the incident laser light due to intense surface plasmon resonance produced on the cavities surface or inside in the nanostructure.

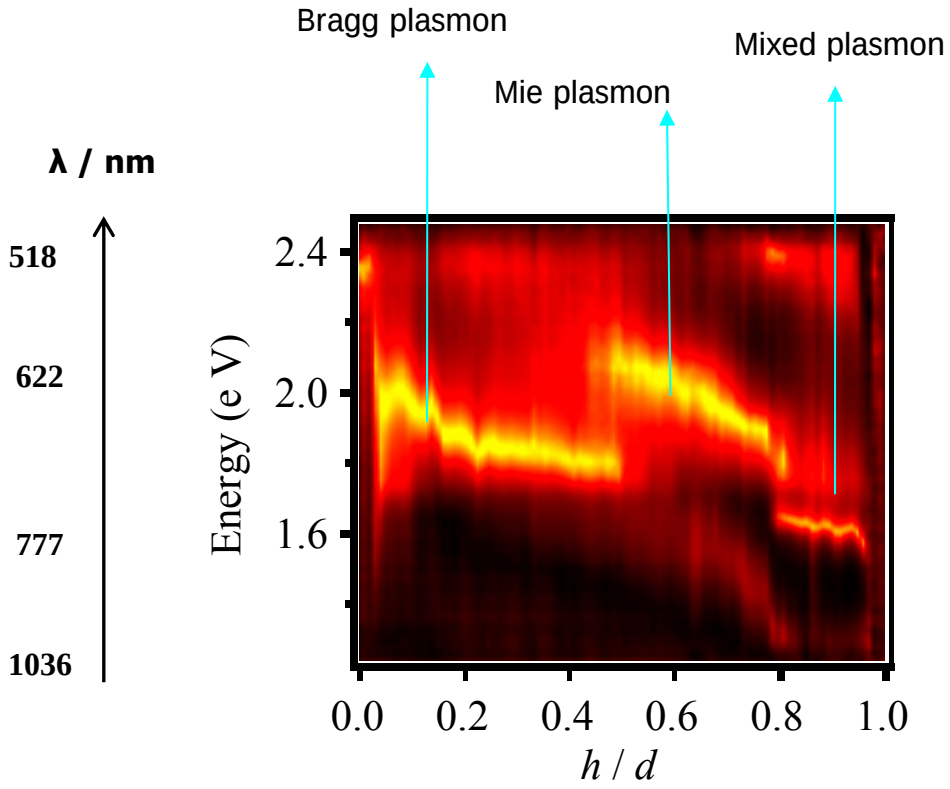

Figure 6-4: 2D map of reflected spectra recorded at normal incidence on a structured gold substrate for different structure thicknesses. The colour scale reflects the absorbance intensity normalised by that of a flat gold substrate (yellow = strong absorbance, black = weak absorbance). The arrows indicate different types of plasmon modes generated on the different film heights.

As discussed in Introduction, three types of surface plasmon modes are observed on nanostructured gold surfaces. The Bragg modes start to disappear just below ½ *d* film height and reappear when the islands reconnect above ¾ *d* film height. When the film structure is between these two heights, Mie modes are observed. As the voids get deeper, the energy of Mie plasmon modes drops.

The reflectance of IrOx coated nanostructured gold substrates was measured and compared with that of the nanostructured gold. By coating a thin layer of IrOx on the nanostructured Au film, the surface plasmon modes of the nanostructured gold surface can be switched on and off by changing the potential. Figure 6-5 below shows the results for the IrOx coated structured Au surface.

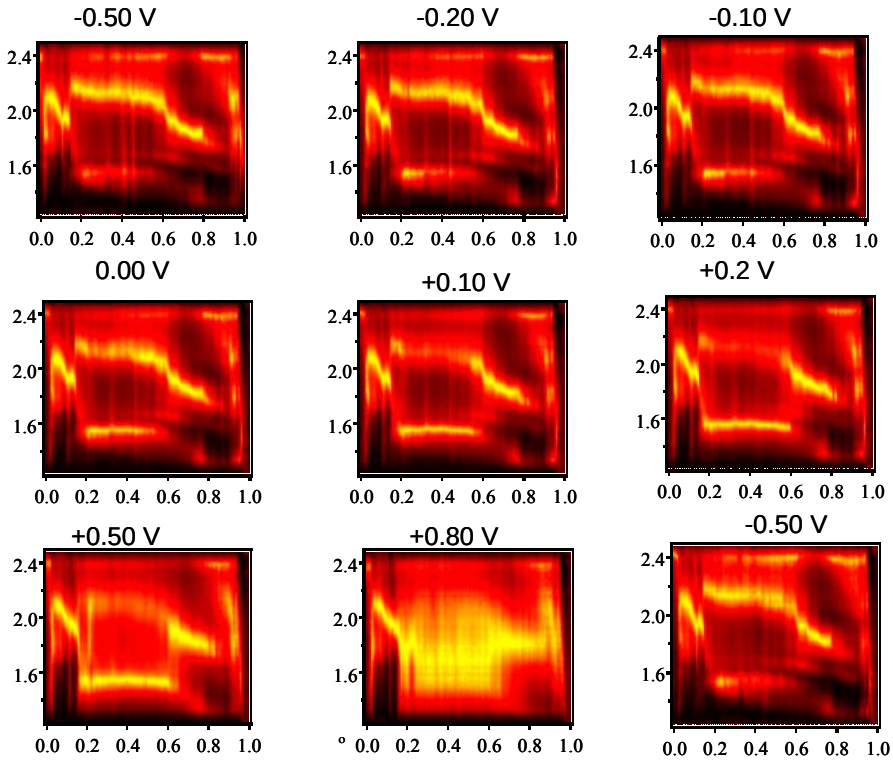

Figure 6-5: Reflectivity spectra showing plots of energy (in eV on vertical axis) vs. normalized thickness (h / d on horizontal axis) recorded while the IrOx coated sample was under potential control between -0.5 V and 0.8 V vs. SCE and then back to -0.5 V. The colour scale reflects the absorbance intensity normalised by that of a flat gold substrate (yellow = strong absorbance, black = weak absorbance).

Figure 6-5 shows that the electrochromic property of the IrOx film can tune the surface plasmon of nanostructured gold. Data were recorded at more potentials however very little changes were seen. Therefore, only these reflectivity spectra with significant

changes are shown in the figure. When the potential was changing from -0.5 to 0.8 V, the IrOx film changed from transparent to dark blue. When the IrOx film is transparent (-0.5 to -0.1 V), the reflectance spectra indicate that the surface plasmon of nanostructured gold was active; while the film changes to dark (0.8V), the IrOx film absorbs the light. So in Figure 6-5, the image at +0.8 V does not show surface absorbance of the incident light and activated surface plasmon. This effect is reversible as shown by the last image at -0.5 V.

The reflectance spectra strongly show that the electrochromic property of the IrOx film can modulate the surface plasmon of structured gold surface. This could be a great advantage of IrOx film as a surface plasmon modulator.

6.2 Studies on the transmittance of nanostructured IrOx film

6.2.1 Influence of the electrolyte pH on film stability

For the electrochromic studies of iridium oxide films, the ageing effects in different electrolytes are quite important since the films are going through ion insertion / extraction processes many times in order to observe the colour changing process. To record the transmittance of the iridium oxide film, transparent ITO substrates are essential for the experiments. Iridium oxide films deposited on gold were found to be very stable while films deposited on ITO were not as stable when cycling in strong acid.

Figure 6-6 shows that the film is quite stable when cycling in base but unstable when cycling in strong acid (pH =1). The arrows in the right voltammograms suggest a gradual loss of material when continuously cycling in acid.

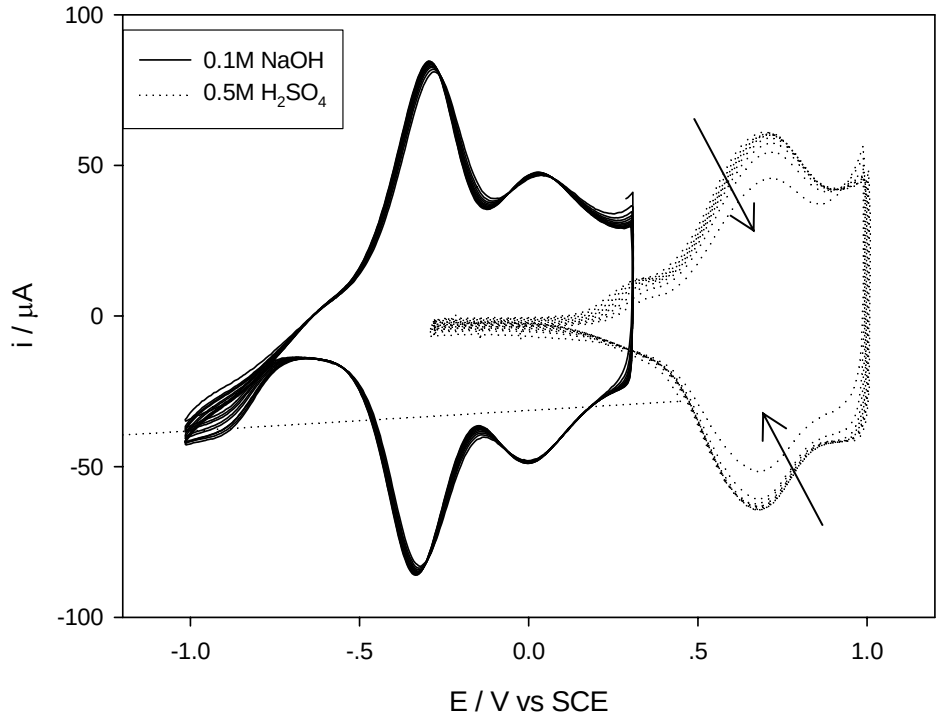

Figure 6-6: Voltammograms showing age effects of iridium oxide films in two electrolytes. Arrows indicate increasing cycle numbers. The film was cycled in 0.1 M NaOH (solid line) and 0.5 M H_2SO_4 (dotted line) for 10 cycles at 10 mV s^{-1} vs. SCE. The films were made with 100 cycles through 400 nm diameter templates on ITO substrates.

The film degradation in acid was observed on the film produced on both ITO and gold substrate. Due to the degradation, transmittance study was mainly carried out in a base solution at this point. However, Yamanaka reported the electrolyte with a pH around 4-5 is the most suitable solution [181].

6.2.2 Modulation of transmittance

Polystyrene spheres of diameters 400, 600 and 800 nm were employed to make templates for fabricating structured iridium oxide films with different cycle numbers. Cycle numbers of 60, 80 and 100 were applied on each template. Meanwhile, flat films of 60,

80 and 100 cycles were fabricated to assess the effect of the nanostructure on the film transmittance. All the samples were monitored in the electrolyte under potential control. Before the transmittances of the films were measured, they were taken out from the electrolyte and held at a potential corresponding to the transparent state. The samples were all dried by clean air.

Figure 6-7 shows that the transmittance of nanostructured films is higher than that of flat films when the films are produced with the same cycle numbers. It also indicates that the transmittance increases as the diameter of spheres increases when the films are made with the same cycle numbers, presumably because bigger spheres leave more of the ITO exposed.

Figure 6-7: Transmittance of iridium oxide films grown with 60 (a), 80 (b) and 100 (c) cycles with flat structure, 400, 600 and 800 nm templated nanostructures. A transparent ITO glass has been used as the reference for 98 % transmittance. The iridium oxide films are in the bleached state.

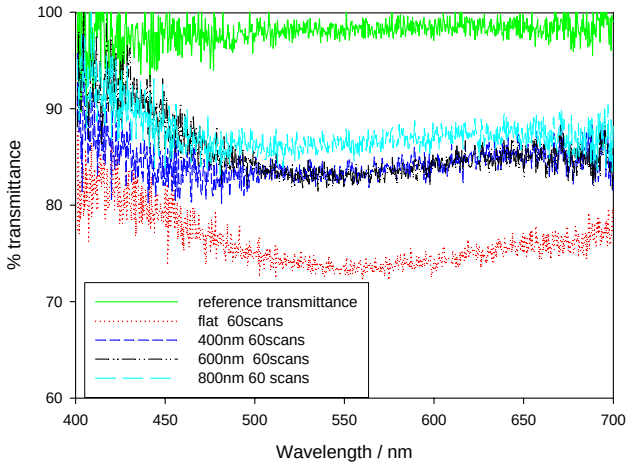
% transmittance
Wavelength / nm
reference transmittance
flat 60scans
400nm 60scans
600nm 60scans
800nm 60 scans

(a)

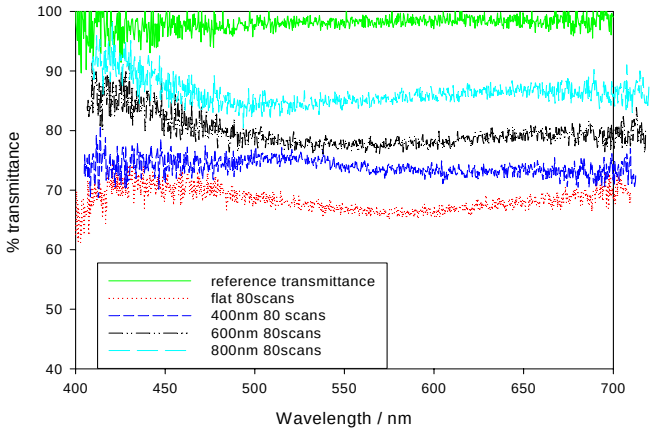
% transmittance
Wavelength / nm
reference transmittance
flat 80scans
400nm 80 scans
600nm 80scans
800nm 80scans

(b)

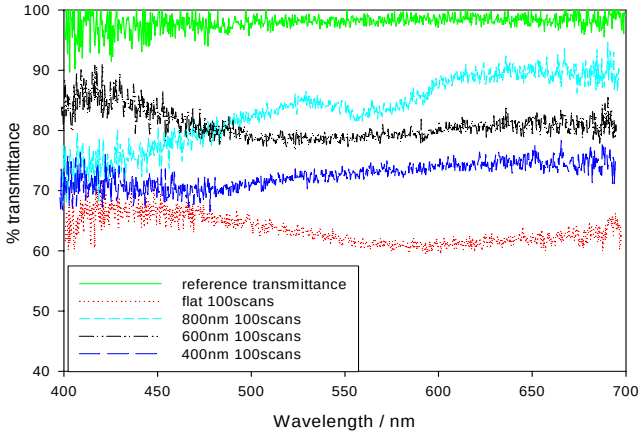
% transmittance
Wavelength / nm
reference transmittance
flat 100scans
800nm 100scans
600nm 100scans
400nm 100scans

(c)

Figure 6-7 clearly shows that the transmittance of the flat films decreases with higher cycle numbers; similarly the transmittance of films made with 400 and 600 nm spheres appear to decrease with higher cycle numbers whereas that of films made with 800 nm spheres does not seem to change significantly; for a given number of cycles and wavelength greater than 450 nm, the transmittance decreases with decreasing sphere diameters. This trend is observed at all cycle numbers although the differences are not so clear with 60 cycles, presumably because the films are too thin.

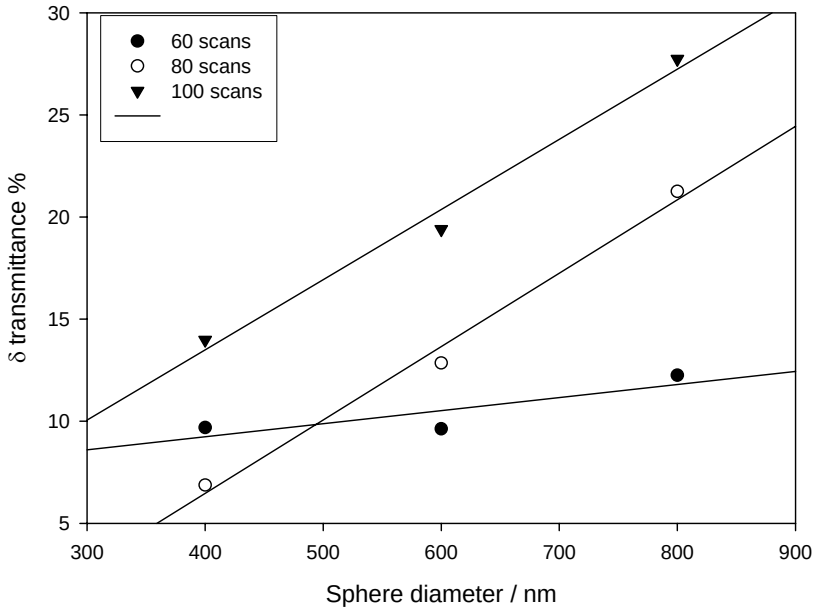

Figure 6-8: The transmittance differences at wavelength of 550 nm between structured and flat films increase with both the scan numbers and the diameters of the nanostructure.

Figure 6-8 presents the effect of the macroporous structure on the transmittance. The values shown in the graph are the differences between the structured and flat films at the same cycle numbers. The graph shows an obvious tendency of increase of transmittance with the diameter of the macroporous structure and with the potential cycle number, thus suggesting that thicker films made with larger pores yield higher transmittance.

Since the SEM pictures show bare areas at the bottom of nanostructured films, the footprint of the spheres, it is possible that these bare areas are the reason for the increase in transmittance.

To address this issue, a set of equations was built up to calculate the increase of transmittance caused by the bare area. Figure 6-9 shows a sketch of the template where one unit cell has been identified.

Since there is one bare area per unit cell, the percentage of surface not covered by the film is given by:

$$\% = 100\ A_h / A_{uc} = 100\ \pi\ r_h^2 / \left(2\sqrt{3} r_s^2\right) \qquad \textit{Equation 6-1}$$

Where r_h, r_s, A_{uc}, A_h are respectively the radius of the holes not coated with IrOx, the radius of the spheres, the area of the unit cell, and the area of one hole.

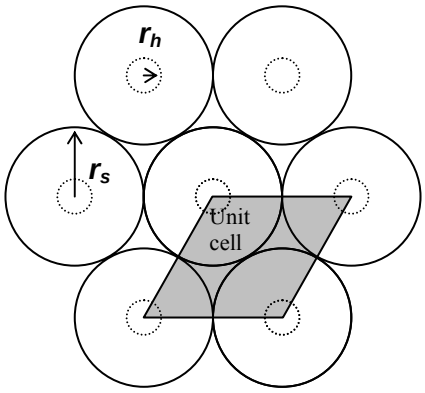

Figure 6-9: Sketch of a nanostructured film; r_h is the radius of the bare area, and r_s is the radius of the spheres. The shaded area shows that there is one bare patch per unit cell.

Real values of r_h and $r_{s,}$ where taken from SEM micrographs of structured IrOx films. In Figure 6-9, a 600 nm diameter templated structured IrOx film has a bare area with a diameter of nearly 300 nm.

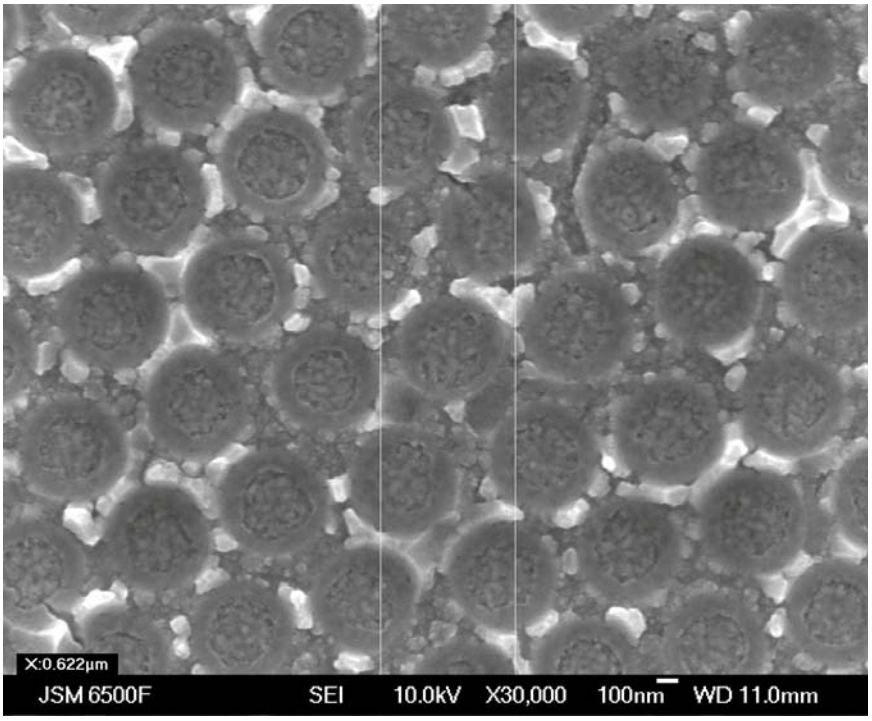

Figure 6-10: FEG SEM micrograph of a structured IrOx film made with a 600 nm diameter template. The holes at the bottom of the cavities are the footprint left by the spheres after their removal [16].

For films made with different templates, we assume that the ratio r_s / r_h is constant. The approximation may not be valid from one substrate to another and may depend on the roughness of the underlying substrate. Using the data from Figure 6-10 we have:

$$r_s / r_h = 300 / 150 \qquad \text{Equation 6-2}$$

Therefore, 400, 600, and 800 nm nanostructured films will have bare patches of 200, 300 and 400 nm diameters according to the equation above.

Taking the 600 nm templated structured films with 80 cycles as an example, the transmittance value is 78.9% at 550 nm wavelength, Figure 6-7 (b). According to Equation 6.1, the percentage of bare area in the structured film is 22.7 % taking r_s = 300 nm and $r_h = 0.5\ r_s$. The flat film at 80 cycles has a transmittance of 66.1%.

The overall film transmittance is assumed to be the sum of the transmittance of bare patches and covered patches, each corrected for their respective fractional areas, Equation 6-3.

$$T_{flat\ IrOx} \times Ø_{IrOx} + T_{ITO} \times Ø_{ITO} = T_{structured\ IrOx} \qquad \textit{Equation 6-3}$$

Where $T_{flat\ IrOx}$ is the transmittance of flat IrOx film on ITO, i.e. 66.1%, $Ø_{IrOx}$ is the coverage of IrOx on the structured film i.e. 1- $Ø_{ITO,}$ T_{ITO} is the transmittance of bare ITO, i.e. 98%, $Ø_{ITO}$ is the coverage of bare ITO, i.e. bare patch 6.1%, $T_{structured\ IrOx}$ is the calculated value of transmittance of the structured IrOx film, hence:

$0.661 \times 77.3\% + 0.227 \times 98\% = 73.3\%$

Comparing the experimental and calculated values, the increase in transmittance due to the structure appears to be 78.9-73.3 % = 5.6 % larger than that expected by transmission through the bare patches. This is probably not significant since the film is likely to have defects and the transmission may vary depending on where the measurement is made. Moreover, the calculation is very crude; transmission through cup shaped IrOx is bound to be different from transmission through a flat IrOx film. A proper calculation should include the dependence of absorbance on film thickness and the fact that the latter increases from the centre to the edges of the cups. The result suggests that the macroporous structure enhanced the transmittance of the film beyond what is estimated to be transmitted through the bare patches. Since the films were rather thin (100 cycles

corresponds to a fraction of a monolayer, see Figure 5.8), these experiments should be repeated with thicker films. However, preparing polystyrene template on the ITO substrate was much more difficult than on Au substrates. Hence, these experiments were not carried out on a thicker nanostructured IrOx film on the ITO substrates.

6.3 Reflectivity of the nanostructured IrOx films: in situ Study

The reflectance of nanostructured IrOx films was measured in order to assess whether, like with Au, the presence of the nanostructure leads to the existence of surface plasmons and whether the electrochromic property of the IrOx film could be used to control the surface plasmons.

According to literature [214], SPR can be observed in any conductor. The study of the surface plasmon on nanostructured IrOx film is a novel idea. In this section, the IrOx film has its own structure deposited on a flat gold surface; this contrasts with the IrOx film deposited on structured gold and discussed in section 6-1. It is well known that a flat non structured Au substrate cannot generate surface plasmon. Therefore, any unusual reflectivity observed in this section will be generated by structured IrOx films.

The nanostructured IrOx films were produced with cyclic voltammetry from the deposition solution. The films were deposited through a 600 nm polystyrene template on a gold surface. The film was graded in thickness as described previously. Figure 6-11 below presents the SEM images of the IrOx film graded in thickness.

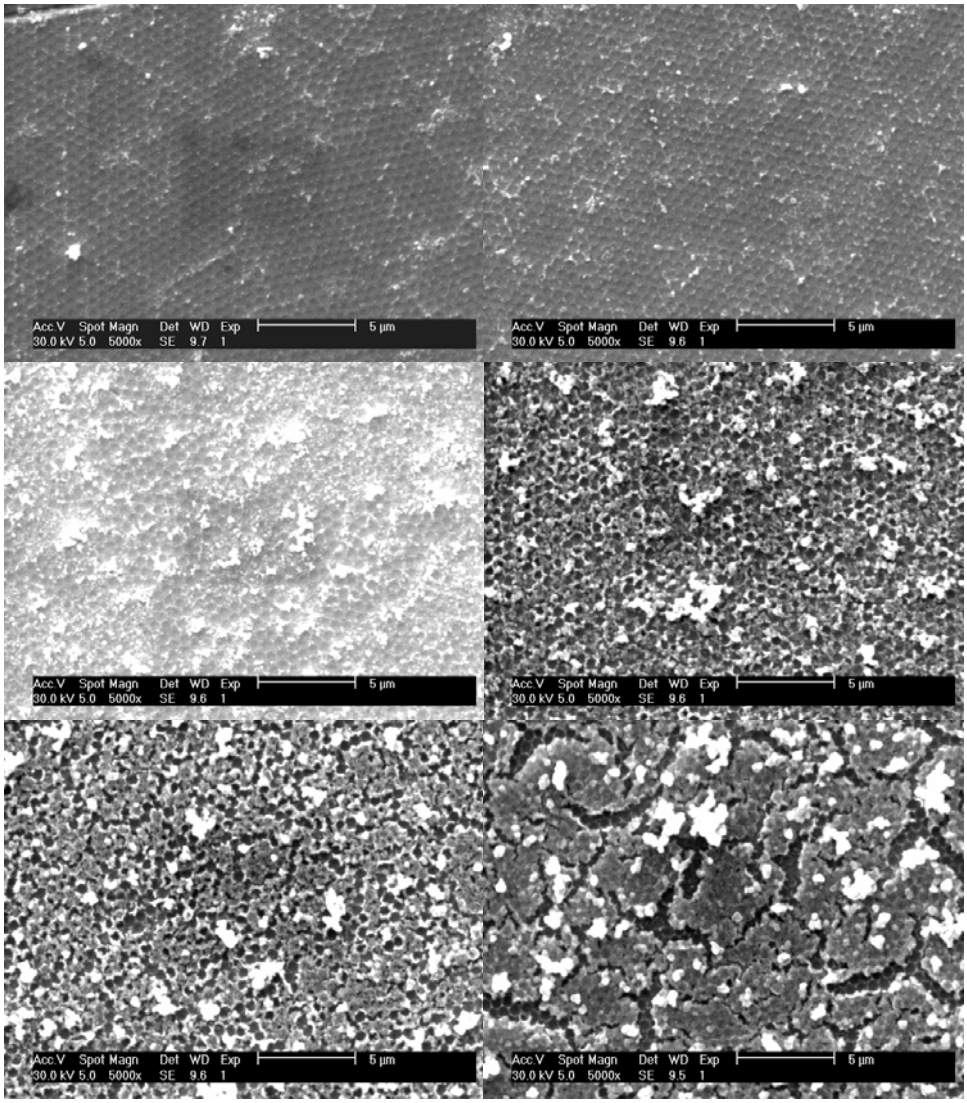

Figure 6-11: Thickness graded monolayer IrOx films produced with a 600 nm diameter polystyrene template by cyclic voltammetry, scan rate 20 mV s^{-1}, potential range -0.8 – 0.7 V, 20 cycles in total, 1 cycle per step.

The thickness graded nanostructured IrOx film was placed in the optical *in situ* design as described in Section 6-1. The electrochemical cell was set on an optical bench. A white laser light was directed at normal incidence on the sample and the reflected light was collected by a spectrometer. The potential of the sample was controlled by a potentiostat. The positioner allows moving the sample holder so that the laser light can be focused on the specific part of the sample. The sample was immersed in the electrolyte to control the

potential electrochemically in order to alter the colour of the film. The reflectance spectra of the film were then measured at a fix potential. Figure 6-12 below presents the reflectance data recorded for the nanostructured IrOx film under potential control.

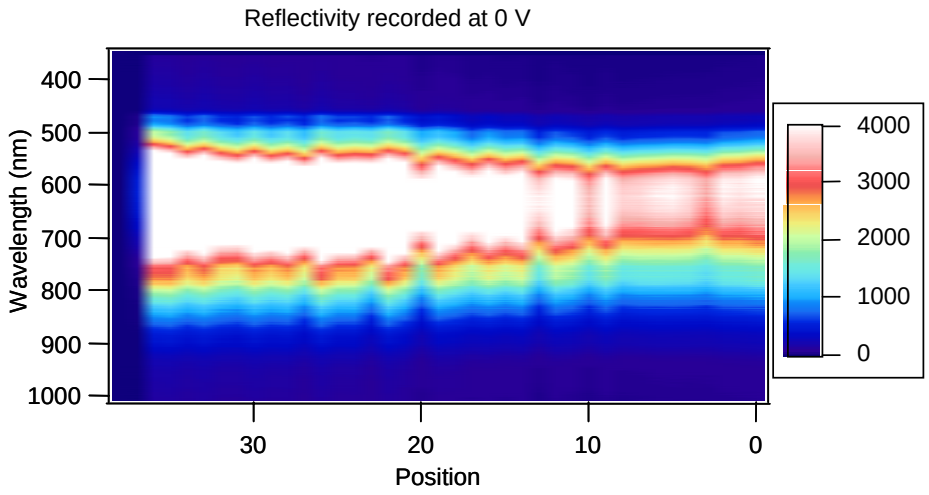

a

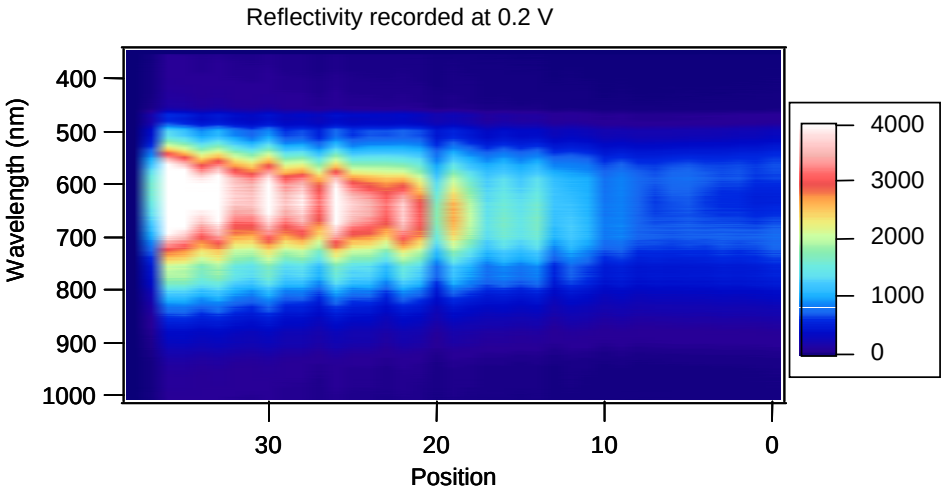

b

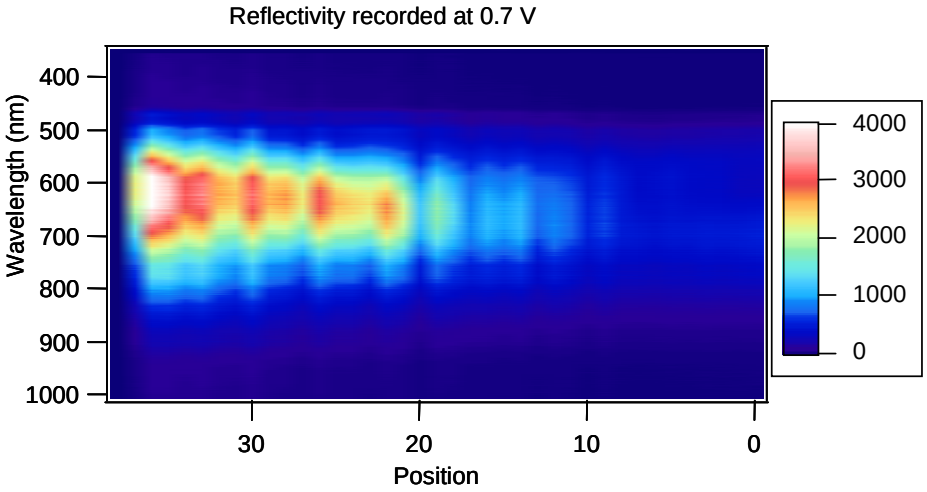

c

Figure 6-12: Reflectance spectra recorded on a structured IrOx film graded in thickness under potentiostatic control in a $(NH_4)_2SO_4$ electrolyte. a) 0 V, b) 0.2 V and c) 0.7 V vs. SCE. The horizontal axis indicates the position where the spectra were recorded with the film thickness increasing from very thin on the left hand side to circa ½ d on the right hand side. The red colour indicates strong substrate reflectance. The unit of the numbers for the colour scale is arbitrary.

When the potential is around 0 V or below, the film is transparent while at 0.7 V and above, the IrOx film is increasingly darker. Figure 6-12 shows the reflectance of IrOx coated on a flat gold substrate is decreasing when the film turns to dark colour from low to high potentials. When the film is in the dark state, it absorbs most of the light and less substrate reflectivity can be observed. The vertical axis shows the wavelength and the colour scale in the figure presents the reflectivity in arbitrary unit. The film has been graded in thickness and Figures 6-12 a, b, c also clearly show that the film reflectivity changes with the film thickness. At the potential 0.7 V, figure 6-12 c, no substrate reflectance can be observed when the film is thick (position around 0); in contrast significant reflectivity can be observed when the film is thin (towards position 30).

6.4 Surface plasmon resonance of the nanostructured IrOx film

The reflectance spectra of a nanostructured IrOx film graded in thickness and measured *in-situ* were reported in Section 6.3. The potential controlled spectra clearly showed the electrochromism of the nanostructured IrOx film. It is also of interest to observe the reflectivity in detail and study the possibility of the surface plasmon coupling on the film surface.

In Section 6.3, the reflectance of IrOx film was affected by the electrolyte. For this reason, in this section, the reflectivity of an IrOx film has been measured under dry conditions to eliminate the interference caused by the electrolyte. The nanostructured IrOx film graded in thickness was taken out of the electrolyte while holding the potential at 0.4 V and then rinsed with water carefully and dried by air. The reflectivity of the sample was measured from different incident angles (often called angle resolved measurement) without potential control. This was realised by turning the sample instead of the incident light with a rotary table sample holder. In order to study the surface plasmon, the reflectance spectra of a flat IrOx film were collected, as shown in Figure 6-13 below. Figure 6-14 below presents the reflectance spectra of a nanostructured IrOx film. The reflectance spectra were taken when the incident light was focused on the film with a thickness around 0.5 sphere diameter.

Compared to the flat IrOx film, the nanostructured IrOx film shows a clean, sharp variation in reflectivity which results from the nanostructure. Based on the work done on Au, it is tempting to analyse these absorbance in terms of delocalised, Bragg plasmons and localised Mie plasmons.

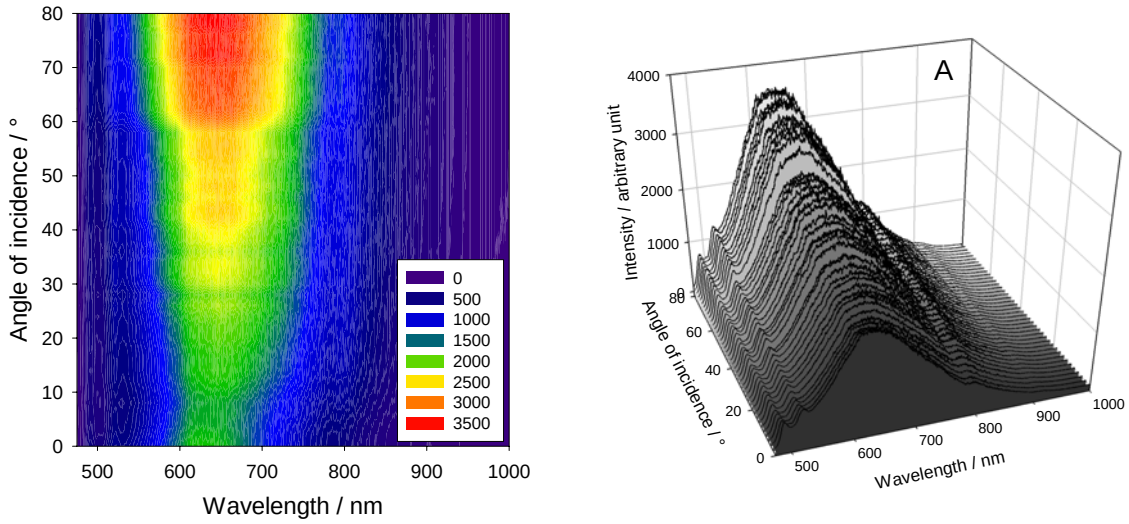

Figure 6-13: Angle resolved reflectivity spectra recorded on a flat IrOx film shown in 2 and 3D. The reflectivity of the film was taken without potential control but with the sample in the dark state. The colour scale is an arbitrary reflectivity scale with the red colour indicating strong reflectivity. 0° normal incidence, 80° grazing incidence.

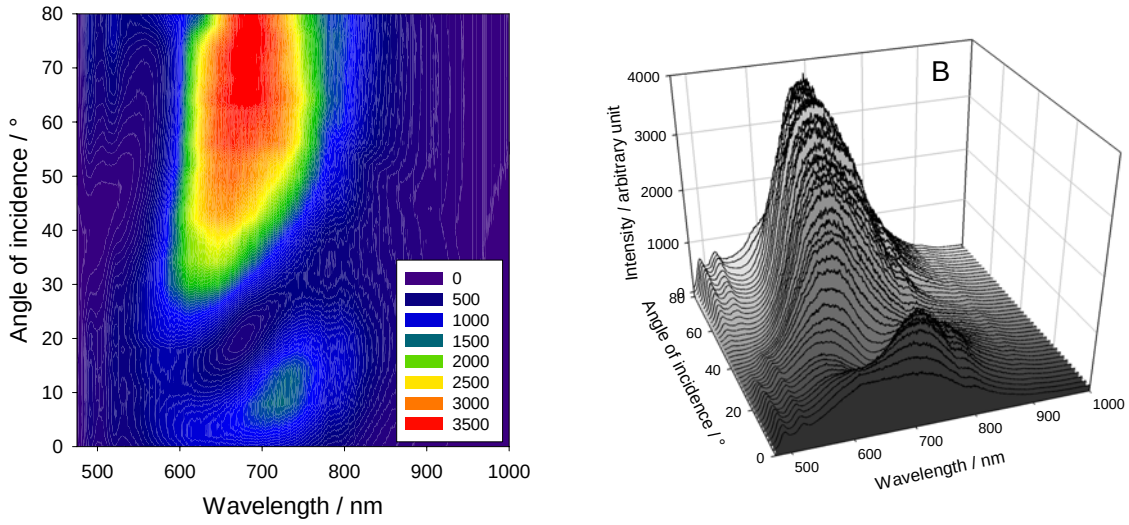

Figure 6-14: Angle resolved reflectivity spectra recorded on a structured IrOx film (½ d thick) shown in 2 and 3D. The reflectivity of the film was taken without potential control but with the sample in the dark state. The colour scale is an arbitrary reflectivity scale with the red colour indicating strong reflectivity. 0° normal incidence, 80° grazing incidence.

Figure 6-15 below shows the image normalised to the reflectivity of an aluminium mirror. These images were acquired, processed and analysed by collaborators at the School of Physics in Southampton and Cambridge. This image clearly demonstrates that the presence of the nanostructure imparts new optical properties to the material. In the case of the flat film, figure 6-15 A, the reflectivity spectrum changes in intensity with angle of incidence but does not change in wavelength or shape. In contrast, figure 6-15 B, for the structured film there is a clear change in the position of the minimum reflectivity with angle. Two plasmon bands are observed in the data, Bragg diffracted by the periodicity of the dishes into the plane of the surface. The dispersion of these modes is governed by the high refractive index IrOx layer and the size of the dishes *d*. Initially coupled at 0° incidence, these modes tune to shorter wavelengths with increasing incident angles, indicative of delocalized behavior. Electrochromism was also observed when reflectivity spectra were recorded under potentiostatic control. For example, the intensity reflected at 770 nm varied from 100% at −0.3 V (the bleached state) to 67% at 0 V, 34% at +0.1 V, 21% at +0.2 V and 16% at +0.7 V (the dark state) [215]. To the best of our knowledge, this is the first attempt of studying surface plasmonic coupling on nanostructured IrOx.

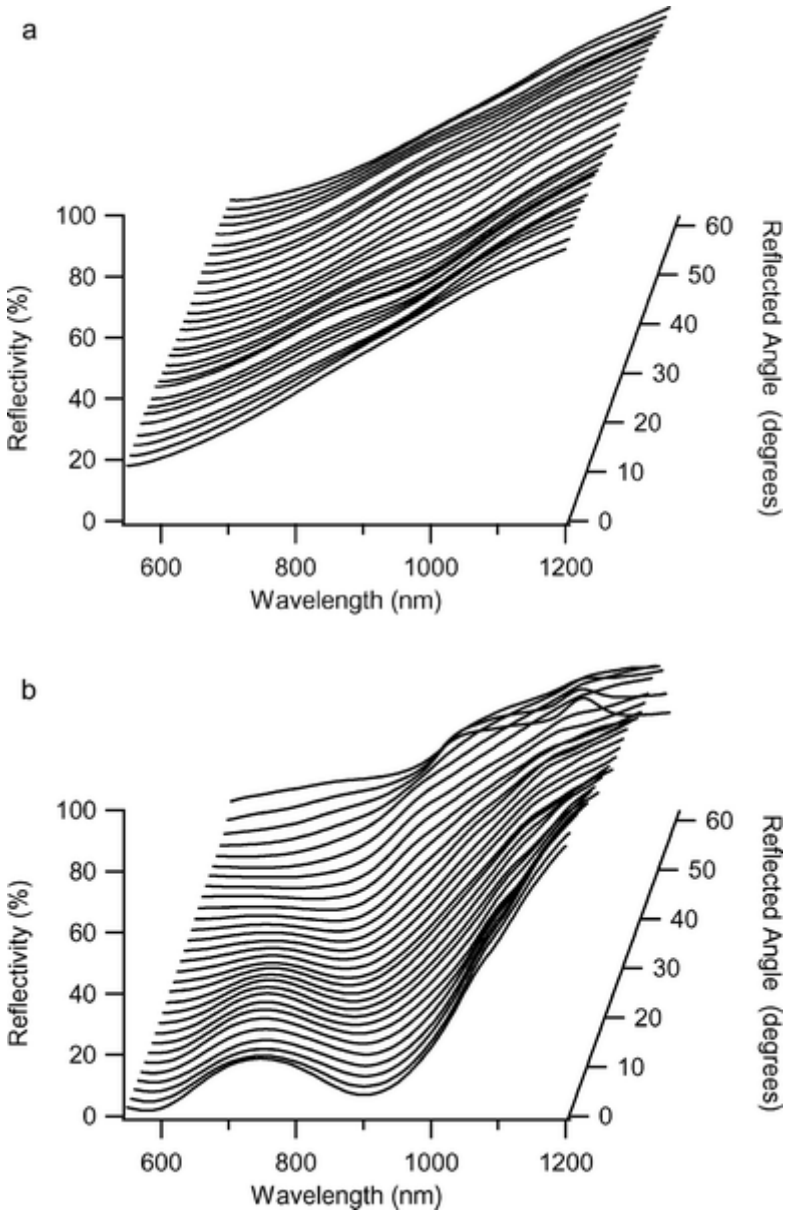

Figure 6-15: Normalized reflectivity spectra recorded on (A) a non-structured film and (B) a structured film supporting plasmon, ~½d, in air [215].

6.5 Summary and conclusion of Chapter Six

In this chapter, the optical properties of IrOx on nanostructured gold surfaces were investigated briefly. The novel idea of coating a thin layer of IrOx on a nanostructured gold surface in order to use the electrochromic property of the IrOx to alter the optical properties of the Au was investigated. The experimental results show clearly that the IrOx

film can work as a modulator of the surface plasmons of the nanostructured gold surface. By changing the potential of the electrochemical cell, the colour of IrOx film can be changed, thus, it can be used to switch on and off of the surface plasmon of the underlying Au film.

The optical properties of nanostructured IrOx films were presented in this chapter. The transmittance of a nanostructured IrOx film was measured with a transparent substrate. Compared to a non-structured film, it is found that the nanostructure increases the transmittance but only by a very small amount and the results are still inconclusive.

The reflectance of thickness-graded nanostructured IrOx films was measured. The electrochromic property of nanostructured IrOx was studied by *in situ* measurements. The reflectance of nanostructured IrOx films was found to contain sharp absorbance not seen with the flat IrOx films.

7 Conclusion and future work

This work has mainly focused on the electrochemical deposition of IrOx films with and without nanostructure by cyclic voltammetry. The deposition solution was produced according to Yamanaka's recipe. Nanostructured IrOx films were deposited with 400 nm, 500 nm, 600 nm, 800, 900 nm and 1.6 μm diameter polystyrene templates for the first time. In addition, different substrates have been used to deposit IrOx films, namely glassy carbon, Pt, Au and ITO. Only Au and ITO substrates were successfully used to obtain nanostructured films.

Electrochemically deposited nanostructured IrOx films present a uniform hexagonal structure. However, nanostructured IrOx films encounter a cracking problem when growing the film beyond ½ *d* (the template sphere diameter). Different dissolving solvents and heat treatments were tested. Cyclohexane was found the most gentle dissolving solvent for the polystyrene sphere, but at the expense of speed, in contrast DMF was mostly used to remove the sphere because of its very rapid action, 5 min as opposed to several days with cyclohexane. With the assistance of cyclohexane, multilayered nanostructured IrOx films can be obtained when applying a multilayer template. Multilayered nanostructured IrOx films show a well organized 3D honey-comb structure.

The thicknesses of both the structured and non structured films were found to increase with the number of voltammetric cycles. A systematic study of the relationship of the film thickness with the cycle number was carried out. Three different methods were suggested to estimate the film thickness, including: SEM estimation, theoretical calculation according to the charge during cyclic voltammetry and the geometric calculation when the film is very thin. Those calculation approaches were found effective under different circumstances.

IrOx films have a wide range of applications, one of which is the excellent electrochromic property. Nanostructured IrOx film was deposited on a structured Au film

to work as a surface plasmon modulator. By changing the colour of the IrOx film through potential control, the Au surface plasmon can be switched on and off. The transmittance of nanostructured IrOx films was studied and compared to that of non structured films. However, a very small effect was observed. Nanostructured thickness graded IrOx films were deposited on flat Au substrates to observe the electrochromic effect. The different film thicknesses show different absorption intensity. The electrochromic effect of a nanostructured IrOx film was studied while the sample was immersed in the electrolyte under potential control.

In this work, surface plasmon resonance on the nanostructured IrOx film was studied for the first time. Compared to the flat IrOx film, the nanostructured IrOx film reflectivity shows clean, sharp absorbance which results from the nanostructure. The reflectivity spectra of nanostructured IrOx films show similar phenomenon as observed on Au where these effects were analysed in terms of surface plasmons. However, the refractive index of IrOx is probably not the same as the refractive index of that of Au. The analysis of the optical properties of nanostructured IrOx films is on going and developing.

The IrOx film structure can be studied further to obtain a better control of film thickness. A variety of substrates for deposition of IrOx film can be looked into. The original objective to make a pH detector with nanostructured IrOx was left aside in order to concentrate on the optical properties of the new material. Therefore, further applications of IrOx film can be studied, such as pH sensing, catalysts and bio-analysis. Typical in the case of bio-analysis, nanostructured IrOx can work as many cavities to trap the cells.

All in all, nanostructured IrOx films with great application potential have been successfully fabricated and studied in this work. Although the chemistry of different metal oxide varies, this work suggests there is a chance of extending this approach to fabricate other oxides.

8 References

[1] Vanhoudt, P.; Lewandowski, Z.; Little, B., Iridium Oxide Ph Microelectrode, *Biotechnology and Bioengineering* **1992**, *40*, 601.

[2] Midgley, D., A Review of Ph Measurement at High-Temperatures, *Talanta* **1990**, *37*, 767.

[3] Kim, J. Y.; Lee, Y. H., Pd-Pdo Ph Microprobe for Local Ph Measurement, *Biotechnology and Bioengineering* **1989**, *34*, 131.

[4] Hitchman, M. L.; Ramanathan, S., Evaluation of Iridium Oxide Electrodes Formed by Potential Cycling as Ph Probes, *Analyst* **1988**, *113*, 35.

[5] Kinoshita, E.; Ingman, F.; Edwall, G.; Thulin, S.; Glab, S., Polycrystalline and Monocrystalline Antimony, Iridium and Palladium as Electrode Material for Ph-Sensing Electrodes, *Talanta* **1986**, *33*, 125.

[6] Burke, L. D.; Mulcahy, J. K.; Whelan, D. P., Preparation of an Oxidized Iridium Electrode and the Variation of Its Potential with Ph, *J. Electroanal. Chem.* **1984**, *163*, 117.

[7] Wipf, D. O.; Ge, F. Y.; Spaine, T. W.; Bauer, J. E., Microscopic measurement of pH with iridium oxide microelectrodes, *Anal. Chem.* **2000**, *72*, 4921.

[8] Runnels, P. L.; Joseph, J. D.; Logman, M. J.; Wightman, R. M., Effect of pH and surface functionalities on the cyclic voltammetric responses of carbon-fiber microelectrodes, *Anal. Chem.* **1999**, *71*, 2782.

[9] Guthrie, A. J.; Narayanaswamy, R.; Russell, D. A., Application of Kubelka - Munk Diffuse Reflectance Theory to Optical Fiber Sensors, *Analyst* **1988**, *113*, 457.

[10] Kirkbright, G. F.; Miller, R. M.; Spillane, D. E. M.; Vickery, I. P., Impulse-Response Photoacoustic-Spectroscopy of Biological Samples, *Analyst* **1984**, *109*, 1443.

[11] Fog, A.; Buck, R. P., Electronic Semiconducting Oxides as Ph Sensors, *Sensors and Actuators* **1984**, *5*, 137.

[12] Beebe, X.; Rose, T. L., Charge Injection Limits of Activated Iridium Oxide Electrodes with 0.2ms Pulses in Bicarbonate Buffered Saline, *Ieee Transactions on Biomedical Engineering* **1988**, *35*, 494.

[13] Schiavone, L. M.; Dautremontsmith, W. C.; Beni, G.; Shay, J. L., Electrochromic Iridium Oxide-Films Prepared by Reactive Sputtering, *Applied Physics Letters* **1979**, *35*, 823.

[14] Bezbaruah, A. N.; Zhang, T. C., Fabrication of anodically electrodeposited iridium oxide film pH microelectrodes for microenvironmental studies, *Anal. Chem.* **2002**, *74*, 5726.

[15] Marzouk, S. A. M.; Ufer, S.; Buck, R. P.; Johnson, T. A.; Dunlap, L. A.; Cascio, W. E., Electrodeposited iridium oxide pH electrode for measurement of extracellular myocardial acidosis during acute ischemia, *Anal. Chem.* **1998**, *70*, 5054.

[16] Jiang, J.; Kucernak, A., Nanostructured platinum as an electrocatalyst for the electrooxidation of formic acid, *J. Electroanal. Chem.* **2002**, *520*, 64.

[17] Raghuveer, V.; Manthiram, A., Mesoporous carbon with larger pore diameter as an electrocatalyst support for methanol oxidation, *Electrochemical and Solid State Letters* **2004**, *7*, A336.
[18] Han, J. H.; Boo, H.; Park, S.; Chung, T. D., Electrochemical oxidation of hydrogen peroxide at nanoporous platinum electrodes and the application to glutamate microsensor, *Electrochim. Acta* **2006**, *52*, 1788.
[19] Imokawa, T.; Williams, K. J.; Denuault, G., Fabrication and characterization of nanostructured Pd hydride pH microelectrodes, *Anal. Chem.* **2006**, *78*, 265.
[20] Sosna, M.; Denuault, G.; Pascal, R. W.; Prien, R. D.; Mowlem, M., Development of a reliable microelectrode dissolved oxygen sensor, *Sens. Actuator B-Chem.* **2007**, *123*, 344.
[21] Mahajan, S.; Abdelsalam, M.; Suguwara, Y.; Cintra, S.; Russell, A.; Baumberg, J.; Bartlett, P., Tuning plasmons on nano-structured substrates for NIR-SERS, *Phys. Chem. Chem. Phys.* **2007**, *9*, 104.
[22] Broglin, B. L.; Andreu, A.; Dhussa, N.; Heath, J. A.; Gerst, J.; Dudley, B.; Holland, D.; El-Kouedi, M., Investigation of the effects of the local environment on the surface-enhanced Raman spectra of striped gold/silver nanorod arrays, *Langmuir* **2007**, *23*, 4563.
[23] Seelig, E. W.; Tang, B.; Yamilov, A.; Cao, H.; Chang, R. P. H., Self-assembled 3D photonic crystals from ZnO colloidal spheres, *Materials Chemistry and Physics* **2003**, *80*, 257.
[24] Scharrer, M.; Yamilov, A.; Wu, X. H.; Cao, H.; Chang, R. P. H., Ultraviolet lasing in high-order bands of three-dimensional ZnO photonic crystals, *Applied Physics Letters* **2006**, *88*.
[25] Birudavolu, S.; Nuntawong, N.; Balakrishnan, G.; Xin, Y. C.; Huang, S.; Lee, S. C.; Brueck, S. R. J.; Hains, C. P.; Huffaker, D. L., Selective area growth of InAs quantum dots formed on a patterned GaAs substrate, *Applied Physics Letters* **2004**, *85*, 2337.
[26] Collings, P. J., *Liquid Crystals: Natures Delicate Phase of Matter* **1990**, *Princeton University Press, Princeton*.
[27] Collings, P. J.; Hird, M., *Itroduction to Liquid Crystals* **1997**, *Taylor and Francis, London*.
[28] Attard, G. S.; Glyde, J. C.; Goltner, C. G., Liquid-Crystalline Phases as Templates for the Synthesis of Mesoporous Silica, *Nature* **1995**, *378*, 366.
[29] Attard, G. S.; Bartlett, P. N.; Coleman, N. R. B.; Elliott, J. M.; Owen, J. R.; Wang, J. H., Mesoporous platinum films from lyotropic liquid crystalline phases, *Science* **1997**, *278*, 838.
[30] Elliott, J. M.; Attard, G. S.; Bartlett, P. N.; Coleman, N. R. B.; Merckel, D. A. S.; Owen, J. R., Nanostructured platinum (HI-ePt) films. Effects of electrodeposition conditions on film properties, *Chem. Mater.* **1999**, *11*, 3602.
[31] Bartlett, P. N.; Birkin, P. N.; Ghanem, M. A.; de Groot, P.; Sawicki, M., The electrochemical deposition of nanostructured cobalt films from lyotropic liquid crystalline media, *J. Electrochem. Soc.* **2001**, *148*, C119.
[32] Attard, G. S.; Leclerc, S. A. A.; Maniguet, S.; Russell, A. E.; Nandhakumar, I.; Bartlett, P. N., Mesoporous Pt/Ru alloy from the hexagonal lyotropic liquid crystalline phase of a nonionic surfactant, *Chem. Mat.* **2001**, *13*, 1444.

[33] Nelson, P. A.; Elliott, J. M.; Attard, G. S.; Owen, J. R., Mesoporous nickel/nickel oxide - a nanoarchitectured electrode, *Chem. Mat.* **2002**, *14*, 524.
[34] Nelson, P. A.; Elliott, J. M.; Attard, G. S.; Owen, J. R., Mesoporous nickel/nickel oxide electrodes for high power applications, *J. New Mat.Electrochem. Syst.* **2002**, *5*, 63.
[35] Denuault, G.; Milhano, C.; Pletcher, D., Mesoporous palladium - the surface electrochemistry of palladium in aqueous sodium hydroxide and the cathodic reduction of nitrite, *Phys. Chem. Chem. Phys.* **2005**, *7*, 3545.
[36] Nandhakumar, I.; Elliott, J. M.; Attard, G. S., Electrodeposition of nanostructured mesoporous selenium films (H-I-eSe), *Chem. Mat.* **2001**, *13*, 3840.
[37] Cook, D. A., *PhD Thesis, Department of Chemistry, University of Southampton* **2005**.
[38] Jiang, P.; Cizeron, J.; Bertone, J. F.; Colvin, V. L., Preparation of macroporous metal films from colloidal crystals, *J. Am. Chem. Soc.* **1999**, *121*, 7957.
[39] Velev, O. D.; Tessier, P. M.; Lenhoff, A. M.; Kaler, E. W., Materials - A class of porous metallic nanostructures, *Nature* **1999**, *401*, 548.
[40] Holland, B. T.; Blanford, C. F.; Do, T.; Stein, A., Synthesis of highly ordered, three-dimensional, macroporous structures of amorphous or crystalline inorganic oxides, phosphates, and hybrid composites, *Chem. Mat.* **1999**, *11*, 795.
[41] Holland, B. T.; Blanford, C. F.; Stein, A., Synthesis of macroporous minerals with highly ordered three- dimensional arrays of spheroidal voids, *Science* **1998**, *281*, 538.
[42] Zakhidov, A. A.; Baughman, R. H.; Iqbal, Z.; Cui, C. X.; Khayrullin, I.; Dantas, S. O.; Marti, I.; Ralchenko, V. G., Carbon structures with three-dimensional periodicity at optical wavelengths, *Science* **1998**, *282*, 897.
[43] Braun, P. V.; Wiltzius, P., Microporous materials - Electrochemically grown photonic crystals, *Nature* **1999**, *402*, 603.
[44] Holland, B. T.; Abrams, L.; Stein, A., Dual templating of macroporous silicates with zeolitic microporous frameworks, *J. Am. Chem. Soc.* **1999**, *121*, 4308.
[45] Velev, O. D.; Jede, T. A.; Lobo, R. F.; Lenhoff, A. M., Porous silica via colloidal crystallization, *Nature* **1997**, *389*, 447.
[46] Velev, O. D.; Jede, T. A.; Lobo, R. F.; Lenhoff, A. M., Microstructured porous silica obtained via colloidal crystal templates, *Chem. Mat.* **1998**, *10*, 3597.
[47] Johnson, S. A.; Ollivier, P. J.; Mallouk, T. E., Ordered mesoporous polymers of tunable pore size from colloidal silica templates, *Science* **1999**, *283*, 963.
[48] Park, S. H.; Xia, Y. N., Macroporous membranes with highly ordered and three-dimensionally interconnected spherical pores, *Advanced Materials* **1998**, *10*, 1045.
[49] Park, S. H.; Xia, Y. N., Fabrication of three-dimensional macroporous membranes with assemblies of microspheres as templates, *Chem. Mat.* **1998**, *10*, 1745.
[50] Darragh, P. J.; Gaskin, A. J.; Sanders, J. V., Opals, *Scientific American* **1976**, *234*, 84.
[51] Matijevic, E., Preparation and Properties of Uniform Size Colloids, *Chem. Mat.* **1993**, *5*, 412.
[52] Stober, W.; Fink, A.; Bohn, E., Controlled growth of monodisperse silica spheres in the micron size range, *J. Colloid Interface Sci.* **1968**, *26*, 62.

[53] Xia, Y. N.; Gates, B.; Yin, Y. D.; Lu, Y., Monodispersed colloidal spheres: Old materials with new applications, *Advanced Materials* **2000**, *12*, 693.
[54] Skjeltorp, A. T.; Meakin, P., Fracture in Microsphere Monolayers Studied by Experiment and Computer-Simulation, *Nature* **1988**, *335*, 424.
[55] Bardosova, M.; Tredgold, R. H., Ordered layers of monodispersive colloids, *J. Mater. Chem.* **2002**, *12*, 2835.
[56] Murray, C. A.; Vanwinkle, D. H., Experimental-Observation of 2-Stage Melting in a Classical Two-Dimensional Screened Coulomb System, *Phys. Rev. Lett.* **1987**, *58*, 1200.
[57] Denkov, N. D.; Velev, O. D.; Kralchevsky, P. A.; Ivanov, I. B.; Yoshimura, H.; Nagayama, K., 2-Dimensional Crystallization, *Nature* **1993**, *361*, 26.
[58] Picard, G., Fine particle monolayers made by a mobile dynamic thin laminar flow (DTLF) device, *Langmuir* **1998**, *14*, 3710.
[59] Hurd, A. J.; Schaefer, D. W., Diffusion-Limited Aggregation in 2 Dimensions, *Phys. Rev. Lett.* **1985**, *54*, 1043.
[60] Wickman, H. H.; Korley, J. N., Colloid crystal self-organization and dynamics at the air/water interface, *Nature* **1998**, *393*, 445.
[61] Denkov, N. D.; Velev, O. D.; Kralchevsky, P. A.; Ivanov, I. B.; Yoshimura, H.; Nagayama, K., Mechanism of Formation of 2-Dimensional Crystals from Latex-Particles on Substrates, *Langmuir* **1992**, *8*, 3183.
[62] Dimitrov, A. S.; Nagayama, K., Continuous convective assembling of fine particles into two- dimensional arrays on solid surfaces, *Langmuir* **1996**, *12*, 1303.
[63] Dimitrov, A. S.; Miwa, T.; Nagayama, K., A comparison between the optical properties of amorphous and crystalline monolayers of silica particles, *Langmuir* **1999**, *15*, 5257.
[64] Trau, M.; Saville, D. A.; Aksay, I. A., Assembly of colloidal crystals at electrode interfaces, *Langmuir* **1997**, *13*, 6375.
[65] Trau, M.; Saville, D. A.; Aksay, I. A., Field-induced layering of colloidal crystals, *Science* **1996**, *272*, 706.
[66] Solomentsev, Y.; Bohmer, M.; Anderson, J. L., Particle clustering and pattern formation during electrophoretic deposition: A hydrodynamic model, *Langmuir* **1997**, *13*, 6058.
[67] Yeh, S. R.; Seul, M.; Shraiman, B. I., Assembly of ordered colloidal aggregates by electric-field-induced fluid flow, *Nature* **1997**, *386*, 57.
[68] Davis, K. E.; Russel, W. B.; Glantschnig, W. J., Settling Suspensions of Colloidal Silica - Observations and X-Ray Measurements, *Journal of the Chemical Society-Faraday Transactions* **1991**, *87*, 411.
[69] Miguez, H.; Meseguer, F.; Lopez, C.; Blanco, A.; Moya, J. S.; Requena, J.; Mifsud, A.; Fornes, V., Control of the photonic crystal properties of fcc-packed submicrometer SiO2 spheres by sintering, *Advanced Materials* **1998**, *10*, 480.
[70] Mayoral, R.; Requena, J.; Moya, J. S.; Lopez, C.; Cintas, A.; Miguez, H.; Meseguer, F.; Vazquez, L.; Holgado, M.; Blanco, A., 3D long-range ordering in an SiO2 submicrometer-sphere sintered superstructure, *Advanced Materials* **1997**, *9*, 257.
[71] Pieranski, P., Colloidal Crystals, *Contemporary Physics* **1983**, *24*, 25.

[72] Neser, S.; Bechinger, C.; Leiderer, P.; Palberg, T., Finite-size effects on the closest packing of hard spheres, *Phys. Rev. Lett.* **1997**, *79*, 2348.
[73] Pieranski, P.; Strzelecki, L.; Pansu, B., Thin Colloidal Crystals, *Phys. Rev. Lett.* **1983**, *50*, 900.
[74] Davis, K. E.; Russel, W. B.; Glantschnig, W. J., Disorder-to-Order Transition in Settling Suspensions of Colloidal Silica - X-Ray Measurements, *Science* **1989**, *245*, 507.
[75] Pusey, P. N.; Vanmegen, W., Phase-Behavior of Concentrated Suspensions of Nearly Hard Colloidal Spheres, *Nature* **1986**, *320*, 340.
[76] Dosho, S.; Ise, N.; Ito, K.; Iwai, S.; Kitano, H.; Matsuoka, H.; Nakamura, H.; Okumura, H.; Ono, T.; Sogami, I. S.; Ueno, Y.; Yoshida, H.; Yoshiyama, T., Recent Study of Polymer Latex Dispersions, *Langmuir* **1993**, *9*, 394.
[77] Park, S. H.; Xia, Y. N., Assembly of mesoscale particles over large areas and its application in fabricating tunable optical filters, *Langmuir* **1999**, *15*, 266.
[78] Gates, B.; Qin, D.; Xia, Y. N., Assembly of nanoparticles into opaline structures over large areas, *Advanced Materials* **1999**, *11*, 466.
[79] Gates, B.; Yin, Y. D.; Xia, Y. N., Fabrication and characterization of porous membranes with highly ordered three-dimensional periodic structures, *Chem. Mat.* **1999**, *11*, 2827.
[80] Bartlett, P. N.; Birkin, P. R.; Ghanem, M. A.; Toh, C. S., Electrochemical syntheses of highly ordered macroporous conducting polymers grown around self-assembled colloidal templates, *J. Mater. Chem.* **2001**, *11*, 849.
[81] Bartlett, P. N.; Birkin, P. R.; Ghanem, M. A., Electrochemical deposition of macroporous platinum, palladium and cobalt films using polystyrene latex sphere templates, *Chem. Commun.* **2000**, 1671.
[82] Bartlett, P. N.; Baumberg, J. J.; Birkin, P. R.; Ghanem, M. A.; Netti, M. C., Highly ordered macroporous gold and platinum films formed by electrochemical deposition through templates assembled from submicron diameter monodisperse polystyrene spheres, *Chem. Mat.* **2002**, *14*, 2199.
[83] Lellig, C.; Hartl, W.; Wagner, J.; Hempelmann, R., Immobilized highly charged colloidal crystals: A new route to three-dimensional mesoscale structured materials, *Angewandte Chemie-International Edition* **2002**, *41*, 102.
[84] Luo, G.; Liu, Z. J.; Li, L.; Xie, S. H.; Kong, J. L.; Zhao, D. Y., Creating highly ordered metal, alloy, and semiconductor macrostructures by electrodeposition, ion spraying, and laser spraying, *Advanced Materials* **2001**, *13*, 286.
[85] Sumida, T.; Wada, Y.; Kitamura, T.; Yanagida, S., Macroporous ZnO films electrochemically prepared by templating of opal films, *Chemistry Letters* **2001**, 38.
[86] Sumida, T.; Wada, Y.; Kitamura, T.; Yanagida, S., Construction of stacked opaline films and electrochemical deposition of ordered macroporous nickel, *Langmuir* **2002**, *18*, 3886.
[87] Sumida, T.; Wada, Y.; Kitamura, T.; Yanagida, S., Electrochemical preparation of macroporous polypyrrole films with regular arrays of interconnected spherical voids, *Chem. Commun.* **2000**, 1613.

[88] van Vugt, L. K.; van Driel, A. F.; Tjerkstra, R. W.; Bechger, L.; Vos, W. L.; Vanmaekelbergh, D.; Kelly, J. J., Macroporous germanium by electrochemical deposition, *Chem. Commun.* **2002**, 2054.
[89] Yan, H. W.; Blanford, C. F.; Holland, B. T.; Parent, M.; Smyrl, W. H.; Stein, A., A chemical synthesis of periodic macroporous NiO and metallic Ni, *Advanced Materials* **1999**, *11*, 1003.
[90] Subramanian, G.; Manoharan, V. N.; Thorne, J. D.; Pine, D. J., Ordered macroporous materials by colloidal assembly: A possible route to photonic bandgap materials, *Advanced Materials* **1999**, *11*, 1261.
[91] Subramania, G.; Constant, K.; Biswas, R.; Sigalas, M. M.; Ho, K. M., Optical photonic crystals fabricated from colloidal systems, *Applied Physics Letters* **1999**, *74*, 3933.
[92] Yang, P. D.; Deng, T.; Zhao, D. Y.; Feng, P. Y.; Pine, D.; Chmelka, B. F.; Whitesides, G. M.; Stucky, G. D., Hierarchically ordered oxides, *Science* **1998**, *282*, 2244.
[93] Yin, J. S.; Wang, Z. L., Template-assisted self-assembly and cobalt doping of ordered mesoporous titania nanostructures, *Advanced Materials* **1999**, *11*, 469.
[94] Bertone, J. F.; Jiang, P.; Hwang, K. S.; Mittleman, D. M.; Colvin, V. L., Thickness dependence of the optical properties of ordered silica-air and air-polymer photonic crystals, *Phys. Rev. Lett.* **1999**, *83*, 300.
[95] Yoshino, K.; Lee, S. B.; Tatsuhara, S.; Kawagishi, Y.; Ozaki, M.; Zakhidov, A. A., Observation of inhibited spontaneous emission and stimulated emission of rhodamine 6G in polymer replica of synthetic opal, *Applied Physics Letters* **1998**, *73*, 3506.
[96] Vlasov, Y. A.; Yao, N.; Norris, D. J., Synthesis of photonic crystals for optical wavelengths from semiconductor quantum dots, *Advanced Materials* **1999**, *11*, 165.
[97] Imhof, A.; Pine, D. J., Uniform macroporous ceramics and plastics by emulsion templating, *Advanced Materials* **1998**, *10*, 697.
[98] Imhof, A.; Pine, D. J., Ordered macroporous materials by emulsion templating, *Nature* **1997**, *389*, 948.
[99] Bartlett, P. N.; Dunford, T.; Ghanem, M. A., Templated electrochemical deposition of nanostructured macroporous PbO2, *J. Mater. Chem.* **2002**, *12*, 3130.
[100] Barnes, W. L.; Dereux, A.; Ebbesen, T. W., Surface plasmon subwavelength optics, *Nature* **2003**, *424*, 824.
[101] Barnes, W. L.; Preist, T. W.; Kitson, S. C.; Sambles, J. R., Physical origin of photonic energy gaps in the propagation of surface plasmons on gratings, *Phys. Rev. B* **1996**, *54*, 6227.
[102] Ebbesen, T. W.; Lezec, H. J.; Ghaemi, H. F.; Thio, T.; Wolff, P. A., Extraordinary optical transmission through sub-wavelength hole arrays, *Nature* **1998**, *391*, 667.
[103] Vukusic, P.; Hooper, I., Directionally controlled fluorescence emission in butterflies, *Science* **2005**, *310*, 1151.
[104] Kitson, S. C.; Barnes, W. L.; Sambles, J. R., Full photonic band gap for surface modes in the visible, *Phys. Rev. Lett.* **1996**, *77*, 2670.

[105] Kneipp, K.; Wang, Y.; Kneipp, H.; Perelman, L. T.; Itzkan, I.; Dasari, R.; Feld, M. S., Single molecule detection using surface-enhanced Raman scattering (SERS), *Phys. Rev. Lett.* **1997**, *78*, 1667.
[106] Nie, S. M.; Emery, S. R., Probing single molecules and single nanoparticles by surface-enhanced Raman scattering, *Science* **1997**, *275*, 1102.
[107] Kelf, T. A.; Sugawara, Y.; Baumberg, J. J.; Abdelsalam, M.; Bartlett, P. N., Plasmonic band gaps and trapped plasmons on nanostructured metal surfaces, *Phys. Rev. Lett.* **2005**, *95*.
[108] Satpathy, S.; Zhang, Z.; Salehpour, M. R., Theory of Photon Bands in 3-Dimensional Periodic Dielectric Structures, *Phys. Rev. Lett.* **1990**, *64*, 1239.
[109] Coyle, S.; Netti, M. C.; Baumberg, J. J.; Ghanem, M. A.; Birkin, P. R.; Bartlett, P. N.; Whittaker, D. M., Confined plasmons in metallic nanocavities - art. no. 176801, *Phys. Rev. Lett.* **2001**, *8717*, 6801.
[110] Teperik, T. V.; Popov, V. V.; de Abajo, F. J. G., Void plasmons and total absorption of light in nanoporous metallic films, *Phys. Rev. B* **2005**, *71*.
[111] Abdelsalam, M. E.; Bartlett, P. N.; Baumberg, J. J.; Cintra, S.; Kelf, T. A.; Russell, A. E., Electrochemical SERS at a structured gold surface, *Electrochem. Commun.* **2005**, *7*, 740.
[112] Kuai, S. L.; Bader, G.; Ashrit, P. V., Tunable electrochromic photonic crystals, *Applied Physics Letters* **2005**, *86*.
[113] Yablonovitch, E., Inhibited Spontaneous Emission in Solid-State Physics and Electronics, *Phys. Rev. Lett.* **1987**, *58*, 2059.
[114] Joannopoulos, J. D., *Photonic Crystals*, 1995.
[115] Thijssen, M. S.; Sprik, R.; Wijnhoven, J.; Megens, M.; Narayanan, T.; Lagendijk, A.; Vos, W. L., Inhibited light propagation and broadband reflection in photonic air-sphere crystals, *Phys. Rev. Lett.* **1999**, *83*, 2730.
[116] Vos, W. L.; Sprik, R.; vanBlaaderen, A.; Imhof, A.; Lagendijk, A.; Wegdam, G. H., Strong effects of photonic band structures on the diffraction of colloidal crystals, *Phys. Rev. B* **1996**, *53*, 16231.
[117] Vukusic, P.; Sambles, J. R., Photonic structures in biology, *Nature* **2003**, *424*, 852.
[118] Prasad, P. N., *Nanophotonics*, 2004.
[119] http://www.icmm.csic.es/cefe/pbgs.htm.
[120] Gruning, U.; Lehmann, V.; Ottow, S.; Busch, K., Macroporous silicon with a complete two-dimensional photonic band gap centered at 5 mu m, *Applied Physics Letters* **1996**, *68*, 747.
[121] Krauss, T. F.; DeLaRue, R. M.; Brand, S., Two-dimensional photonic-bandgap structures operating at near infrared wavelengths, *Nature* **1996**, *383*, 699.
[122] Fukuda, K.; Sun, H.; Matsuo, S.; Misawa, H., Self-organizing three-dimensional colloidal photonic crystal structure with augmented dielectric contrast, *Japanese Journal of Applied Physics Part 2-Letters* **1998**, *37*, L508.
[123] Mei, D. B.; Liu, H. G.; Cheng, B. Y.; Li, Z. L.; Zhang, D. Z.; Dong, P., Visible and near-infrared silica colloidal crystals and photonic gaps, *Phys. Rev. B* **1998**, *58*, 35.
[124] Yamasaki, T.; Tsutsui, T., Spontaneous emission from fluorescent molecules embedded in photonic crystals consisting of polystyrene microspheres, *Applied Physics Letters* **1998**, *72*, 1957.

[125] Miguez, H.; Lopez, C.; Meseguer, F.; Blanco, A.; Vazquez, L.; Mayoral, R.; Ocana, M.; Fornes, V.; Mifsud, A., Photonic crystal properties of packed submicrometric SiO2 spheres, *Applied Physics Letters* **1997**, *71*, 1148.
[126] Romanov, S. G.; Johnson, N. P.; Fokin, A. V.; Butko, V. Y.; Yates, H. M.; Pemble, M. E.; Torres, C. M. S., Enhancement of the photonic gap of opal-based three-dimensional gratings, *Applied Physics Letters* **1997**, *70*, 2091.
[127] Tarhan, II; Watson, G. H., Photonic band structure of fcc colloidal crystals, *Phys. Rev. Lett.* **1996**, *76*, 315.
[128] Lopez, C.; Vazquez, L.; Meseguer, F.; Mayoral, R.; Ocana, M.; Miguez, H., Photonic crystal made by close packing SiO2 submicron spheres, *Superlattices and Microstructures* **1997**, *22*, 399.
[129] Gates, B.; Park, S. H.; Xia, Y. N., Tuning the photonic bandgap properties of crystalline arrays of polystyrene beads by annealing at elevated temperatures, *Advanced Materials* **2000**, *12*, 653.
[130] Busch, K.; John, S., Photonic band gap formation in certain self-organizing systems, *Phys. Rev. E* **1998**, *58*, 3896.
[131] Doosje, M.; Hoenders, B. J.; Knoester, J., Photonic bandgap optimization in inverted fcc photonic crystals, *Journal of the Optical Society of America B-Optical Physics* **2000**, *17*, 600.
[132] Kulinowski, K. M.; Jiang, P.; Vaswani, H.; Colvin, V. L., Porous metals from colloidal templates, *Advanced Materials* **2000**, *12*, 833.
[133] Weston, J. L.; Butera, A.; Otte, D.; Barnard, J. A., Nanostructured magnetic networks: a materials comparison, *Journal of Magnetism and Magnetic Materials* **1999**, *193*, 515.
[134] Yamilov, A.; Wu, X.; Cao, H., Photonic band structure of ZnO photonic crystal slab laser, *J. Appl. Phys.* **2005**, *98*.
[135] Scharrer, M.; Wu, X.; Yamilov, A.; Cao, H.; Chang, R. P. H., Fabrication of inverted opal ZnO photonic crystals by atomic layer deposition, *Applied Physics Letters* **2005**, *86*.
[136] Aliev, A. E.; Lee, S. B.; Baughman, R. H.; Zakhldov, A. A., Thermal properties of carbon inverse opal photonic crystals, *Journal of Luminescence* **2007**, *125*, 11.
[137] Zakhidov, A. A.; Khayrullin, II; Baughman, R. H.; Iqbal, Z.; Yoshino, K.; Kawagishi, Y.; Tatsuhara, S., CVD synthesis of carbon-based metallic photonic crystals, *Nanostructured Materials* **1999**, *12*, 1089.
[138] Kempa, K.; Kimball, B.; Rybczynski, J.; Huang, Z. P.; Wu, P. F.; Steeves, D.; Sennett, M.; Giersig, M.; Rao, D.; Carnahan, D. L.; Wang, D. Z.; Lao, J. Y.; Li, W. Z.; Ren, Z. F., Photonic crystals based on periodic arrays of aligned carbon nanotubes, *Nano Letters* **2003**, *3*, 13.
[139] Choi, C. G.; Han, Y. T.; Kim, J. T.; Schift, H., Air-suspended two-dimensional polymer photonic crystal slab waveguides fabricated by nanoimprint lithography, *Applied Physics Letters* **2007**, *90*.
[140] Chen, J. Q.; Jiang, W.; Chen, X. N.; Wang, L.; Zhang, S. S.; Chen, R. T., Holographic three-dimensional polymeric photonic crystals operating in the 1550 nm window, *Applied Physics Letters* **2007**, *90*.

[141] Blanco, A.; Lopez, C.; Mayoral, R.; Miguez, H.; Meseguer, F.; Mifsud, A.; Herrero, J., CdS photoluminescence inhibition by a photonic structure, *Applied Physics Letters* **1998**, *73*, 1781.
[142] Miguez, H.; Meseguer, F.; Lopez, C.; Mifsud, A.; Moya, J. S.; Vazquez, L., Evidence of FCC crystallization of SiO2 nanospheres, *Langmuir* **1997**, *13*, 6009.
[143] Marzouk, S. A. M., Improved electrodeposited iridium oxide pH sensor fabricated on etched titanium substrates, *Anal. Chem.* **2003**, *75*, 1258.
[144] Izutsu, K.; Yamamoto, H., Response of an iridium oxide pH-sensor in nonaqueous solutions. Comparison with other pH-sensors, *Analytical Sciences* **1996**, *12*, 905.
[145] Kinlen, P. J.; Heider, J. E.; Hubbard, D. E., A Solid-State Ph Sensor-Based on a Nafion-Coated Iridium Oxide Indicator Electrode and a Polymer-Based Silver-Chloride Reference Electrode, *Sens. Actuator B-Chem.* **1994**, *22*, 13.
[146] Pasztor, K.; Sekiguchi, A.; Shimo, N.; Kitamura, N.; Masuhara, H., Iridium Oxide-Based Microelectrochemical Transistors for Ph Sensing, *Sensors and Actuators B-Chemical* **1993**, *12*, 225.
[147] Joseph, J.; Kim, H. O. L.; Oh, S. J., Insitu Electrochemical Sensor for Measurement in Nonconductive Liquids, *J. Electrochem. Soc.* **1993**, *140*, L33.
[148] Olthuis, W.; Bomer, J. G.; Bergveld, P.; Bos, M.; Vanderlinden, W. E., Iridium Oxide as Actuator Material for the Isfet-Based Sensor Actuator System, *Sens. Actuator B-Chem.* **1991**, *5*, 47.
[149] Olthuis, W.; Vankerkhof, J. C.; Bergveld, P.; Bos, M.; Vanderlinden, W. E., Preparation of Iridium Oxide and Its Application in Sensor Actuator Systems, *Sens. Actuator B-Chem.* **1991**, *4*, 151.
[150] Ardizzone, S.; Carugati, A.; Trasatti, S., Properties of Thermally Prepared Iridium Dioxide Electrodes, *J. Electroanal. Chem.* **1981**, *126*, 287.
[151] Glab, S.; Hulanicki, A.; Edwall, G.; Ingman, F., Metal-Metal Oxide and Metal-Oxide Electrodes as Ph Sensors, *Critical Reviews in Analytical Chemistry* **1989**, *21*, 29.
[152] Rauh, D., Design and fabrication of electrochromic light modulators, *Sol. Energy Mater. Sol. Cells* **1995**, *39*, 145.
[153] Lefrou, C.; Gentilhomme, C.; Ast, M., Testing of electrochromic materials using symmetrical devices, *Journal of Applied Electrochemistry* **2006**, *36*, 1011.
[154] Terashima, C.; Rao, T. N.; Sarada, B. V.; Spataru, N.; Fujishima, A., Electrodeposition of hydrous iridium oxide on conductive diamond electrodes for catalytic sensor applications, *J. Electroanal. Chem.* **2003**, *544*, 65.
[155] Xian, Y. Z.; Sun, W. L.; Xue, J. A.; Luo, M.; Jin, L. T., Iridium oxide and palladium modified nitric oxide microsensor, *Anal. Chim. Acta* **1999**, *381*, 191.
[156] Yagi, M.; Tomita, E.; Kuwabara, T., Remarkably high activity of electrodeposited IrO2 film for electrocatalytic water oxidation, *J. Electroanal. Chem.* **2005**, *579*, 83.
[157] Lee, I. S.; Park, J. M.; Son, H. J.; Park, J. C.; Lee, G. H.; Lee, Y. H.; Ciu, F. Z. In *Asbm6: Advanced Biomaterials Vi*, 2005; Vol. 288-289, pp 307.
[158] Lee, I. S.; Whang, C. N.; Lee, Y. H.; Lee, G. H.; Park, B. J.; Park, J. C.; Seo, W. S.; Cui, F. Z., Formation of nano iridium oxide: material properties and neural cell culture, *Thin Solid Films* **2005**, *475*, 332.

[159] Silva, T. M.; Rito, J.; Ferreira, M. G. S.; Fonseca, I.; Watkins, K., Electrochemical response of iridium oxide for implanted neural stimulating electrodes, *Journal of Materials Science-Materials in Medicine* **1996**, *7*, 261.
[160] Meyer, R. D.; Cogan, S. E.; Nguyen, T. H.; Rauh, R. D., Electrodeposited iridium oxide for neural stimulation and recording electrodes, *IEEE Trans. Neural Syst. Rehabil. Eng.* **2001**, *9*, 2.
[161] Lee, I. S.; Whang, C. N.; Choi, K.; Choo, M. S.; Lee, Y. H., Characterization of iridium film as a stimulating neural electrode, *Biomaterials* **2002**, *23*, 2375.
[162] Cogan, S. F.; Guzelian, A. A.; Agnew, W. F.; Yuen, T. G. H.; McCreery, D. B., Over-pulsing degrades activated iridium oxide films used for intracortical neural stimulation, *J. Neurosci. Methods* **2004**, *137*, 141.
[163] Juodkazyte, J.; Sebeka, B.; Valsiunas, I.; Juodkazis, K., Iridium anodic oxidation to Ir(III) and Ir(IV) hydrous oxides, *Electroanalysis* **2005**, *17*, 947.
[164] Silva, T. M.; Simoes, A. M. P.; Ferreira, M. G. S.; Walls, M.; Belo, M. D., Electronic structure of iridium oxide films formed in neutral phosphate buffer solution, *J. Electroanal. Chem.* **1998**, *441*, 5.
[165] Baur, J. E.; Spaine, T. W., Electrochemical deposition of iridium(IV) oxide from alkaline solutions of iridium(III) oxide, *J. Electroanal. Chem.* **1998**, *443*, 208.
[166] Mousty, C.; Foti, G.; Comninellis, C.; Reid, V., Electrochemical behaviour of DSA type electrodes prepared by induction heating, *Electrochim. Acta* **1999**, *45*, 451.
[167] Pauporte, T.; Aberdam, D.; Hazemann, J. L.; Faure, R.; Durand, R., X-ray absorption in relation to valency of iridium in sputtered iridium oxide films, *J. Electroanal. Chem.* **1999**, *465*, 88.
[168] Wang, M.; Yao, S.; Madou, M., A long-term stable iridium oxide pH electrode, *Sens. Actuator B-Chem.* **2002**, *81*, 313.
[169] Nishio, K.; Watanabe, Y.; Tsuchiya, T., Preparation and properties of electrochromic iridium oxide thin film by sol-gel process, *Thin Solid Films* **1999**, *350*, 96.
[170] Olthuis, W.; Robben, M. A. M.; Bergveld, P.; Bos, M.; Vanderlinden, W. E., Ph Sensor Properties of Electrochemically Grown Iridium Oxide, *Sens. Actuator B-Chem.* **1990**, *2*, 247.
[171] Korotcov, A.; Huang, Y. S.; Tsai, D. S.; Tiong, K. K., Growth and characterization of well aligned densely packed IrO2 nanocrystals on sapphire via reactive sputtering, *Journal of Physics-Condensed Matter* **2006**, *18*, 1121.
[172] Korotcov, A.; Hsu, H. P.; Huang, Y. S.; Tsai, D. S., Raman scattering characterization of well-aligned IrO2 nanocrystals grown on sapphire substrates via reactive sputtering, *Journal of Raman Spectroscopy* **2006**, *37*, 1411.
[173] Bock, C.; Birss, V. I., Irreversible decrease of Ir oxide film redox kinetics, *J. Electrochem. Soc.* **1999**, *146*, 1766.
[174] Slavcheva, E.; Vitushinsky, R.; Mokwa, W.; Schnakenberg, U., Sputtered iridium oxide films as charge injection material for functional electrostimulation, *J. Electrochem. Soc.* **2004**, *151*, E226.
[175] Slavcheva, E.; Schnakenberg, U.; Mokwa, W., Deposition of sputtered iridium oxide - Influence of oxygen flow in the reactor on the film properties, *Appl. Surf. Sci.* **2006**, *253*, 1964.

[176] Osman, J. R.; Crayston, J. A.; Pratt, A.; Richens, D. T., Sol-gel processing of IrO2-TiO2 mixed metal oxides based on a hexachloroiridate precursor, *Journal of Sol-Gel Science and Technology* **2007**, *44*, 219.
[177] Nishio, K.; Tsuchiya, T., Electrochromic thin films prepared by sol-gel process, *Sol. Energy Mater. Sol. Cells* **2001**, *68*, 279.
[178] Jaworski, R. K.; Cox, J. A.; Strohmeier, B. R., Characterization of Oxide-Films Electrochemically Deposited from Solutions of Palladium-Chloride and Sodium Hexachloroiridate, *J. Electroanal. Chem.* **1992**, *325*, 111.
[179] Cox, J. A.; Gadd, S. E.; Das, B. K., Modification of Glassy-Carbon with a Stable Film Containing Iridium Oxide and Palladium, *J. Electroanal. Chem.* **1988**, *256*, 199.
[180] Yamanaka, K., Anodically Electrodeposited Iridium Oxide-Films (Aeirof) from Alkaline-Solutions for Electrochromic Display Devices, *Jpn. J. Appl. Phys. Part 1 - Regul. Pap. Short Notes Rev. Pap.* **1989**, *28*, 632.
[181] Yamanaka, K., The Electrochemical-Behavior of Anodically Electrodeposited Iridium Oxide-Films and the Reliability of Transmittance Variable Cells, *Jpn. J. Appl. Phys. Part 1 - Regul. Pap. Short Notes Rev. Pap.* **1991**, *30*, 1285.
[182] Yoshino, T.; Baba, N.; Arai, K., Electrochromic Irox Thin-Films Formed in Sulfatoiridate (Iii,Iv) Complex Solution by Periodic Reverse Current Electrolysis (Prirof), *Jpn. J. Appl. Phys. Part 1 - Regul. Pap. Short Notes Rev. Pap.* **1987**, *26*, 1547.
[183] Granqvist, G. G., Handbook of Inorganic Electrochromism Materials, **1995**.
[184] Lampert, C. M., Solar-Energy Materials Related Papers of the Proceedings of the Optical-Materials Technology for Energy Efficiency and Solar-Energy Conversion Vi Conference - San Diego, Ca, 18-19 August 1987 - Preface, *Solar Energy Materials* **1989**, *19*, R7.
[185] Patil, P. S., Solution thermolysed tungsten oxide-based electrochromic devices: thickness-dependent step potential analysis, *Journal of Solid State Electrochemistry* **2002**, *6*, 284.
[186] Cogan, S. F.; Plante, T. D.; McFadden, R. S.; Rauh, R. D., Solar Modulation in a-Wo3 a-Iro2 and C-Kxwo3+(X/2) a-Iro2 Complementary Electrochromic Windows, *Solar Energy Materials* **1987**, *16*, 371.
[187] Bohnke, O.; Bohnke, C.; Robert, G.; Carquille, B., Electrochromism in Wo3 Thin-Films .2. Liclo4-Dioxolane-Water Electrolytes, *Solid State Ionics* **1982**, *6*, 267.
[188] Bohnke, O.; Bohnke, C.; Robert, G.; Carquille, B., Electrochromism in Wo3 Thin-Films .1. Liclo4-Propylene Carbonate Water-Electrolytes, *Solid State Ionics* **1982**, *6*, 121.
[189] McIntyre, J. D. E.; Peck, W. F.; Schwartz, G. P., Electrochromism in Hydrous Nickel-Oxide Films, *Journal of Electronic Materials* **1979**, *8*, 707.
[190] Delichere, P.; Joiret, S.; Hugotlegoff, A.; Bange, K.; Hetz, B., Electrochromism in Nickel-Oxide Thin-Films Studied by Oma and Raman-Spectroscopy, *J. Electrochem. Soc.* **1988**, *135*, 1856.
[191] Ottermann, C. R.; Temmink, A.; Bange, K., Comparison of Tungsten and Nickel-Oxide Electrochromism in Single Films and in All-Solid-State Devices, *Thin Solid Films* **1990**, *193*, 409.

[192] Niklasson, G. A.; Granqvist, C. G., Electrochromics for smart windows: thin films of tungsten oxide and nickel oxide, and devices based on these, *J. Mater. Chem.* **2007**, *17*, 127.
[193] Kanoh, H.; Hirotsu, T.; Ooi, K., Electrochromic behavior of a lambda-MnO2 electrode accompanying Li+-insertion in an aqueous phase, *J. Electrochem. Soc.* **1996**, *143*, 905.
[194] Monk, P. M. S.; Ali, T.; Partridge, R. D., The Effect of Doping Electrochromic Molybdenum Oxide with Other Metal-Oxides - Correlation of Optical and Kinetic-Properties, *Solid State Ionics* **1995**, *80*, 75.
[195] Mujawar, S. H.; Inamdar, A. I.; Betty, C. A.; Ganesan, V.; Patil, P. S., Effect of post annealing treatment on electrochromic properties of spray deposited niobium oxide thin films, *Electrochim. Acta* **2007**, *52*, 4899.
[196] Mujawar, S. H.; Inamdar, A. I.; Patil, S. B.; Patil, P. S., Electrochromic properties of spray-deposited niobium oxide thin films, *Solid State Ionics* **2006**, *177*, 3333.
[197] Shay, J. L.; Beni, G.; Schiavone, L. M., Electrochromism of Anodic Iridium Oxide-Films on Transparent Substrates, *Applied Physics Letters* **1978**, *33*, 942.
[198] Beni, G.; Shay, J. L., Electrochromism in Anodic Iridium Oxide-Films, *Applied Physics Letters* **1978**, *33*, 208.
[199] Beni, G.; Shay, J. L., Electrochromism of Heat-Treated Anodic Iridium Oxide-Films in Acidic, Neutral, and Alkaline-Solutions, *Applied Physics Letters* **1978**, *33*, 567.
[200] Patil, P. S.; Kawar, R. K.; Sadale, S. B., Electrochromism in spray deposited iridium oxide thin films, *Electrochim. Acta* **2005**, *50*, 2527.
[201] Rauh, R. D.; Cogan, S. F., Design-Model for Electrochromic Windows and Application to the Wo3/Iro2 System, *J. Electrochem. Soc.* **1993**, *140*, 378.
[202] Patil, P. S.; Mujawar, S. H.; Sadale, S. B.; Deshmukh, H. P.; Inamdar, A. I., Effect of film thickness on electrochromic activity of spray deposited iridium oxide thin films, *Materials Chemistry and Physics* **2006**, *99*, 309.
[203] Bartlett, P. N., Private Communication, **2007**.
[204] Liao, P. C.; Huang, Y. S.; Tiong, K. K., Characterization of RuO2 and IrO2 films deposited on Si substrate, *Journal of Alloys and Compounds* **2001**, *317*, 98.
[205] Liao, P. C.; Chen, C. S.; Ho, W. S.; Huang, Y. S.; Tiong, K. K., Characterization of IrO2 thin films by Raman spectroscopy, *Thin Solid Films* **1997**, *301*, 7.
[206] Vlasov, Y. A.; Astratov, V. N.; Baryshev, A. V.; Kaplyanskii, A. A.; Karimov, O. Z.; Limonov, M. F., Manifestation of intrinsic defects in optical properties of self-organized opal photonic crystals, *Phys. Rev. E* **2000**, *61*, 5784–5793.
[207] Bartlett, P. N.; Baumberg, J. J.; Coyle, S.; Abdelsalam, M. E., Optical properties of nanostructured metal films, *Faraday Discussions* **2004**, *125*, 117.
[208] Nagayama, K., Two-dimensional self-assembly of colloids in thin liquid films, *Colloid Surf. A-Physicochem. Eng. Asp.* **1996**, *109*, 363.
[209] Mahajan, S., *Private Communication* **2007**.
[210] Denuault, G., *Private Communication* **2007**.
[211] Patil, P. S.; Kawar, R. K.; Sadale, S. B., Effect of substrate temperature on electrochromic properties of spray-deposited Ir-oxide thin films, *Appl. Surf. Sci.* **2005**, *249*, 367.

[212] Sato, Y.; Ono, K.; Kobayashi, T.; Wakabayashi, H.; Yamanaka, H., Electrochromism in Iridium Oxide-Films Prepared by Thermal-Oxidation of Iridium-Carbon Composite Films, *J. Electrochem. Soc.* **1987**, *134*, 570.
[213] Abdelsalam, M. E.; Mahajan, S.; Bartlett, P. N.; Baumberg, J. J.; Russell, A. E., SERS at structured palladium and platinum surfaces, *J. Am. Chem. Soc.* **2007**, *129*, 7399.
[214] Rhodes, C. F., S, Surface plasmon resonance in conducting metal oxides, *J. Appl. Phys.* **2006**, *100*.
[215] Denuault, G., Electrodeposition of highly ordered macroporous iridium oxide through self-assembled colloidal templates, *J. Mater Chem. 2009.*